UNIVERSITY OF OKLAHOMA

GRADUATE COLLEGE

EXAMINING METEOROLOGICAL BENEFITS OF RAPID-SCAN,

DUAL-POLARIZATION, ALL-DIGITAL PHASED ARRAY RADAR

OBSERVATIONS FOR DETECTING TORNADO FORMATION AND

INTENSIFICATION

A THESIS

SUBMITTED TO THE GRADUATE FACULTY

in partial fulfillment of the requirements for the

Degree of

MASTER OF SCIENCE IN METEOROLOGY

By

BRANDON KEITH COHEN
Norman, Oklahoma
2022

EXAMINING METEOROLOGICAL BENEFITS OF RAPID-SCAN,
DUAL-POLARIZATION, ALL-DIGITAL PHASED ARRAY RADAR
OBSERVATIONS FOR DETECTING TORNADO FORMATION AND
INTENSIFICATION

A THESIS APPROVED FOR THE
SCHOOL OF METEOROLOGY

BY THE COMMITTEE CONSISTING OF

Dr. David J. Bodine, Chair

Dr. Mark B. Yeary, Co-Chair

Dr. Jeffrey C. Snyder

Dr. Robert D. Palmer

Dr. Howard B. Bluestein

Dr. Kelvin K. Droegemeier

Dedication

To my Pop, in loving memory. While you have not been around to be a part of this adventure, you passed down your love for travel (as well as train and plane spotting) and for sitting on the porch to watch storms. I found your tenacity, unparalleled passion, and love for everything you did to be an infectious example of the best way to live life with no regrets and motivation to continue my studies. You encouraged my passions every step of the way, and I have no doubt you would be doing the same now.

This work is also dedicated in memory of the three OU School of Meteorology undergraduate students we lost too soon on 29 April 2022: Gavin Short, Nicholas Nair, and Drake Brooks. Each of you had bright futures full of accomplishments in our field, and I thank you for the opportunity to be a part of your journey to fulfill your dreams of becoming meteorologists. You may be gone, but you will never be forgotten. Never stop chasing your dreams, OU3.

Acknowledgments

Over the past two years as a master's student, I have been blessed to work with so many amazing people who have helped to not only improve this study but also improve me as both a scientist and a person. I must start by giving a huge thank you to my advisors: Dr. David Bodine, Dr. Mark Yeary, and Dr. Jeffrey Snyder. The three of you made transitioning to graduate school, starting independent living in Oklahoma, and working in radar research incredibly smooth despite the (ongoing) global COVID-19 pandemic. All of your feedback and comments on my research, our debugging sessions, our weekly meetings and off-topic discussions, and field work experiences have made working with the three of you fun and rewarding. I cannot imagine working with advisors that are a better trio, and I thank you for taking a chance on me and allowing me to pursue my dream of studying at OU. I look forward to continuing to work with you all on my PhD. I also thank Dr. Robert Palmer, who taught me more about weather radar than I thought I would ever know, especially from an engineering perspective. Your class challenged me to think outside the box and strengthened my academic and research skill sets. I also must thank you for taking a chance on me to join the ARRC. Combined with my advisors, you all have provided me with more confidence in my capabilities and value as a scientist in ways I could never have imagined. And, of course, a thank you to Dr. Howard Bluestein and Dr. Kelvin Droegemeier for taking the time to serve on my committee.

I also would like to thank Dr. Jana Houser and Zach Wienhoff for their helpful insight to the data sets used in this study. Your willingness to engage in discussions and share your wealth of knowledge helped to not only strengthen these results but also made me a better scientist. A larger thank you extends to Dr. Howard Bluestein and his research group members for the collection of the data used in this study.

I also want to acknowledge the unconditional love and support of my mom and dad. They have always been the perfect examples of what a little elbow (or mind) grease

and commitment can bring to those who aspire to achieve. While I may not have said it enough growing up, I cannot thank you enough for what you have done for me and allowed me to branch out and do. I would not be working with my passion everyday if you had not nurtured this curiosity for our atmosphere. I also would like to thank my sister, Kaleigh, for being there whenever I needed her. From sharing the joy of our accomplishments to venting about frustrations, I would not have been able to maintain my well-being without your listening ear and thoughtful advice along the way. I could not be prouder to watch you begin your own academic journey in psychology, and look forward to seeing and celebrating your own accomplishments for many years ahead.

Another thank you goes to my friends both in Norman and afar (with a special acknowledgement to my Friday night dinner and games group) and fellow group members (Laura, Rachael, Morgan, and Sam) as all of you have made coming to OU and to work every day easier and an absolute joy. It is easy to want to come to work every day knowing that one of you will bring a smile or laugh to my face, an animal photo to my desk, and the knowledge to make my own work even better. The excellence each of you has shown in your work has been a constant source of motivation to improve this study along the way. I would certainly not be where I am today without the support you all have given me over the last two years.

There are many others who have helped me on my journey, and while I cannot possibly name each of you, I am forever thankful for your support, friendship, and inspiration to continue pursuing my dreams.

Table of Contents

List Of Tables

List Of Figures

Abstract

Phased array radar (PAR) is widely considered the future for a replacement to the current operational radar network, NEXRAD. In particular, an all-digital operational PAR network offers a range of benefits including adaptive scanning techniques, higher temporal resolution especially via radar imaging modes, and denser vertical sampling to allow for more complete observations of severe hazard structure and evolution. This study focuses on the application of future operational phased array radar (PAR) systems to observe tornadoes and their formation. To best understand the benefits of a future all-digital operational PAR, we generate synthetic PAR observations from archived mobile rapid-scan observations collected by the Rapid X-band Polarimetric radar (RaXPol) to emulate typical operational radar ranges, PAR enabled scanning strategy effects, and NEXRAD and future possible PAR volumetric update times.

In this study, the synthetic PAR tool is applied to two datasets from RaXPol: the 24 May 2011 El Reno, Oklahoma, tornado and the 24 May 2016 Dodge City, Kansas, tornadoes. Range and azimuth averaging is applied over different windows to emulate different standoff ranges more comparable to operational, fixed-site radars. Using dealiased velocity data, we analyze the intensity of synthetic PAR tornado vortex signatures (TVSs) through a measure of the intensity of rotation (ΔV) plotted as a function of time and height for each different standoff range. Despite increasingly coarse resolution, we find similar qualitative trends in the vertical evolution of TVS intensity even though the magnitude of ΔV decreases. TVS intensification is found to occur in an ascending or simultaneous manner, even for data that has undergone spatial resampling to much longer standoff ranges (e.g., 80 km). Thus, it appears that detection of rapid TVS intensification occurring in an upward or simultaneous manner, as seen previously with mobile radars, can be used to detect tornadogenesis with future operational PARs. Additional work has focused on comparison of expected PAR revisit times in comparison to NEXRAD volume scan times. Update times of

60 s or faster are found enhance the data available to forecasters by better capturing critical evolution steps currently missed at NEXRAD update times (i.e., typical volume updates every 5—6 min). However, at longer standoff ranges, a slight delay in observing the TVS intensification is found across tested temporal resolutions. We also observed some instances at longer standoff ranges where tornado-scale versus mesocyclone-scale TVS intensification may be occurring in different directions, particularly at 40 s and 5 min updates. Finally, we have analyzed the implementation of focusing, which shows promising results. Focusing could be used by an operational radar to enable updates faster than 60 s by targeted observations of specific storms or a region within a larger storm complex. Ultimately, through understanding the meteorological benefits from the synthetic PAR data, we should be able to contribute to improved planning for future all-digital operational PARs and warning decisions for tornadic storms.

Chapter 1

Introduction

Severe weather hazards, such as tornadoes, pose a significant risk to life and property. They also remain a meteorological phenomena still not fully understood and challenging to predict; thus, they are important for both operational and research meteorology. As storm evolution occurs on an advective time scale of $\sim$100 s (Bluestein and Wakimoto 2003) and (assuming a 100 m core radius and $\sim$60 m s^{-1} wind speeds) tornadoes have a shorter advective time scale of $\sim$10 s (Bluestein et al. 2003, 2010; Tanamachi et al. 2007; Wurman and Gill 2000), it is evident that severe storms and their associated hazards are rapidly evolving phenomena. Tornadoes also occur infrequently and exhibit a wide range of variability from the duration of their life cycles (60 s or less to over an hour) to their intensity (29 m s^{-1} to $>$ 89 m s^{-1}). This rapid evolution and variability increases the difficulty of detecting critical moments to identify and further understand the structure and evolution of tornadoes. Other phenomena such as hail and severe wind events are also rapidly evolving, with processes such as hail melt and drop shedding occurring on the order of minutes to seconds (Ryzhkov et al. 2013).

One widely used method by operational meteorologists for observing severe weather hazards and making warning decisions is Doppler weather radar. In the United States, 154 parabolic dish Weather Surveillance Radar - 1988 Dopplers (WSR-88D; Crum and Alberty 1993b), or the Next Generation Weather Radar (NEXRAD) network, are currently used by the National Weather Service (NWS) alongside the Federal Aviation

Administration and the Department of Defense to provide weather surveillance. While this coverage would ideally be continuous and data instantaneously retrieved, a radar requires a measurable amount of time to collect high-quality observations (Doviak and Zrnić 2006). To collect data best suited for any ongoing weather phenomenon or clear air, the WSR-88D network utilizes Volume Coverage Patterns (VCPs; Office of the Federal Coordinator for Meteorological Services and Supporting Research 2007) operating as pre-defined scanning strategies providing a balance between important trade-offs such as data quality, spatial coverage, sensitivity, and the frequency of complete volumetric updates.

The average WSR-88D volumetric update time (i.e., time to complete a VCP) is 5–7 min, but can reduce to ∼4–4.5 min when the radar is operating on VCP 12 or 212. The OFCM's Federal Meteorological Handbook has defined required elevation angles for each VCP use, with Figure 1.1 showing the required elevation angles which comprise VCPs 12/212. The longer duration to complete a volumetric scan is linked to the mechanical steering of the antennas in the WSR-88D network. While the Radar Operations Center has and continues to make improvements to the VCPs available to NWS meteorologists (e.g., Radar Operations Center 2015), further reducing the volumetric update time would reqiure one or more of the following: (a) the elimination of elevation angles from the pattern, (b) adaptive scanning[1], a capability not currently offered by the radar network, or (c) faster rotation speeds, which would increase stress on the radar's motors. The closest capabilities of WSR-88Ds to adaptive scanning modes are AVSET (Automated Volume Scan Evaluation and Termination), SAILS/MESO-SAILS (Supplemental Adaptive Intra-Volume Low-Level Scan/Multiple Elevation Scan

---

[1]Adaptive scanning techniques on fixed-site radars have been tested before. Testbed networks of X-band radars, known as Collaborative Adaptive Sensing of the Atmosphere (CASA; McLaughlin et al. 2009) radars, provided distributed collaborative adaptive sensing (DCAS; McLaughlin et al. 2009) to optimize scanning for a variety of weather phenomena as well as targeted sector-scanning. Results from studies such as Brotzge et al. (2010) have shown the utility in the CASA radars providing more focused volumetric scans as well as features not otherwise identified in WSR-88D data.

Option for SAILS) or MRLE (Mid-volume Rescan of Low-level Elevations), which have restricted usage dependent upon precipitation coverage and/or VCP. However, despite providing additional low-level data, utilizing these scanning modes can lead to an undesirable increase in the volumetric update time. As a result of longer volumetric update times (among other limitations discussed below), the observations collected by the WSR-88D network may (and, at times, do) miss key moments in capturing the structure and rapid evolution of severe hazards.

The operating requirements and locations of the WSR-88D radars make it difficult to capture and understand these infrequent, complex, and dynamic phenomena. Some limitations of this fixed-side, widely spaced radar network are or relate to: missed near-ground processes (e.g., from Earth's curvature effect at increasing distance from the radar[2]), obstructions, and decreased likelihood of collecting observations of convection and tornadoes. Thus, to address these, mobile radar systems have been built and operated since the late 1980s with the Los Alamos National Laboratory's (LANL) portable, continuous wave (CW), 3-m Doppler radar, later modified in 1988 to operate in the FM (frequency modulated)-CW mode (Bluestein and Unruh 1989). Analyses of CW Doppler wind spectra collected at relatively close range with simultaneous photographic and video documentation by the LANL radar in 1990 and 1991 were first presented in Bluestein et al. (1993). Throughout the 1990s, additional mobile radars were deployed such as the U-Mass Mobile W-band radar (Mead et al. 1994; Bluestein et al. 1995) and the Doppler on Wheels (DOW; Wurman et al. 1997). With further development of technology, new rapid-scan mobile radar systems have been built since such as the Meteorological Weather Radar 2005 X-band Phased Array (MWR-05XP; Bluestein et al. 2010), the Atmospheric Imaging Radar (AIR; Isom et al. 2013;

---

[2]The CASA radars also sought to address this "sensing gap" through a dense network of closely spaced X-band radars (McLaughlin et al. 2009).
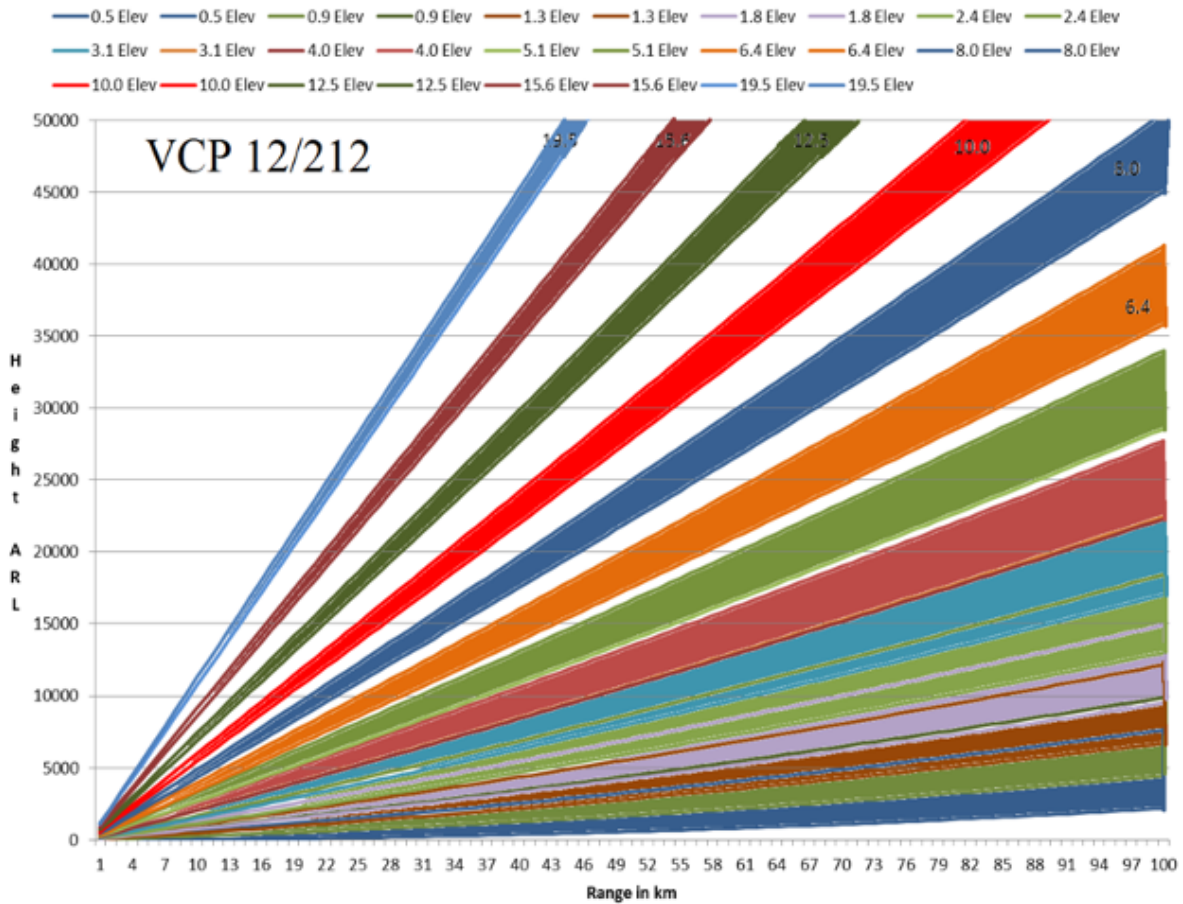
Figure 1.1: A visual of the elevation angles scanned by VCPs 12/212 as found in the VCP Improvement Initiatives from Radar Operations Center (2015).

Kurdzo et al. 2017), the Rapid, X-band Polarimetric (RaXPol; Pazmany et al. 2013) radar, and the SKYLER (Kollias et al. 2022) phased array radar (PAR). There are also two new systems scheduled to be completed and operational this year: the all-digital, polarimetric Horus PAR (Palmer et al. 2019) and the Polarimetric Atmospheric Imaging Radar (PAIR; Salazar et al. 2019).

While each system has its own unique capabilities, in general, these mobile systems offer a few key benefits that aid in the study of convective storms and severe hazards. These include higher resolution (spatial and temporal) and flexible positioning. A few

systems, such as RaXPol and the DOW8, have rapid-scan[3] capabilities enabling fast volumetric updates of ∼15-20 s while still collecting high-quality data. Even with a rapid-scan system like RaXPol, it remains difficult to capture all of a tornado's evolution. As Bluestein et al. (2003) showed, even with ∼10–15 s sector scan updates from a mobile, W-band radar, there are still missed evolutionary components. Nonetheless, these radars have been crucial to the continued development and revision of existing conceptual models, especially related to tornado formation (e.g., French et al. 2013, 2014).

Some of these conceptual models consider a visual cue provided by Doppler radar that aids in the detection of tornadoes: the tornadic vortex signature (TVS; Brown et al. 1978). A TVS is a region of persistent, localized, strong shear where azimuthally adjacent (or gate-to-gate) peak radial velocity values of opposite signs are observed. Notably, a weak tornado that is rapidly moving towards or away from the radar may not have radial velocity of opposite signs. While not every tornado has a TVS and the observation of a TVS is not necessarily a guarantee of tornado formation or an ongoing tornado, it does provide greater confidence for NWS forecasters when making warning decisions (Kuster et al. 2015). Previous observations used to explain tornadogenesis using observations from the WSR-88D network and mobile radars have found differing TVS intensification methods. Studies using data from WSR-88D radars have generally supported a TVS forming aloft and descending to the surface (e.g., Trapp and Davies-Jones 1997; Trapp et al. 1999; Vasiloff 1993), also referred to as the dynamic pipe effect (DPE; Leslie 1971). It should be noted that Trapp and Davies-Jones (1997) did also introduce a bimodal tornadogenesis model, and Trapp et al. (1999) identified

---

[3]The definition of "rapid-scan" varies from platform to platform. In this study, with a focus on RaXPol data, this is a scanning rate defined by Pazmany et al. (2013) as "hundreds of degrees per second rather than tens of degrees per second" with the latter being a more appropriate definition for the DOW8. For operational purposes, "rapid-scan" would be defined by a volume scan (or volumetric sector) collected in 1 min or less.

some non-descending TVSs as well (see Section 2.1.2). More recent mobile radar based studies have observed a TVS forming at the low-levels (i.e., near-ground) and ascending or forming in a nearly simultaneous manner (e.g., Alexander and Wurman 2005; Alexander 2010; Bluestein et al. 2019; French et al. 2013, 2014). Using analysis from a mobile radar, French et al. (2013) suggested that this descending TVS conceptual model from operational radars was an artifact of insufficient temporal resolution to sample the common presence of transient mid-level TVSs (e.g., Burgess et al. 1975; Brown et al. 1978; Brown and Wood 2012). The observations in these mobile radar studies only represent an extremely small fraction of tornadoes and are heavily biased towards mesocyclone-produced tornadoes in supercells in the central United States preventing generalization of the findings to all tornadoes. The temporal and spatial capabilities of mobile systems to detect more tornado-scale processes have shown support for non-descending TVS intensification within the limited focus of these data sets. This difference in observations, however, should not discount the value and successes of the WSR-88D network and its value to current NWS operations and warning processes.

As the current operational radar network continues to age, a replacement system will be needed by 2040 when the current reliable service life of the WSR-88D network is set to come to an end (Cook et al. 2014). PARs are under scientific evaluation as a potential future replacement for the radars within the WSR-88D network (Joint Action Group for Phased Array Radar Project 2006; National Research Council 2002, 2008; National Severe Storms Laboratory 2020; Weber et al. 2021). One possible system design would consist of a rotating, all-digital, dual-polarization PAR, which has shown the capability to meet NOAA's radar functional requirements discussed in National Weather Service (2015) (e.g., 1-min volumetric updates, 1° beamwidth). A future all-digital PAR could provide several enhancements to the detection and study of severe hazards including adaptive scanning techniques, improved temporal resolution, and

denser vertical sampling through imaging. While the development of this technology has faced challenges (e.g., dual-polarization; Zhang et al. 2008), numerous studies over the last 15 years have demonstrated the possibilities afforded by PAR technologies, which have included analyses of: operational benefits of rapid-scan observations (e.g., Heinselman et al. 2008; Kuster et al. 2015, 2016), PAR signal processing techniques (e.g., Kurdzo et al. 2014; Yu et al. 2007), adaptive scanning capabilities (e.g., Heinselman and Torres 2011; Torres and Schvartzman 2020), and array and dual-polarization calibration (e.g., Fulton et al. 2016; Ivic et al. 2019) alongside prototype and proof-of-concept systems such as the ATD (Advanced Technology Demonstrator; Hondl and Weber 2019).
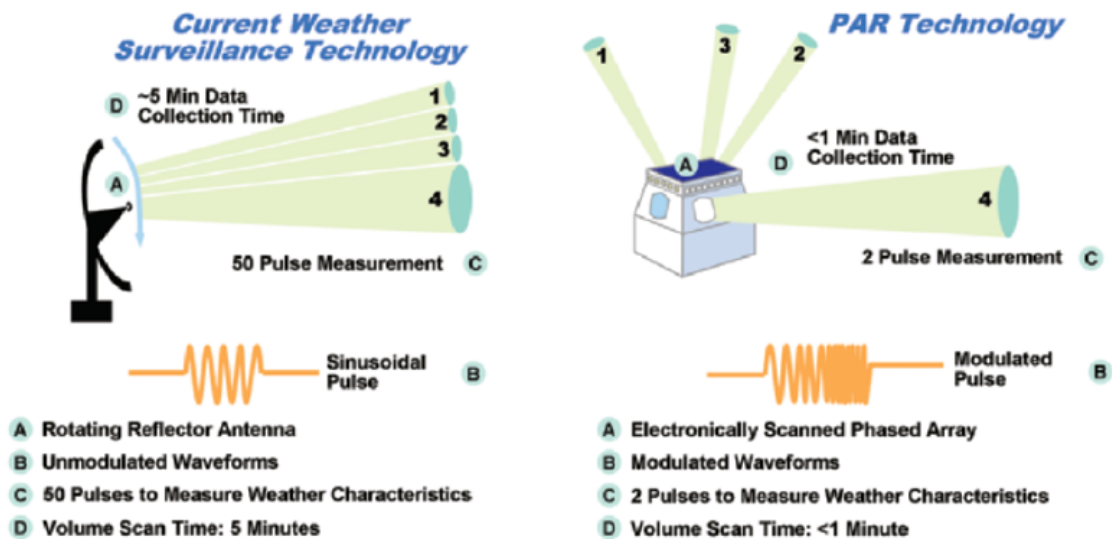
Figure 1.2: Reprinted from Zrnić et al. (2007), showing basic differences between the (left) conventional radar with a mechanically rotating antenna and (right) agile-beam PAR.

A PAR, at its simplest level, is an array consisting of multiple individual radiating antenna elements with coherently combined signals capable of transmitting and receiving a pulse of electromagnetic energy. The design and placement of elements in this

array can be modified and adapted to meet different design specifications such as a desired beamwidth or a stationary versus rotating system. Thus, given this technology and the flexibility in creating a blueprint for any PAR, it is easy to see how a system such as this would be significantly different than the current operational radar design. An overview of some basic differences between current mechanically rotated parabolic dish radars in comparison to an agile-beam PAR are shown in Figure 1.2. Notably, one of the most significant differences between these two systems is that PAR technology is able to form and steer an agile, electronic radar beam instantaneously while also remaining supportive of mechanical steering in azimuth due to its flexible and scalable architecture. In contrast, current WSR-88D radars consist of a single parabolic dish reflector in order to form the radar beam and must be mechanically steered in azimuth and elevation to complete a full planned position indicator (PPI).

The goal of this study is to further understand the potential benefits a future operational PAR network can offer to forecasters with respect to detecting tornadogenesis and intensification. Experiments such as PARISE (Phased Array Radar Innovative Sensing Experiment; Bowden et al. 2014, 2015; Heinselman et al. 2012, 2015; Tanamachi and Heinselman 2016; Wilson et al. 2017a) and studies such as Kuster et al. (2015) and Bowden and Heinselman (2016) have focused on the impacts to NWS forecasters and their warning decision process as well as data quality and resolution of observations across varied convective modes and severe hazards. Work still remains to understand long-range or PAR enabled scanning strategy effects on data from these systems. This study seeks to provide insight on these areas while also understanding any temporal impacts beyond forecaster performance and workload. Therefore, this study is guided by a broad research question: Can rapid-scan, dual-polarization observations from an all-digital PAR transform our capabilities to forecast and warn for tornadoes? To answer this question, our analysis focuses on the following three areas:

(1) spatial resolution impacts, (2) temporal resolution impacts, and (3) PAR-centric topics (i.e., scanning strategies). Some of the questions with each of these areas are:

- **Spatial Resolution Impacts**:

    - How does varying spatial resolution impact observed tornadogenesis processes? Are important ΔV changes still observed as spatial resolution degrades?

    - Can significant benefits still be realized when observing mesocyclone-scale processes?

- **Temporal Resolution Impacts**:

    - What temporal resolution is optimal for a future PAR to observe tornado formation?

    - Do faster update times provided by a PAR impact how tornadogenesis is observed?

- **PAR-centric Topics**:

    - How do observations of the TVS change when using PAR enabled scanning strategies in comparison to WSR-88D capabilities (such as the pencil beam)?

    - What all-digital PAR scanning modes can enable the optimal temporal resolution for a future PAR?

The remainder of this thesis covers material as follows. Chapter 2 gives a background of literature on the TVS and rapid-scan PAR data and forecaster response. Chapter 3 provides information about the data and methods used for this project.

Chapters 4 and 5 provide the results and discussion of this project through the analysis of two individual cases. Chapter 6 gives the conclusions and future work, including a discussion of considerations for operational PARs, and upcoming collaborative projects.

Chapter 2

Background

This chapter provides necessary background information to support the work in this thesis. An overview of previous literature is provided related to TVSs in Section 2.1 and prior work with PAR data and NWS forecasters in Section 2.2 to consider the prospects of future operational PARs.

2.1 The Tornado Vortex Signature

2.1.1 History to Discovery

Throughout the developmental history of Doppler weather radar, a central focus was placed on the detection of tornadoes or the parent circulation associated with the tornado. A 3-cm (X-band), continuous wave Doppler radar collected the first measurement of tornadic winds on 10 June 1958 as a tornado struck El Dorado, Kansas (Smith and Holmes 1961). Their work provided recommendations for improvements to future Doppler radar systems, and by the end of 1964, that same radar was modified into a pulsed Doppler radar (Lhermitte and Kessler 1964). Owing to the attenuation of 3-cm wavelength radars, the National Severe Storms Laboratory (NSSL) determined they were unfit for use as a national surveillance network. This lead to the development of a 10-cm (S-band) wavelength radar.

With the NSSL's 10-cm wavelength experimental Doppler radar, a unique Doppler velocity signature was detected in the mean Doppler velocity data on 24 May 1973 as a tornado struck Union City, Oklahoma. Brown et al. (1978) coined this signature the tornado vortex signature (TVS) and noted its utility in detecting a tornado as "localized extreme azimuthal shear in the mean Doppler velocity measurements" across 10 identified TVSs in their 1973-1976 data set. At the time of their study, objective identification criterion had not been adopted for widespread operational use. Instead, Brown et al. (1978) provided the following tentative guidelines on identifying the signature:

1. An azimuthal shear of at least 20 m s^{-1} over an azimuthal distance of approximately one beamwidth (typically greater than 1x10^{-2} s^{-1}).

2. Signature with extreme Doppler velocity values of opposite sign, after TVS translation has been removed.

3. Anomalous shear region not more than 1 km in range extent (otherwise it would indicate a shear line rather than a small-scale vortex).

4. Shear region at least several kilometers in vertical extent.

5. Persistent anomalous shear region at the same general heights for about 10 min or more.

This signature was found to be not detectable when the radar's gate width was greater than or equal to the size for the vortex being observed. As a result, due to limitations in sampling and the variance of size with tornadoes, not all tornadoes reported will be associated with a TVS (and not every TVS indicates an ongoing tornado). An additional challenge arises from Earth's curvature effects that can lead to beam heights that are too high to sample tornadoes (e.g., strongest tornadic shear near the ground with the radar beam observing above that shear region would result

in the radar observations missing that TVS near the ground). Several studies went on to confirm the existence of the TVS including Wilson et al. (1980), Dunn (1990), and Burgess et al. (1993).

2.1.2 Tracking Tornadogenesis via TVS Intensification

Observations (detailed in Brown et al. 1978) of the TVS from Union City provided the first information about tornadoes above cloud base. The signature was first identified at the mid-levels of the storm, and it worked its way downward to the ground over at least 25 min (Fig. 2.1). During this 25 min, the TVS increased in magnitude across all heights as it slowly descended toward the surface and continued to increase in magnitude until the tornado reached its maximum observed size after tornadogenesis. The eventual weakening and decay of the tornado were also observed in the TVS. These findings were found to an observational fit for descending tornadogenesis via the dynamic pipe effect (DPE; Leslie 1971). As the installation of the national WSR-88D network was completed by the mid-1990s, the TVS has been used in operations by the NWS for the identification of tornadoes, from genesis to decay, in Doppler weather radar data (Warning Decision Training Division 2022).

Researchers were skeptical and unsure of the exact role, if any, the TVS held in any recognized tornadogenesis model. Rotunno (1986) notably commented on this confusion stating, "...the appearance of a TVS aloft may not be relevant" and Rotunno (1993) further commented that "I still do not know where the tornado vortex signature fits into the picture."

Results from observational analysis found by Vasiloff (1993) and confirmed in numerical model simulations by Trapp and Fiedler (1995), however, both showed TVS formation could also occur in a simultaneous, uniform manner across a large depth

13
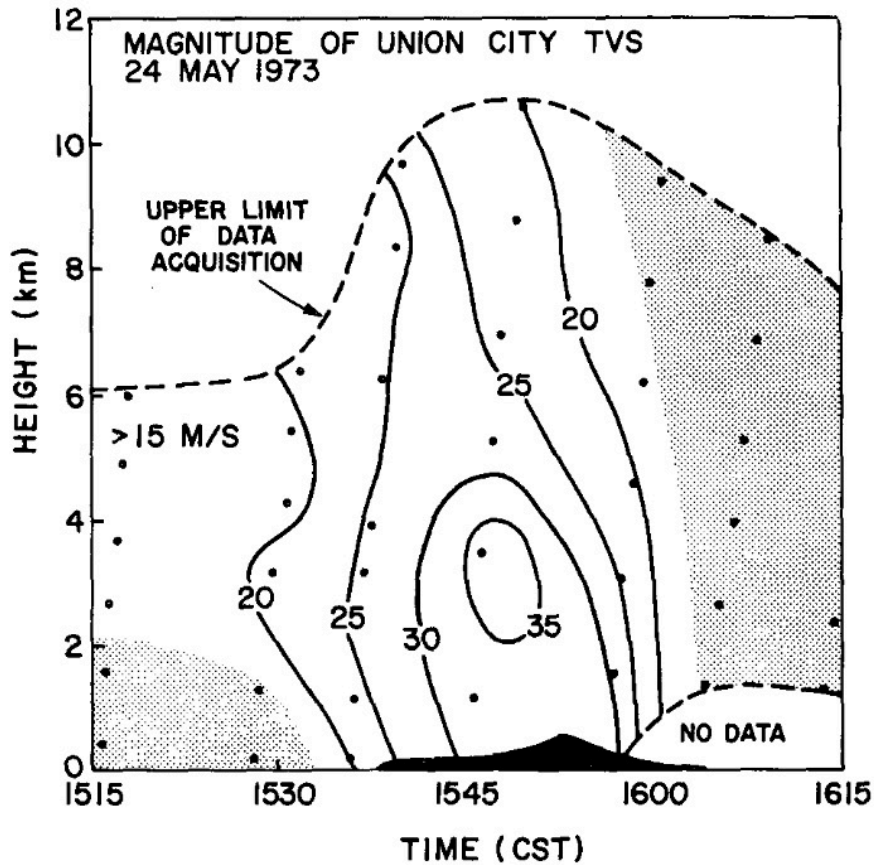
Figure 2.1: Time-height profile of the magnitude of the largest Doppler velocity value within each TVS (adjusted for TVS motion). Dots indicate data points and dashed lines represent the limits of data collection. Velocity shears below the TVS detectibility level are lightly shaded. The black region at the bottom center is the diameter (using ordinate scale) of the Union City tornado funnel near cloud base. Reprinted from Brown et al. (1978).

of the atmosphere or via ascent with time. These possibilities directly contrasted the results dependent on using the DPE to explain descending TVS intensification for tornadogenesis. Trapp and Mitchell (1995) analyzed 16 TVSs observed by WSR-88Ds and found a 50% split between the TVSs that descended versus those that ascended or formed simultaneously.

Prior to Trapp and Davies-Jones (1997), a lack of focus had been placed on explaining the physical processes that might explain a descending TVS. Their study used
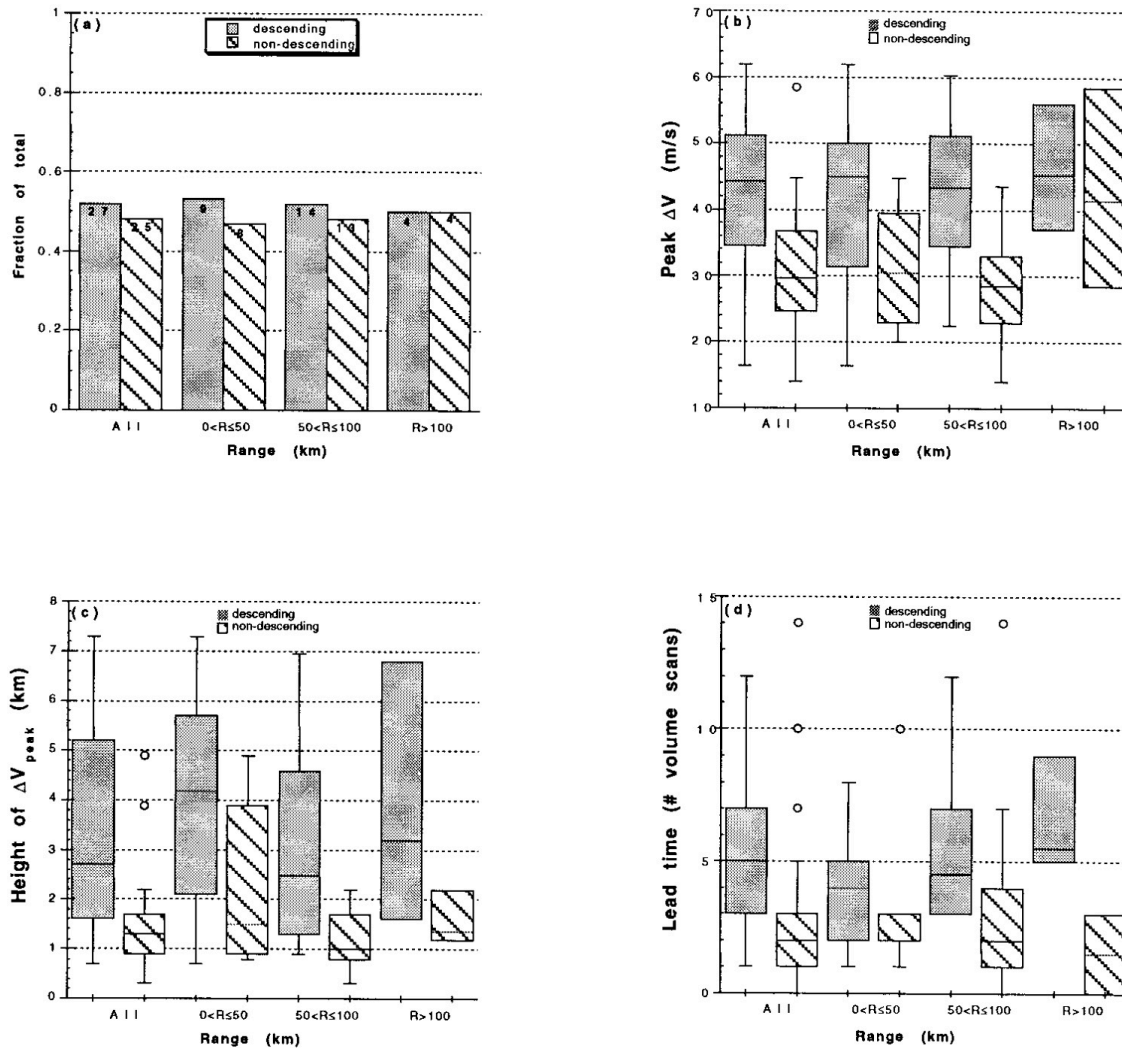
Figure 2.2: (a) Number of descending and nondescending TVSs, given as a fraction of the total occurring in a given range bin. Box plots of descending and nondescending TVS attributes, as a function of radar range; (b) peak, pretornadic gate-to-gate diffrential velocity (m s^{-1}); (c) height of the peak, pretornadic gate-to-gate differential velocity (km); and (d) lead time (in number of radar volume scans). Open circles indicate outliers, which are > the upper quartile + 1.5 X interquartile range or < the lower quartile - 1.5 X interquartile range. Reprinted from Trapp et al. (1999).

numerical and analytical models to introduce a bimodal tornadogenesis model. Mode I was linked to a descending TVS while mode II was linked to TVS formation that ascended or occurred nearly simultaneously across a column depth. Further work by Trapp et al. (1999) aimed to understand the relative frequency of each mode. Using 52 tornadoes observed by WSR-88D radars, mode I was found to have occurred for 52% of TVSs while the remaining 48% of TVSs were associated with mode II (Fig. 2.2).

In contrast to these limited observational studies, however, ascending or nearly simultaneous TVS intensification has been documented from WSR-88Ds (e.g., Burgess et al. 2002), Terminal Doppler Weather Radars (TDWRs) (e.g., Dunn and Vasiloff 2001), and mobile Doppler radars. It was with the advent of these ground-based, mobile radar platforms that more detailed and targeted analysis of TVSs was possible, particularly the detection of tornadogenesis on a much shorter time scale than with descending tornadogenesis via the DPE.

2.1.3   Recent Research and Developments

This more recent combination of dynamic scale analysis (Bluestein et al. 2003) and an increased number of data sets with both visual observations and increased spatio-temporal resolution data from mobile radar systems (like those discussed in Chapter 1), particularly rapid-scan radars, has been the focus of several studies on tornadogenesis (e.g., Alexander and Wurman 2008; Alexander 2010; Bluestein et al. 2010, 2019; French et al. 2013, 2014; Griffin et al. 2019; Houser et al. 2015, 2022; Kurdzo et al. 2015, 2017; Snyder and Bluestein 2014; Wienhoff et al. 2020). These studies, among numerous others, have generally failed to find support for TVS descent via the DPE.

Instead, they have continually found evidence of ascending or almost simultaneous growth of the TVS across a column depth that occurs on the order of seconds to 1 min.
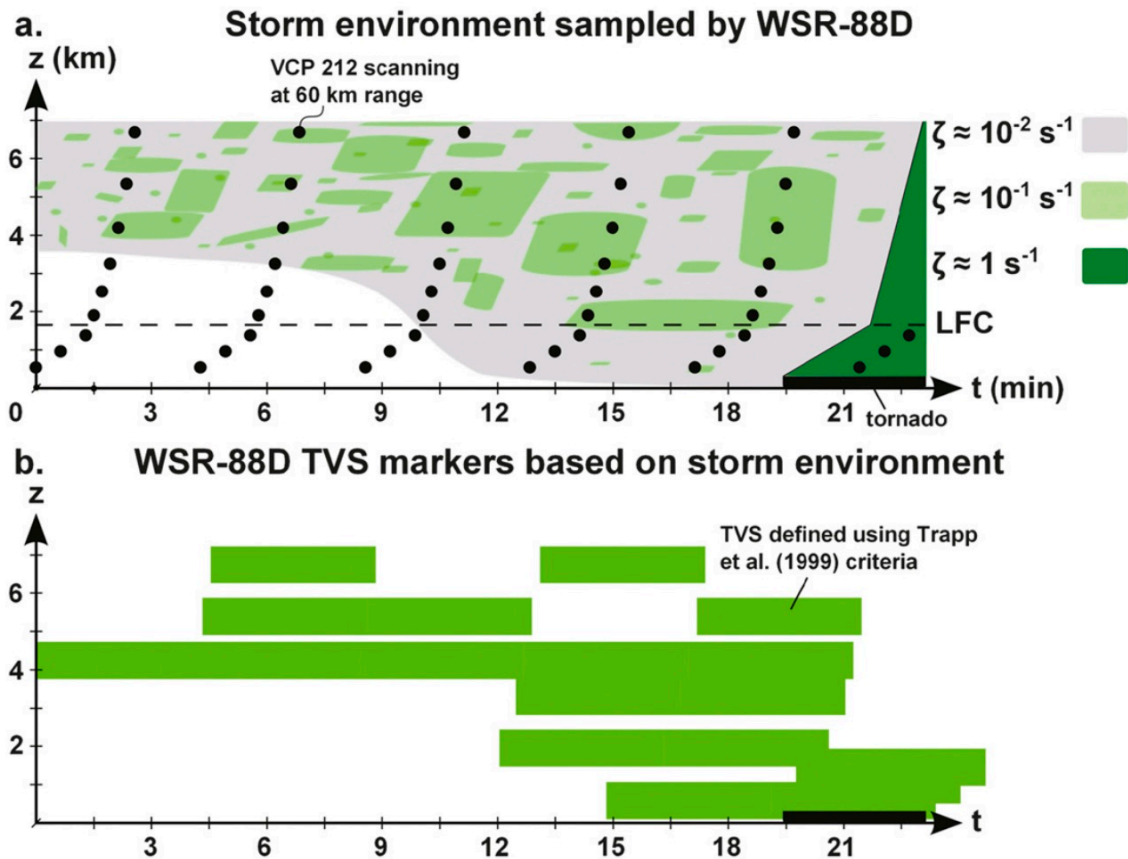
Figure 2.3: An illustration, based loosely on the Goshen County supercell, of how enhanced levels of vertical vorticity within a mid- and low-level mesocyclone might appear as a descending incipient tornado in WSR-88D data. The black bar indicates a tornado and the dotted horizontal line marks the level of free convection. Gray (dark green) shading represents mesocyclone-scale (tornadic) vertical vorticity. Light green shading highlights areas (top) of locally enhanced vertical vorticity as discussed in the text and (bottom) where the Trapp et al. (1999) TVS criteria are met based on the given vertical vorticity distribution. The black dots indicate the approximate center beam locations from a WSR-88D scanning a storm 60km away using VCP 212. Reprinted from French et al. (2013).

Perhaps one of the most notable papers on the topic is work by French et al. (2013). This study worked with three data sets from MWR-05XP, which found one case with a persistent low-level TVS and contraction (consistent with Alexander 2010) while the other two TVSs ascended with time. Further, the study made the determination that the descending TVS feature was an artifact of the poor temporal resolution found with

17

WSR-88Ds (Fig. 2.3). This misidentification was largely attributed to large changes in the TVSs ΔV that were observed in MWR-05XP data occurring over a "period of time an order of magnitude faster than the WSR-88D volumetric update time" (French et al. 2013). This helped to further cement that tornadogenesis was a rapidly-evolving process in contrast to the longer time required for tornadogenesis via the DPE.

While current research suggests that mode II (non-descending) from Trapp and Davies-Jones (1997) is the likely manner in which TVS intensification occurs, a recent study by Houser et al. (2022) has some substantial implications worth considering. Their work highlighted the lack of a formal definition of what makes a vortex "tornadic" and notes the challenge in developing consistent, quantitative criteria for TVS identification. As a range of thresholds exist across the literature, even within literature utilizing mobile radar data, there is a subjective aspect associated with finding the best fit of threshold for each study. One of the conclusions in this work states that "the interpretation of results may be a function of the methodology, and it raises the question of when should rotation be considered 'tornadic'" (Houser et al. 2022). This determination has often been based on visual reports of a tornado, which might or might not be reliable. While their sample size remains small and is biased towards one supercell undergoing cyclic tornadogenesis, they did find TVSs appearing via descending (one case), non-descending (five cases), and both (one case) modes of TVS intensification according to their tested set of criteria.

2.2 Rapid-Scan PAR Data and Forecaster Response

An S-band PAR previously located at the National Weather Radar Testbed in Norman, Oklahoma, has served as a testing ground for the development of phased array technology for meteorological applications (Curtis and Torres 2011; Heinselman

and Torres 2011; Yu et al. 2007; Zrnić et al. 2007). Studies have shown the PAR was capable of collecting better samples of rapidly evolving severe weather events in comparison to the WSR-88D radars (e.g., Emersic et al. 2011; Heinselman et al. 2008; Newman and Heinselman 2012). One notable challenge addressed by these studies was based on interviews with NWS forecasters in the southern plains. They stated that forecasters might know how a storm was likely evolving by applying the conceptual models they were familiar with, but that the volumetric update times of WSR-88Ds could not capture some of the trends they expected to see.

Heinselman et al. (2012) described the long-term goal for PAR technology as one that seeks "to understand how new weather radar information provided by rapid scanning might benefit the decision making of NWS warning forecasters." This led to the advent of several PARISE studies, as described in Chapter 1. Results from the 2010 PARISE were described in Heinselman et al. (2012), which assessed responses to 43-s and 4.5-min volumetric update times in team scenarios, with one time assigned to each. These cases focused on EF-0 and EF-1 tornadoes often missed in warning operations.

In the study, the 43-s team was able to quickly provide and update warnings on the correct storm for the correct threat using a radar-driven approach. They also noted they were much more confident in comparison to the usual confidence reported by the 4.5-min team. However, the use of this 43-s data did result in an increased number of false alarms. One 43-s team noted that "they were comfortable using the rapid-update data during the case because fluid motions matched their expectation of seeing circulations cycling up and down, and that increased their confidence..." (Heinselman et al. 2012).

Another PARISE was conducted in 2012, with the primary goal of examining the validity of the findings with PARISE 2010 (Heinselman et al. 2015). In this case,
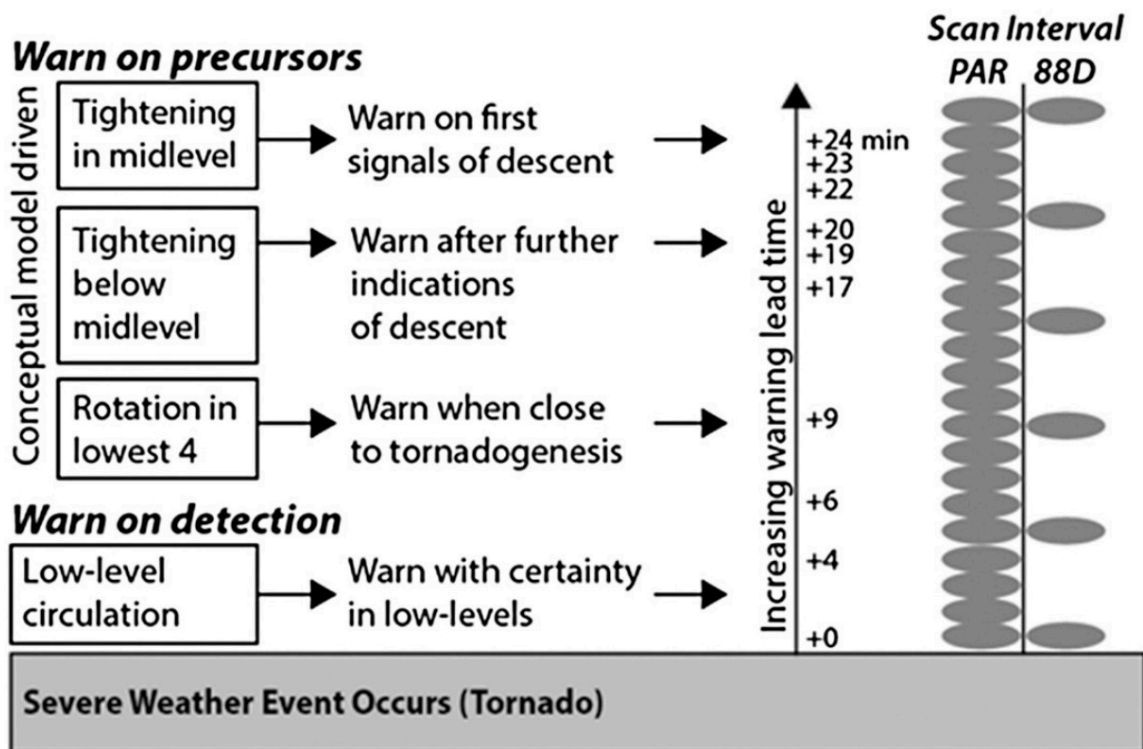
Figure 2.4: Forecasters using rapid-temporal, full-volumetric PAR data had multiple scans upon which to confidently identify the persistence of features aloft that preceded tornadogenesis. Differences in warning decisions were then driven by their personal thresholds for location and strength of key features. Reprinted from Heinselman et al. (2015).

the PAR data were generally found to improve knowledge of rapid-evolution within a storm while increasing confidence and reducing stress. However, one of the youngest forecasters in this experiment found that, while the additional data increased his confidence in warning, it did not help with his decision time, and he issued a warning too late. In general though, the forecasters were able to adapt the conceptual models and workflows they were familiar with to make decisions while issuing their warnings with the PAR data (Fig. 2.4). Ultimately, the rapid-scan capabilities from the PAR data better allowed for addressing earlier concerns related to applying conceptual models without sufficient radar data to support those notions. The study found a 20-min median tornado warning lead time - exceeding the national average lead time for weak

tornado cases (that are often not observed or warned well) by 7 min (Heinselman et al. 2015).

Kuster et al. (2015) sought to build upon the work done by Heinselman et al. (2012, 2015), by focusing on a higher-end tornado event. Reaffirming previous work, the higher temporal resolution offered by the PAR data (70-s) versus the Oklahoma City, Oklahoma, WSR-88D (4.58-min) allowed for a better analysis of several important features, including: low- and mid-level mesocyclone cycles, rapid intensification of the low-level mesocyclone and TVS, and changes in tornado motion and location. These results were contrary to initial expectations expressed in the study that the rapid updates may be less beneficial because environmental cues are typically supportive of tornadoes preceding strong tornado cases (Kuster et al. 2015). Nonetheless, the work remains promising in showing the utility of PAR data across the range of tornadoes found in the United States.

The 2015 PARISE expanded to include severe wind and hail events and increased the sample size of forecasters, regions, and cases to improve the generalization of findings (Bowden et al. 2015; Wilson et al. 2017a). Building upon the results focused on tornadoes in Heinselman et al. (2015), Bowden et al. (2015) found a statistically significant increase in lead time for severe thunderstorm warnings when 1-min update PAR updates were provided. A follow-up study by Bowden and Heinselman (2016) not only tested the use of 2-min PAR updates but also found the increase in lead time for severe thunderstorm warnings was driven by the ability of forecasters to observe radar-based precursors earlier when using 1-min vs 5-min volumetric updates. In addition to analyzing warning performance, cognitive workload of forecasters was also analyzed Wilson et al. (2017a). Using subjective instantaneous self-assessment levels, this study showed a skew towards higher cognitive workload at faster temporal resolutions. However, it was found that the experience of a cognitive overload was rare.

The 2015 PARISE was the first to feature focus groups, which allowed forecasters to share their thoughts and experiences of using the rapid-update PAR data (Wilson et al. 2017b). Results from those groups provided considerations for integrating and using this rapidly-updating data into operations such as the feasibility of new algorithms, prioritizing attention to a primary threat, and hands-on training for rapidly-updating radar data. Following a pilot study by Wilson et al. (2016), an eye-tracking study was also conducted during the 2015 PARISE. Results from this study in Wilson et al. (2018) found little difference in the fixation patterns and attention distributions of forecasters at 1- or 5-min PAR updates. However, this was attributed to the chosen weather scenario, and Wilson et al. (2018) further noted that additional work to understand fixation measures for more dynamic events may be useful in continuing operational meteorology research.

Chapter 3

Data & Methodology

3.1 Data

This section will provide relevant background information on the radar system that collected the data sets used in this study.

3.1.1 RaXPol

The data used for each of the cases analyzed in this study were all collected by RaX-Pol (Fig. 3.1). RaXPol is a mobile, 3-cm wavelength, dual-polarization radar system operated by the University of Oklahoma with unique capabilities designed around the need for rapid temporal resolution while maintaining a high level of spatial resolution to aid in the study of rapidly evolving convective phenomena. Its high-speed pedestal enables antenna rotation speeds of up to $180° \text{ s}^{-1}$ resulting in volumetric update times of $\sim$16–20 s for 8–10 elevation angles. In comparison to the 2–3 min volumetric update times of other mobile systems such as the Shared Mobile Atmospheric Research and Teaching (SMART; Biggerstaff et al. 2005) radars and most of the DOWs, it is RaX-Pol's combination of dual-polarization and rapid-scan capabilities that distinguishes its utility in observing rapidly evolving meteorological phenomena. To collect observations at such a high speed and mitigate spatial resolution degradation, a signal transmission and reception technique known as frequency hopping is employed. For this frequency

diversity technique (Doviak and Zrnić 2006), the radar transmits a sequence of uniformly spaced pulse-pair signals that, to increase the independence across samples in a shorter time than without this technique, are shifted in frequency by at least the pulse bandwidth (Pazmany et al. 2013).

Figure 3.1: An image of the Rapid X-Band Polarimetric Radar (RaXPol) on deployment, courtesy of Dr. David Bodine

This radar also has the same half-power beamwidth of $\sim 1°$ found within the WSR-88D network. When the radar is operating in rapid-scan mode, there is beam smearing that produces an effective beamwidth of $\sim 1.5°$. Using this same $1°$ 'pencil beam' maintains a similar resolution of observed storms and hazards across the two different systems, with the acknowledgement of some additional limitations for the X-band system (e.g., attenuation and rapid-scan beam smearing). Table 3.1 summarizes some of RaXPol's key system parameters adapted from Table 1 of Pazmany et al. (2013), which the reader is also referred to for a complete discussion of RaXPol's specifications and capabilities.

Table 3.1: A selection of RaXPol's key system parameters and specifications. Adapted from Pazmany et al. (2013).

Parameter	Value
Center frequency	9.73 GHz $\pm$ 20 MHz
Transmit power	20 kW peak, 200 W avg
Transmit pulse width	0.1–40 µs
PRT	Uniform or staggered
Antenna diameter	2.4 m
Half-power antenna gain	44.5 dB
Maximum pedestal scan rate	$180° \text{ s}^{-1}$ azimuthal; $36° \text{ s}^{-1}$ elevation
Range gate spacing	7.5–75 m
Receiver bandwidth	0.5–40 MHz, or custom

Data from RaXPol were chosen for this study as they are an excellent candidate to serve as the basis for creating synthetic PAR data to emulate future all-digital PAR benefits. This is due to the higher temporal resolution of the system in addition to the low-level and spatial sampling capabilities that the system offers. With data of this quality, the synthetic PAR tool can be confidently applied with the resulting synthetic data used to investigate and analyze the benefits that a future operational PAR network may offer.

3.1.2 Case Information

For this study, data are analyzed from two cases observed by RaXPol. Each of these cases is discussed in their respective sections which follow.

3.1.2.1 Case I: 24 May 2011 El Reno, OK Tornado

On 24 May 2011, 16 tornadoes impacted the state of Oklahoma. Of these tornadoes, three were violent and impacted the greater Oklahoma City metropolitan area. The El Reno, OK EF-5 tornado was one of the three violent (i.e., EF-4 or EF-5) tornadoes on this day.
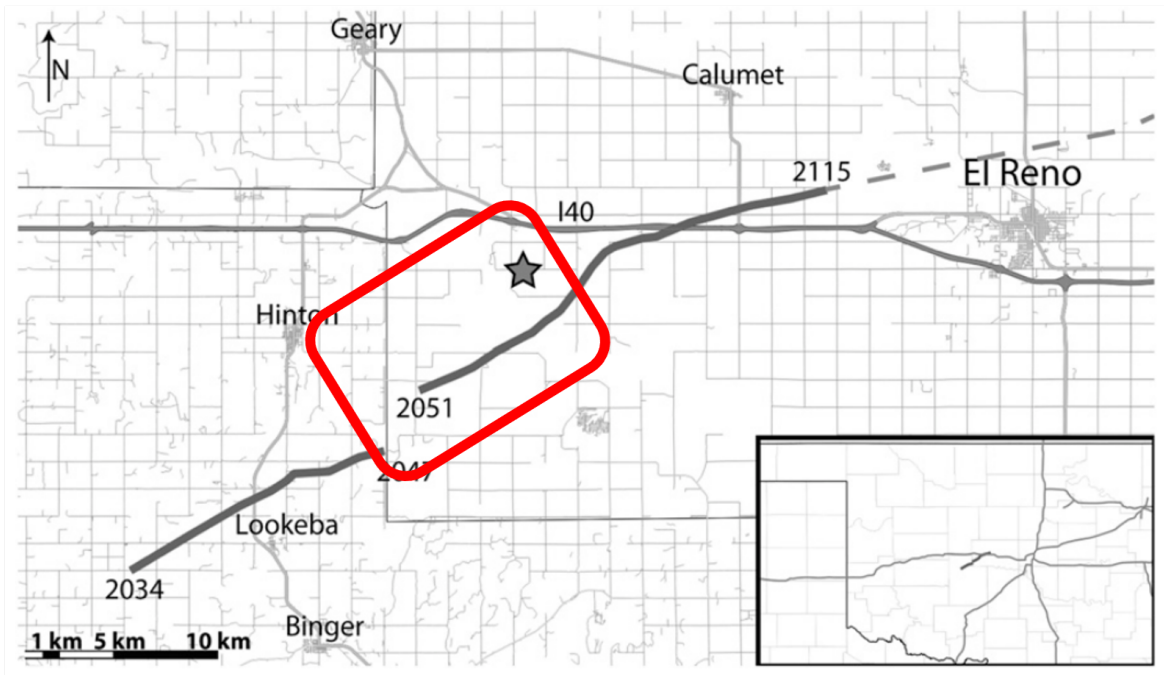
Figure 3.2: Annotated version of Figure 1 from Houser et al. (2015) showing the Lookeba, OK and El Reno, OK tornado tracks and RaXPol's location (black star) on 24 May 2011. The red box outlines the time period discussed in this study.

In this study, the analysis focuses on the time period from 2047–2055 UTC. During this period, RaXPol data collected by Dr. Howard Bluestein's research group are used to observe the development of a new mesocyclone following a previous tornado (Lookeba, OK EF-3 tornado; Houser et al. 2015), tornadogenesis, and subsequent intensification. An annotated version of Figure 1 from Houser et al. (2015) is shown as Figure 3.2 with the red annotations highlighting the time period this study analyzes.

This case used a scanning strategy that provides volume scans covering eight elevation angles (4–18° every 2°) approximately every 17 s. There are a couple of limitations that exist within the data set. The lowest elevation angle available in a volume is 4° (making lowest elevation ∼800 m above ground level or AGL), and following tornadogenesis there is a brief period of data missing at 2052 UTC for a change in scanning strategy (for specifics, see Houser et al. 2015, 2016). For the purposes of this project (explained further in Section 3.2.1), it is important to consider the range gate spacing and range resolution of the data that were collected. To best emulate the 250 m range resolution of a WSR-88D radar, this information guides the spatial averaging within the synthetic PAR data tool. This information and a range of distances from RaXPol to the tornado are provided in Table 3.2.

Table 3.2: Range gate spacing and distance between RaXPol and tornado for both Case I and Case II.

Event	Tornado # (as applicable)	Time	Range Gate Spacing	Distance Between RaXPol & Tornado
Case I		2047–2052 UTC	75 m	∼7.5–12.5 km
Case I		2052–2055 UTC	15 m	∼4.5–7.5 km
Case II	4	2319–2322 UTC	30 m	∼6.5–7.0 km
Case II	5	2321–2326 UTC	30 m	∼6.5–7.5 km

For discussion on the Lookeba, OK tornado as well as additional analysis of observations and the evolution of polarimetric signatures (e.g., TDS: tornadic debris signature) seen with the El Reno, OK tornado, the reader is directed to Houser et al. (2015, 2016).

3.1.2.2 Case II: 24 May 2016 Dodge City, KS Tornadoes

On 24 May 2016, a cyclic supercell thunderstorm produced 13 tornadoes over the course of 90 min near Dodge City, Kansas, as the storm underwent at least four complete mesocylogenesis "cycles" (e.g., Adlerman et al. 1999; Burgess et al. 1992; Dowell and Bluestein 2002). While a majority were weak and short-lived, there were a few stronger (EF-2 or greater) tornadoes with each mesocyclone responsible for one stronger tornado. Of the 13 tornadoes (four mesocyclones) produced by this supercell, nine (three mesocyclones) were directly observed with RaXPol (by Dr. Howard Bluestein's research group) across two deployment sites, and seven of those had their full life cycles observed. A map showing the deployment locations and estimated 13 tornado tracks from Wienhoff et al. (2020) with annotations specific to this study is provided as Figure 3.3. Specifically, RaXPol collected direct observations of tornadoes 1 and 3–10 indicated on the figure. The remaining tornadoes were either reported by storm chasers, visually confirmed by the RaXPol crew, or confirmed by a post-storm damage survey.

For this case, the focus is on tornadoes 4 and 5 as identified in Figure 3.3. Following post-storm damage surveys, tornadoes 4 and 5 were rated as an EF-0 and EF-2, respectively. Tornado 4 was only recorded for ∼45–60 s, but its entire lifespan from genesis to decay was captured by RaXPol. Tornado 5 was the strongest tornado for which tornadogenesis was observed by RaXPol during this deployment. Additionally, these tornadoes occurred in close succession from the same mesocyclone (M-2 in Figure 3.3). Observations from other supercells which underwent cyclic tornadogenesis have been found to have weaker, short-lived tornadoes preceding a longer-lived, potentially stronger tornado (Dowell and Bluestein 2002). In the case of mesocyclone 2, there is evidence this process occurred across three tornadoes (2–4) before tornado 5. While
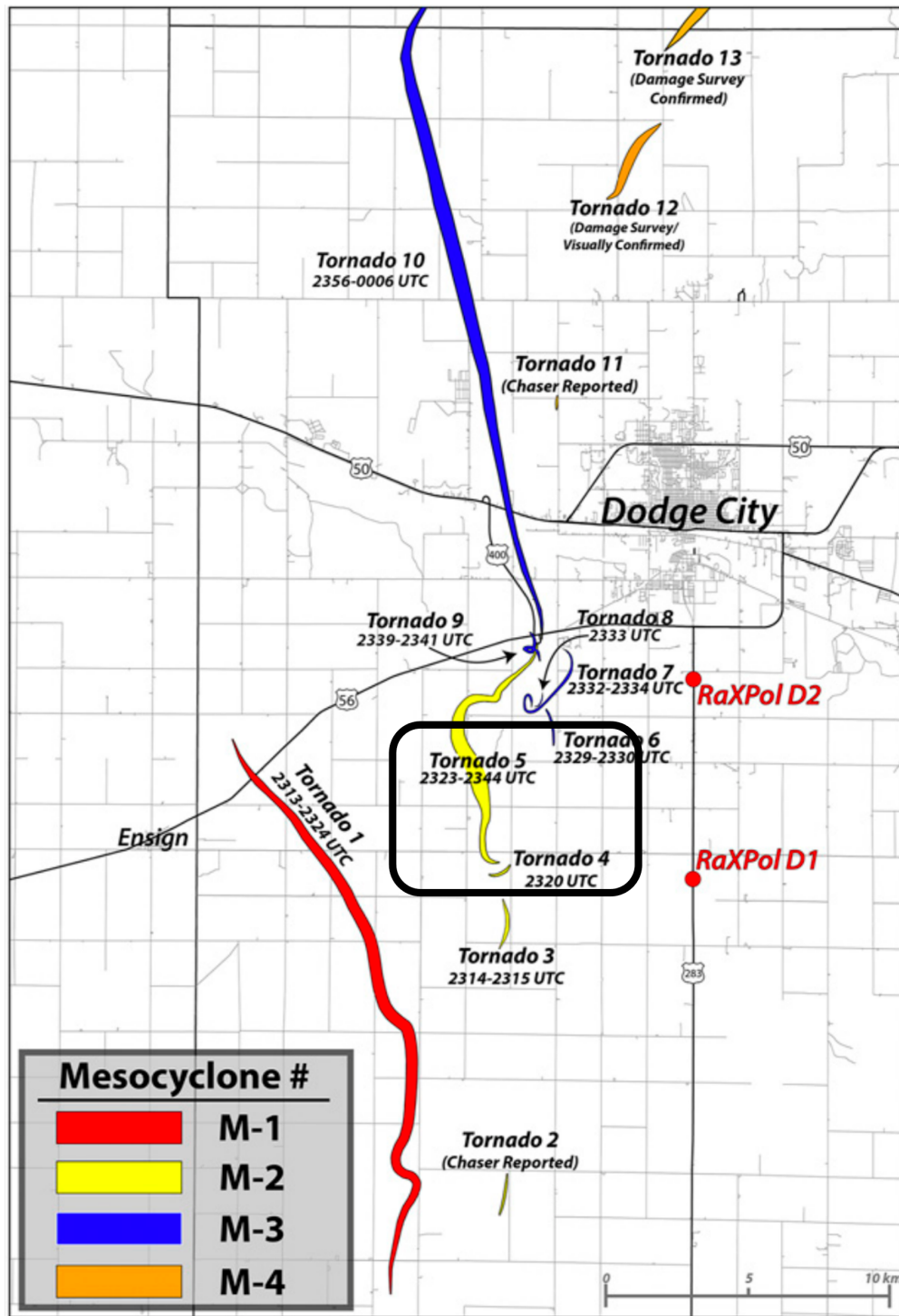
Figure 3.3: Annotated version of Figure 4 from Wienhoff et al. (2020) showing the tracks of 13 estimated tornadoes produced by four different mesocyclones (color coded). RaXPol deployment sites 1 and 2 are indicated with red dots and labeled as RaXPol D1 & RaXPol D2 respectively. The black box outlines the time period discussed in this study.

29

outside of the scope of this study, similar observations are supportive of the same process occurring with mesocyclone 3 before the formation of tornado 10.

The scanning strategy in this case varied across and within each of the individual deployments. For both of the tornadoes discussed in this study, volume scans covering seven elevation angles (0–6° every 1°) are completed every 17–20 s. Similar to case I, a summary of the range gate spacing used during data collection is provided in Table 3.2. Notably, given the shorter distance between the tornado and RaXPol, a finer range gate spacing was used as there was not a need to increase radar sensitivity for a longer range with coarser range gate spacing (e.g., case I's first time period).

While also for the sake of brevity, the decision to include only discussion for one of the weak tornadoes is due to largely similar results found across these weaker tornadoes. For a complete analysis of the TDS characteristics and evolution across most tornadoes from this event's RaXPol deployment, the reader is referred to Wienhoff et al. (2020).

3.2 Methodology

For both cases, a variety of tools have been used to perform analyses. The synthetic PAR data tool has been a primary focus of this work allowing for simulation of longer standoff ranges similar to WSR-88D's long-range scans as well as one PAR enabled scanning strategy: focusing. An operational radar is unlikely to collect observations with the resolution of a mobile radar, so the synthetic PAR tool enables the unique capability to use high spatio-temporal resolution data from RaXPol to emulate the capabilities of a future operational PAR. Additional tools allowed for more streamlined, consistent, and repeatable collection of relevant data and calculated parameters (e.g., ΔV) across both the original and synthetic PAR data. The most used tools and methods for this study are further discussed in the following subsections.

3.2.1   Synthetic PAR Data Tool

To best analyze the benefits a future operational PAR network may offer using RaXPol data, slight modification of data sets described in Section 3.1.2 is required. In this study, spatial degradation via a spatial averaging scheme is conducted to emulate longer standoff ranges. By doing so, the close-range (e.g., < 10 km) data can be used to emulate what would be seen at the longer standoff range (e.g., 60 km). The resulting data are termed synthetic PAR data in this study. A visual overview of this tool's process and application to sample data is provided as Figure 3.4, and a more detailed written description follows below.

The first step in creating the synthetic PAR data is to ingest the data into the tool. Although this study focuses on RaXPol data, the synthetic PAR data tool has been designed to be flexible for use with data from other radar systems. Provided data are in a netCDF/CFRadial file format with variable dimensions of (azimuth, range) or (range, azimuth) - or can be easily converted - those data can be processed via this tool. For this study, synthetic PAR data of radar reflectivity factor (Z) and radial velocity (V_r) are generated to analyze the TVS directly. Although the examination of other polarimetric variables and signatures (e.g., ρ_{hv} and TDS) is outside of the scope of this study, it is an area for future work.

This tool does not presently have the capability to perform automated velocity dealiasing. Therefore, all data must be quality checked and confirmed to be dealiased along with clutter filtering applied, as needed, before being input into this tool. The data sets used in this study were both previously dealiased as presented in Houser et al. (2015) and Wienhoff et al. (2020). Once formatted correctly and prepared for conversion, the data are input into the synthetic PAR tool as is.
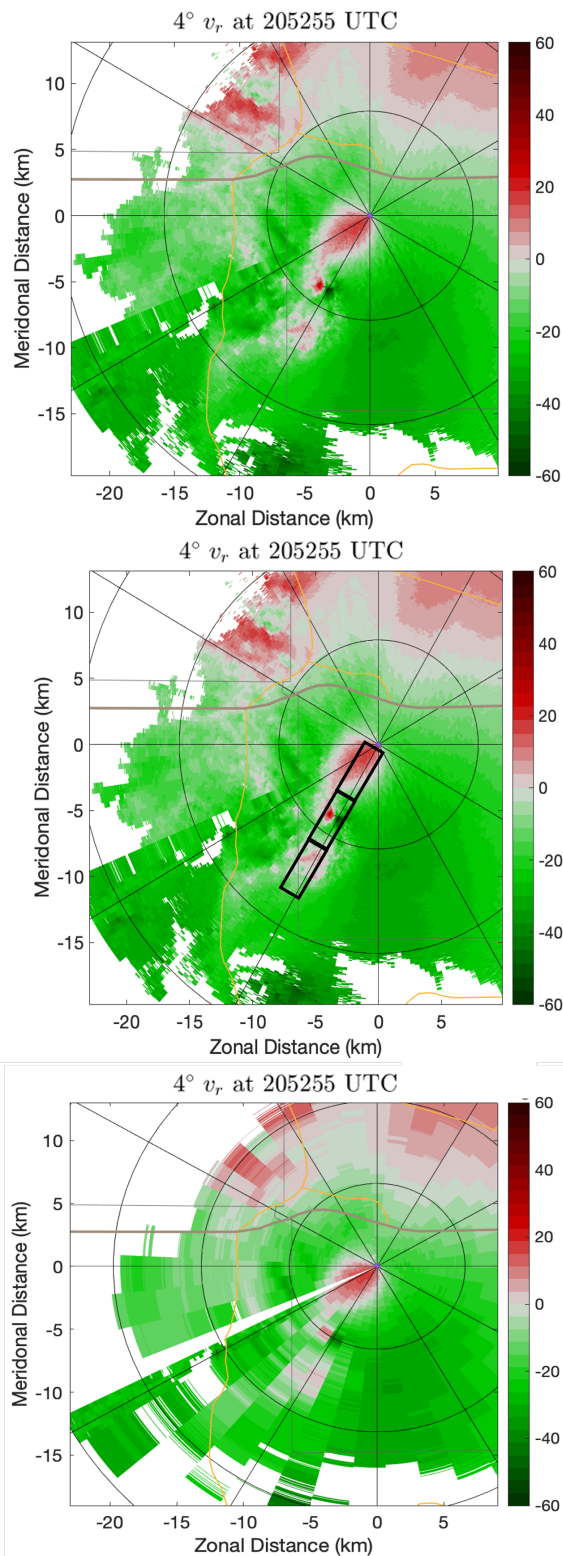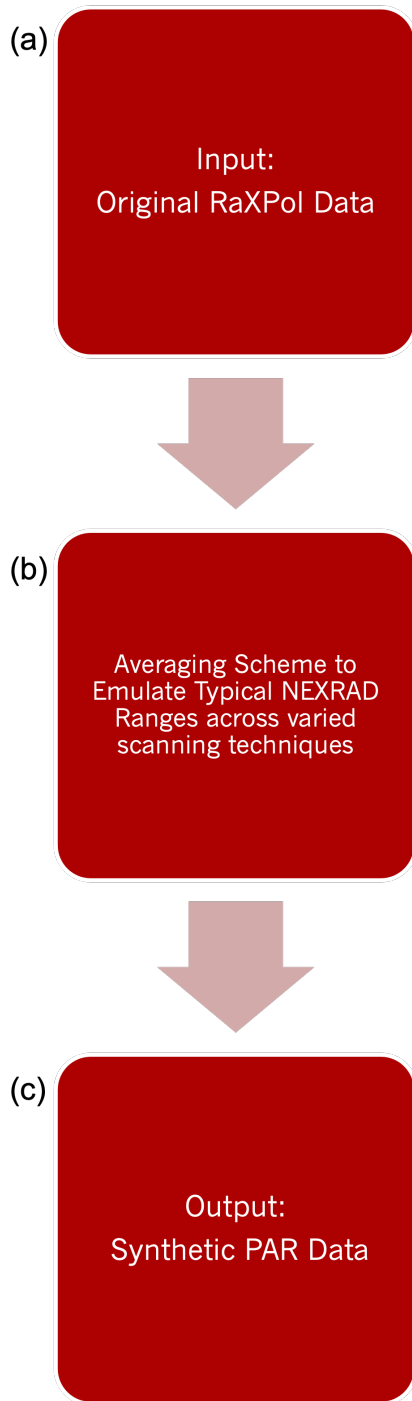
Figure 3.4: A visual overview of the synthetic PAR data tool (left) and PPIs showing the steps on a sample case emulating a typical WSR-88D standoff range of 80 km using the 4° V$_r$ from 2052:55 UTC in the El Reno, OK case (right).

The tool has the ability to perform several independent or combined techniques in the generation of synthetic PAR data. To emulate longer WSR-88D standoff ranges, spatial degradation is conducted by applying spatial averaging across both the range gates and azimuth. Averaging occurs across the range gates in order to match the WSR-88D radar range gate spacing of 250 m as closely as possible. For example, using the range gate spacing of 30 m from either tornado in case II (see Table 3.2), averaging is completed across eight range gates to emulate a 240 m range gate spacing. Azimuthal averaging is also performed to emulate how a 1° beamwidth WSR-88D would observe the TVS at a longer standoff range. For example, assuming the distance between RaXPol and the TVS is 10 km and the user decides to average across 8° in azimuth, an 80-km standoff range will be emulated. While the data sets used in this study prevent a perfect match to the WSR-88D specifications, the spatially degraded data remain a close representation of longer-range data one might see from these radars. The tool does not presently account for minimum beam altitude changes as a result of Earth's curvature (i.e., denial of low-level observations at longer standoff ranges). This would have an impact on detecting some of the trends analyzed at increasing standoff ranges. Thus, this is a limitation of the conclusions presented, especially with respect to the identification of TVS intensification methods. However, this study was primarily motivated to identify the presence of a TVS with long-range, coarse resolution data with this limitation to be addressed in continuing work.

In the current version of this tool, the user inputs the number of range gates and azimuths on which to average spatially. The tool then performs averages within regions fitting those parameters like the illustrative boxes drawn on the PPI shown in Figure 3.4(b)'s right column. For example, an calculation over three range gates and four azimuths results in 12 total gates to be averaged. As will be further discussed in Chapters 4 and 5, this can have important implications to consider for the TVS as

standoff range is increased. The tool does not presently account for antenna weighting pattern (i.e., decreased weighting farther from the center of the beam) beyond the effects already present in the original data. Since Doppler velocities are a power-weighted average of scatterers' radial velocities, an additional consideration is made here with respect to reflectivity weighting of Doppler velocities. Velocities associated with higher Z are more "important" than velocities associated with lower Z, which is similar to how this process works naturally where V_r is weighted toward high Z scatterers in the volume (Doviak and Zrnić 2006). A notable limitation exists in this spatial averaging scheme. To truly emulate a NEXRAD radar, the same spatial degradation would need to also be applied in elevation. However, given the close proximity of RaXPol to the observed TVSs, the data necessary to perform this averaging (especially at longer standoff ranges) is not available. The addition of data sets with greater vertical extent in observations would enable this spatial degradation to be applied in elevation as well.

The synthetic PAR data tool is also capable of emulating one PAR-enabled, adaptive scanning strategy: focusing. The radar tool can apply the focusing strategy to the original or synthetic PAR data. A user specified azimuth of interest is used to emulate a focusing scan by updating a 45° azimuthal sector (created by ±22.5° azimuth around the user provided azimuth) at an increased rate and updating the rest of the azimuths (i.e., those outside the focusing sector) at a slower rate. The simulations analyzed in this study have updated the specified sector approximately at 20-s intervals and updated the entire PPI approximately every 1 min. Both the sector size and the update times may be changed to meet user needs, but these values were chosen based on expected PAR operational capabilities. Of note, there is some drawback to emulating this scanning mode with mobile radar data. As these radars are often deployed in close-range and providing targeted observations of one storm, they essentially already provide the benefit of this mode to an operational network. Thus, in this study,

although focusing will continue to show the benefits of having increased temporal resolution, it is limited in showing the utility of targeting one storm or region of interest in a multi-storm or quasi-linear convective system (QLCS) scenario more likely to be observed by WSR-88Ds.

After being processed through the technique(s) selected by the user, the data (currently not back to netCDF/CFRadial) and/or images created by the tool are saved for the user to analyze. An example PPI showing the impacts of long standoff ranges is provided on the right column of Figure 3.4(c). The synthetic PAR data tool remains a flexible framework capable of continued expansion and refinement of its current emulated scanning techniques and WSR-88D standoff ranges. Some of the planned future additions to this tool are discussed in Chapter 6.

3.2.2 TVS Tool

Built into the visualization for RaXPol's data, the TVS tool was designed to allow for streamlined and consistent collection of the specific data relevant to this study. The tool relies on code within the visualization tool where range and azimuth are converted to Cartesian coordinates for plotting. The user clicks the location of the TVS, and then specifies a range outward from the TVS from which to collect data. Upon completing these two steps, the tool will automatically save a file with Z, V_r, diffrential reflectivity (Z_{DR}), correlation coefficient (ρ_{hv}), the selected (x,y) points, and a few tool-specific variables such as the array used to select values only in the defined radius.

The most recent iteration of this tool allows users to go back and re-capture variables not originally saved using the same threshold and selected (x,y) points. This ensures consistency in the location that variables are collected from in an otherwise subjective process. This iteration also allows the use of the same (x,y) points but recalculated to capture a different radius threshold to confirm that the TVS was completely captured.

This study uses the traditional proxy of ΔV for the rotational intensity of the TVS, calculated as the difference between maximum outbound and inbound V_r measurements. The final step of the TVS tool calculates the ΔV. The consistency and flexibility of this tool has allowed the minimization of subjectivity introducing error with respect to finding these maximum values for this calculation.

3.2.3   Simulating Increased Temporal Resolution

In order to answer the questions related to temporal impacts of a future PAR network, varied temporal resolutions are simulated by introducing a delay between volumetric updates. Two approaches are investigated to understand the impacts of varied temporal resolutions: (1) providing a comparison to current WSR-88D radar capabilities and (2) understanding the benefits of different temporal update rates for operations (in line with the future system requirements outlined in National Weather Service 2015). In order to simulate different volume scan times, volumes of data are removed to temporally downsample the observations. With RaXPol data providing volumetric updates approximately every 17–20 s, the exact time can between simulated volumes can vary slightly as with actual operational radars. In this study, we simulate the increased time to complete a volumetric update by removing volumes of data until the desired update time is achieved (i.e., removing one volume to simulate an update taking 20 s longer).

To assess the first point, this study simulates WSR-88D observations occurring on a 5-min volumetric update time. While updates on VCPs 12/212 can update volumes every $\sim$4–4.5 min (i.e., faster volume updates compared to the 5-min benchmark update time), this update time seems reasonable to use beyond just for the sake of simplicity. Due to the fact that VCPs 12/212 often are also running with MESO-SAILS or SAILS, which can be implemented to provide up to three supplemental low-level scans, these

additional scans can actually increase the time required to complete a full volumetric update. Therefore, a slightly longer update time still fits the project goals well. Additional studies may be done to emulate the slightly faster 4–4.5 min updates as well as the additional low-level data.

Given the requirements of the next radar network to have a volumetric update time of 1-min or less (National Weather Service 2015), the second point assesses a few PAR enabled temporal resolutions. In this study, analysis is conducted at 20-s, 40-s, and 60-s update times to capture a range of potential capabilities by an operational PAR. While the replacement radar must meet these requirements, the 'rapid-scan' like capabilities provided by faster updates might have utility with certain scanning strategies or during high-impact storms. Thus, while a 1 min volumetric update time seems likely with the next operational radar network, the results from this study could be used to guide developing scanning strategies which leverage this increased temporal resolution on a case-by-case basis.

Chapter 4

Case I: 24 May 2011 El Reno, OK Tornado

This chapter details the results and discussion related to the 24 May 2011 El Reno, OK, case. Each of the previously mentioned focus areas for this study have their own sections in this chapter.

4.1 Spatial Resolution Impacts

The primary analysis related to spatial resolution impacts is centered around the rotational intensity of the TVS. This analysis is important in order to determine if there is still a benefit to rapid-scan radar observations at coarse resolutions. As discussed in Section 3.2.2, this analysis utilizes the traditional proxy of ΔV. In order to best understand the impacts of the synthetic PAR data tool's various capabilities, analysis is first performed on the original data set.

In the original data set (Fig. 4.1), observations show that across the time period prior to tornadogenesis, as indicated via a tornadic-velocity threshold at 2051:05 UTC (vertical black line), the mid- and upper-level ΔV of the mesocyclone remained notably weaker until the tornado formed. An exception to this is found around 2048-2049 UTC when there is an area of higher ΔV indicating stronger rotation aloft from approximately 2.5 km above ground level (AGL) and above.
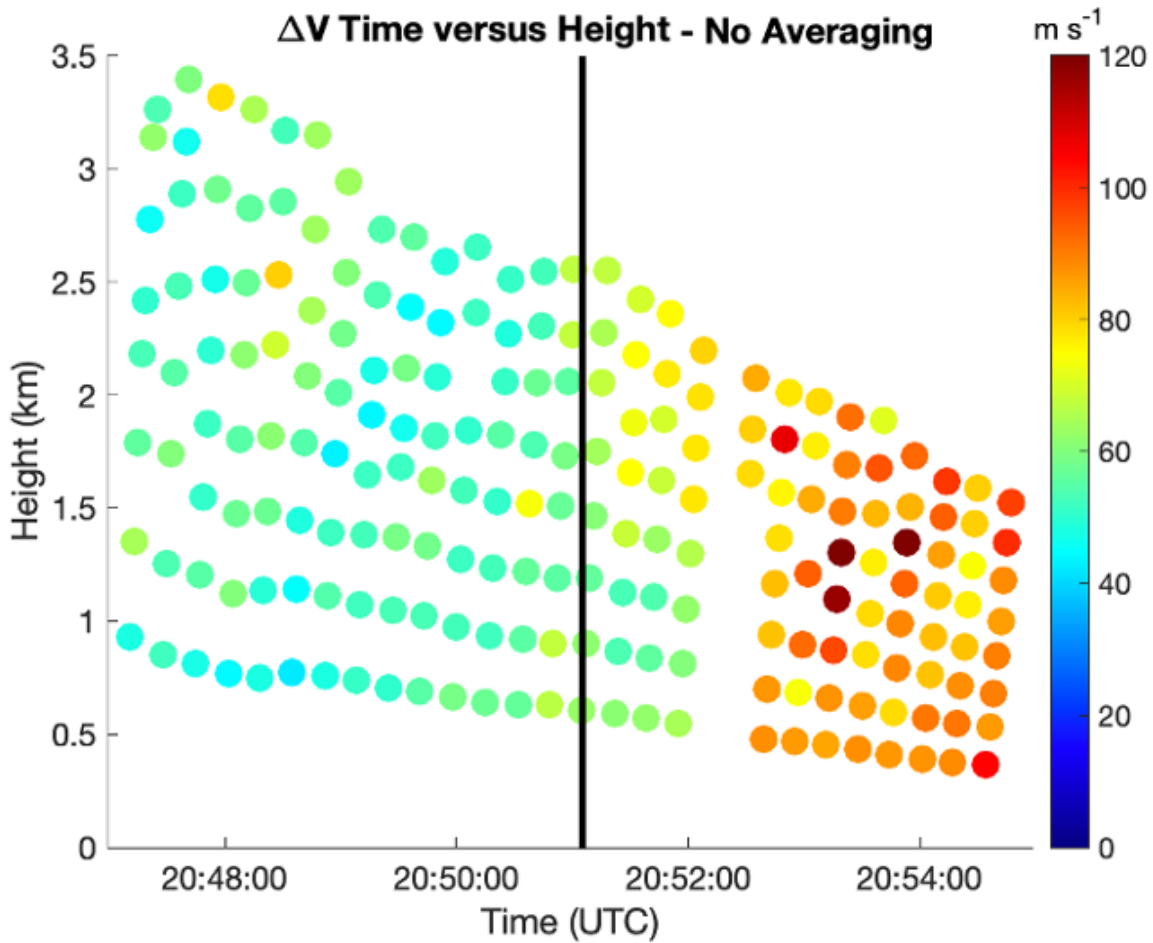
Figure 4.1: ΔV as a function of time and height on the original 24 May 2011 El Reno, OK data set. The vertical black line represents the time at which all velocities are >55 m s^{-1} indicating tornadogenesis has occurred as in Houser et al. (2015).

At 2049:41 UTC, ΔV at the low levels – around 0.8 km AGL – begins to steadily increase. Tornadogenesis occurs shortly after 2051 UTC as the entire column (in contrast to the rotation found from 2048-2049 UTC) has rotation that exceeds a tornadic-velocity threshold of 55 m s^{-1} consistent with that used in Houser et al. (2015). Subsequent to tornadogenesis, there is a marked increase in ΔV to values exceeding 70-80 m s^{-1} across the entire depth of data within 2 min. All ΔV surpassed the 55 m s^{-1} tornadic-velocity threshold within a volume scan update time of $\sim$17 s indicating a TVS forming in a nearly simultaneous manner across the entire depth of the data.

39

The rapid evolution of the observed successful tornadogenesis is notable. Without the fast update times of a radar like RaXPol, these processes would have been missed completely on a WSR-88D. Additionally, this would support the work completed by French et al. (2013) suggesting that a descending TVS may be an artifact of insufficient temporal resolution. Thus, this rapid tornadogenesis suggests that updates on a faster temporal scale are needed to properly observe tornado formation. This will be further explored in Section 4.2.

Synthetic PAR data emulating a representative 20-km standoff range serves as the basis for the next ΔV analysis (Fig. 4.2). To create these data, spatial averaging is performed across three or 16 range gates (as discussed in Section 3.2.1) and 2° in azimuth. For simplicity, the single representative 20-km standoff range value is used. By stating that the TVS was found to be approximately 10 km away from RaXPol for most of the data analyzed here, this spatial averaging set-up emulates of how a 1° beamwidth radar would observe this tornado at the 20-km standoff range. However, there is an inherent interval of standoff ranges (9–25 km) since the tornado did move closer to RaXPol. An average reduction of about 7 m s^{-1} in the ΔV is observed in the data emulated at this standoff range.

The first observation of the 20 km ΔV (Fig. 4.2) is the decrease in ΔV due to the spatial degradation performed to produce the synthetic data. Despite this decrease in magnitude, the vertical evolution of the TVS is similar to that seen in the original data set (Fig. 4.1). At the beginning of the time series, an area of higher ΔV around 55-65 m s^{-1} is seen at heights of 2.5 km and above. Shortly after 2049 UTC, this area of higher ΔV diminishes until tornadogenesis occurs. Thus, the observation of transient intensification of the low- and mid-level mesocyclone (though there is little change in the low-level vortex below 1 km AGL) is captured when simulating this 20-km standoff
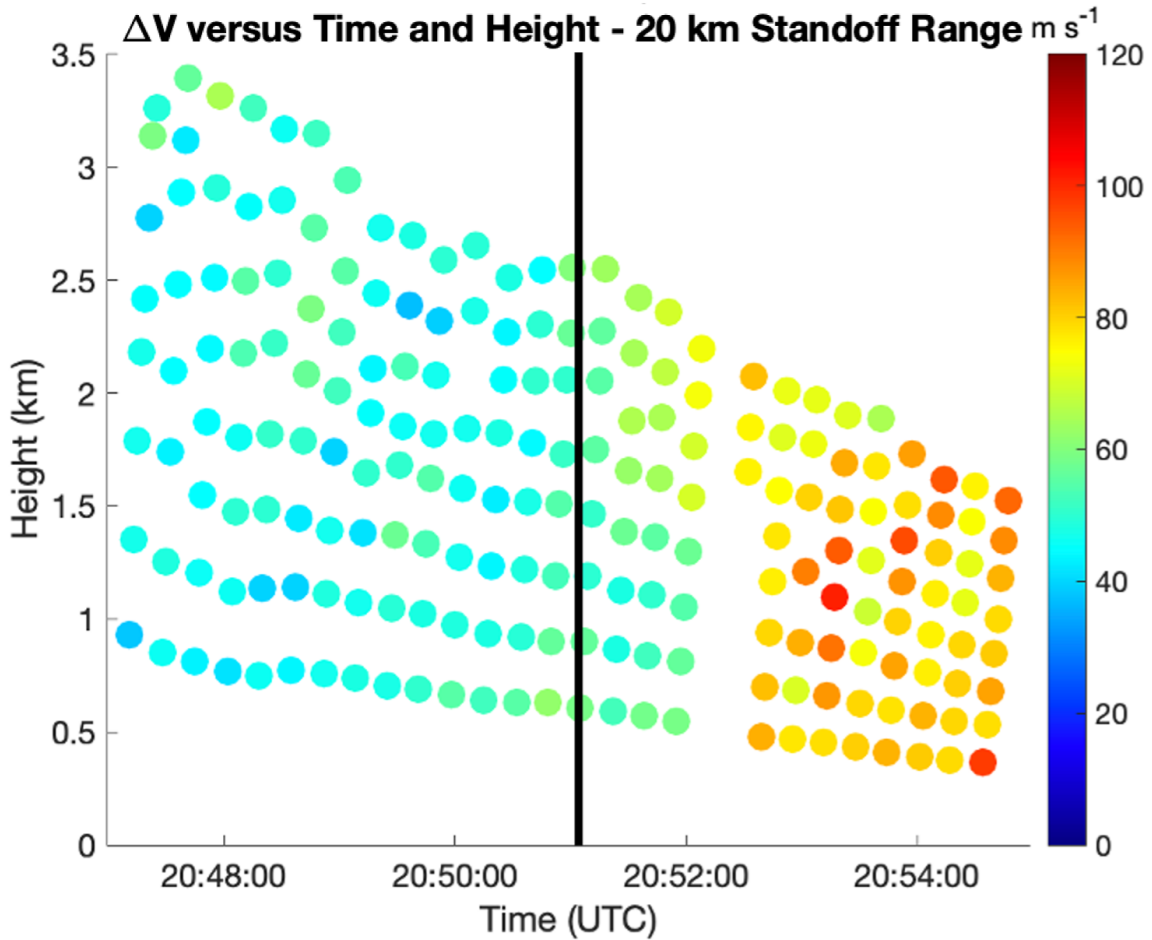
Figure 4.2: As in Figure 4.1, but here showing the ΔV for an emulated 20-km standoff range.

range. While this could possibly be identified as a failed tornadogenesis case since there was intensification of the mesocyclone, there was a lack of evidence that the low-level rotation was simultaneously intensifying to otherwise support tornadogenesis.

The vertical black line for assessing tornadogenesis via ΔV exceeding a tornadic-velocity threshold remains at 2051:05 UTC. Here, a tornadic-velocity threshold of 55 m s^{-1} can primarily be used to identify tornadogenesis has occurred. A few exceptions exist where some data points are just below the threshold (by $\sim$3 m s^{-1}) at the 6° and 8° elevation angles before strengthening above the threshold within two volume

updates (or approximately 34 s). However, it becomes important to consider changes to the tornadic-velocity threshold selected, especially as this value can change from event to event as well as from coarser spatial resolution (e.g., broader beamwidth or greater distance between the radar and tornado; Alexander and Wurman 2008; French et al. 2013). Consistent with previous work, it seems reasonable to account for this and slightly lower the threshold to 50 m s^{-1}, as this reduction is well within the average decrease in ΔV at this standoff range. Thus, TVS formation still appears to be occurring in a nearly simultaneous manner across the entire depth of data despite reduced ΔV.

The same qualitative trend in rapid intensification is evident after the formation of the tornado beginning around 2052:32-2052:39 UTC. Across the remainder of the time series, ΔV remain high with few exceptions around 1-1.5 km and the 18° elevation angle (~1.6 km AGL). Again, this process occurs extremely rapidly and well under the typical WSR-88D update time (within ~2 min) suggesting the need for and the importance of faster temporal updates than currently provided by operational radars. Nonetheless, it is encouraging to see the same qualitative trends leading up to and following tornadogenesis despite the decreased spatial resolution in the data set.

Synthetic PAR data emulating a representative 80-km standoff range serves as the final ΔV analysis. Trends in ΔV at this standoff range indicate a large degradation in the spatial resolution of the data at this point (Fig. 4.3). For the 80-km standoff range, analysis is being completed on data that is more representative of a mesocyclone scale (beam spread of ~1.4 km). Qualitative analysis of planned position indicator (PPI) scans show data that is significantly degraded in terms of spatial resolution and observed TVSs identified in previous standoff ranges and the original data are much broader and weaker than reasonably expected for tornadoes.
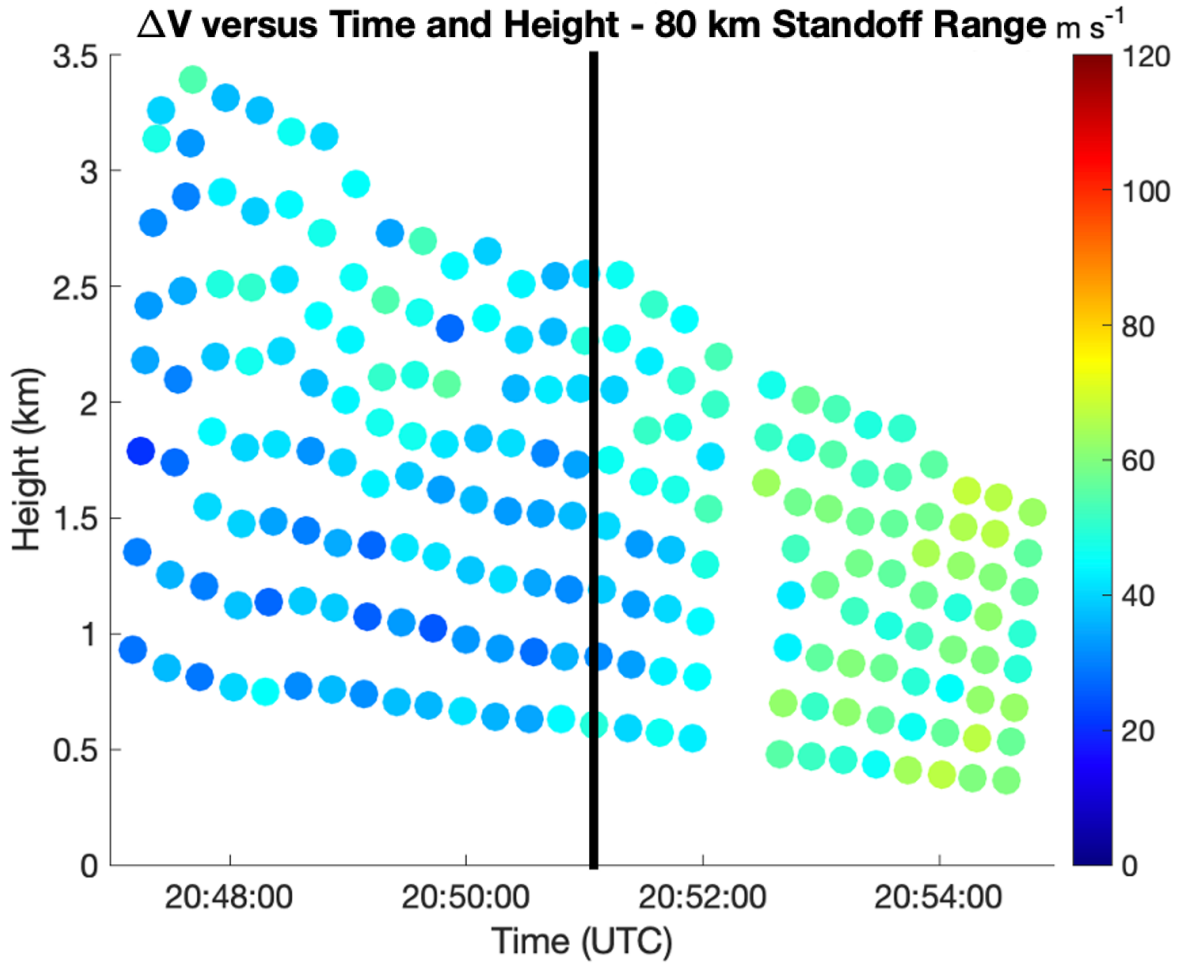
Figure 4.3: As in Figure 4.1, but here showing the ΔV for an emulated 80-km standoff range.

A look at the quantitative trends observed in the data set show some disparity between the ΔV before and after tornadogenesis. In the time before tornadogenesis at 2051:05 UTC, there was a reduction from the original ΔV by $\sim$16 m s^{-1} whereas this increased to $\sim$29 m s^{-1} for the time period after tornadogenesis (after 2051:05 UTC). A probable reason for this discrepancy is related to the structure of the velocity field before and after tornadogenesis occurs. Before tornadogenesis, relatively broad rotation is apparent, and thus spatial averaging has less impact compared to after tornadogenesis when the vortex is smaller. By considering that more widespread weaker

velocities were surrounding a tight radial velocity couplet existing over only a 1.5 km horizontal distance (thus a small region of higher values in comparison to the averaged area), it makes sense for these otherwise high ΔV to be degraded more.

Nonetheless, despite this significant degradation and change of scale, there are important features found in the data. There is still evidence of brief upper-level intensification during the 2048-2049 UTC time frame. Similar to the original data and the 20-km standoff range, the figure itself shows this area of higher ΔV (50-55 m s^{-1}) at and above 2.5 km AGL with predominantly weaker ΔV (25-35 m s^{-1} with some locally higher values) found at the middle and lower levels, again supportive of a lack of sufficient rotation at these levels to support tornadogenesis.

A consideration for this standoff range is the reduction of the tornadic-velocity threshold before moving any further down the time series. There is no support for a threshold of 55 m s^{-1} as there were no ΔV at the original tornadogenesis time higher than this threshold and even fewer than 40% of data points above this threshold after tornadogenesis. A reduction to 40 m s^{-1} for the tornadic-velocity threshold seems appropriate here and is in line with previous studies using this speed as the lower bound for ΔV tornadic-velocity thresholds. When applied to this data set, all of the points are above this reduced threshold just one volumetric update slower (2051:22 UTC) than in the original data set (2051:05 UTC). While the intensification across the entire depth of the column is already supportive of ascending or nearly simultaneous TVS intensification, further evidence can be derived from the shorter temporal scale that this intensification occurred on compared to the longer timescale expected for descending tornadogenesis via the dynamic pipe effect. This pairs with the need for and importance of rapid temporal updates, as using a volumetric update time customary of the WSR-88D radars (e.g., approximately 5 min) would have likely tagged this as

the opposite formation mechanism providing further support of French et al. (2013) findings.

After 2052 UTC, the intensification is still clear albeit with much lower ΔV. Here, most values are around 55-65 m s^{-1} within $\sim$2 min of tornadogenesis and continue to increase in strength as the end of the time series is reached. Despite this coarse resolution exhibiting a short ($\sim$17 s) delay in the identification of features from the original data, the overall results and qualitative trends for this 80-km standoff range are remarkable. These observations seem to show that tornado-scale (observed in the RaXPol data and shorter standard simulated data) and mesocyclone-scale rotation are intensifying at roughly the same rate (the tornado-scale ΔV is still affecting the ΔV in the 80 km data, so some influence is to be expected).

To aid the reader in better understanding and interpreting the output of data from the synthetic PAR data tool, several PPIs of Z and V$_r$ are provided (Figs. 4.4 and 4.5). Additionally, they provide the same visual that a forecaster would have available to them when making warning decisions. Three columns of PPIs are provided with one showing the original data and the other two showing data at the standoff ranges used so far in this discussion.

The PPIs of Z (Fig. 4.4) confirm that the impacts of spatial averaging increase the coarseness of data the most at longer standoff ranges. While the data at 20-km appear to be largely similar to the original data, there is a notable decrease in the resolution at the 80-km standoff range. Here, while most of the storm's structure remains intact, it does become increasingly difficult to pinpoint the location of the hook echo. However, one can use some of the nearby structure and knowledge of supercells to reasonably find where this feature may be. In spite of the reduced resolution, even at this long standoff range, the data available for analysis remain more valuable than initially expected in this study.

The PPIs of V_r (Fig. 4.5) share similar findings as those above. The identification of a velocity couplet is easiest with the original and 20-km standoff range data, but it remains possible to identify it in the coarse data as well. Although, in this case, it appears that the most intense circulation is present at the 16° elevation angle. The ease in finding this couplet, however, does underscore the potentially promising use of future operational PARs to resolve tornadic velocity couplets even at far ranges.

4.2   Temporal Resolution Impacts

Another goal of this study is to suggest a temporal resolution that would perform well for analyzing rapidly evolving severe hazards on an operational PAR system. NWS forecasters have also discussed their desire for faster update times between radar volumes, which has been improved by the development of new VCPs and other changes to scanning strategies (e.g., MESO-SAILS) in recent years. Previous work by Kingfield and French (2022) and Cho et al. (2022), NWS forecasters desires (e.g., Heinselman et al. 2012, 2015), and the goal of this research are key motivating factors in exploring optimal temporal resolutions for a future operational PAR network. The need for this has also been evidenced throughout Section 4.1 of this chapter. As analyses of ΔV in Section 4.1 showed the difference in temporal scales between tornadogenesis failure and success, temporal resolution will be an important consideration for any future PAR network with respect to tornadoes. The project/system objectives for an operational PAR, with respect to temporal resolution, state a goal of 60 s or less for volumetric update times (Weber et al. 2021). As the following analysis will show, this seems sufficient while continuing to improve temporal resolution will provide even greater insight to severe hazard evolution.
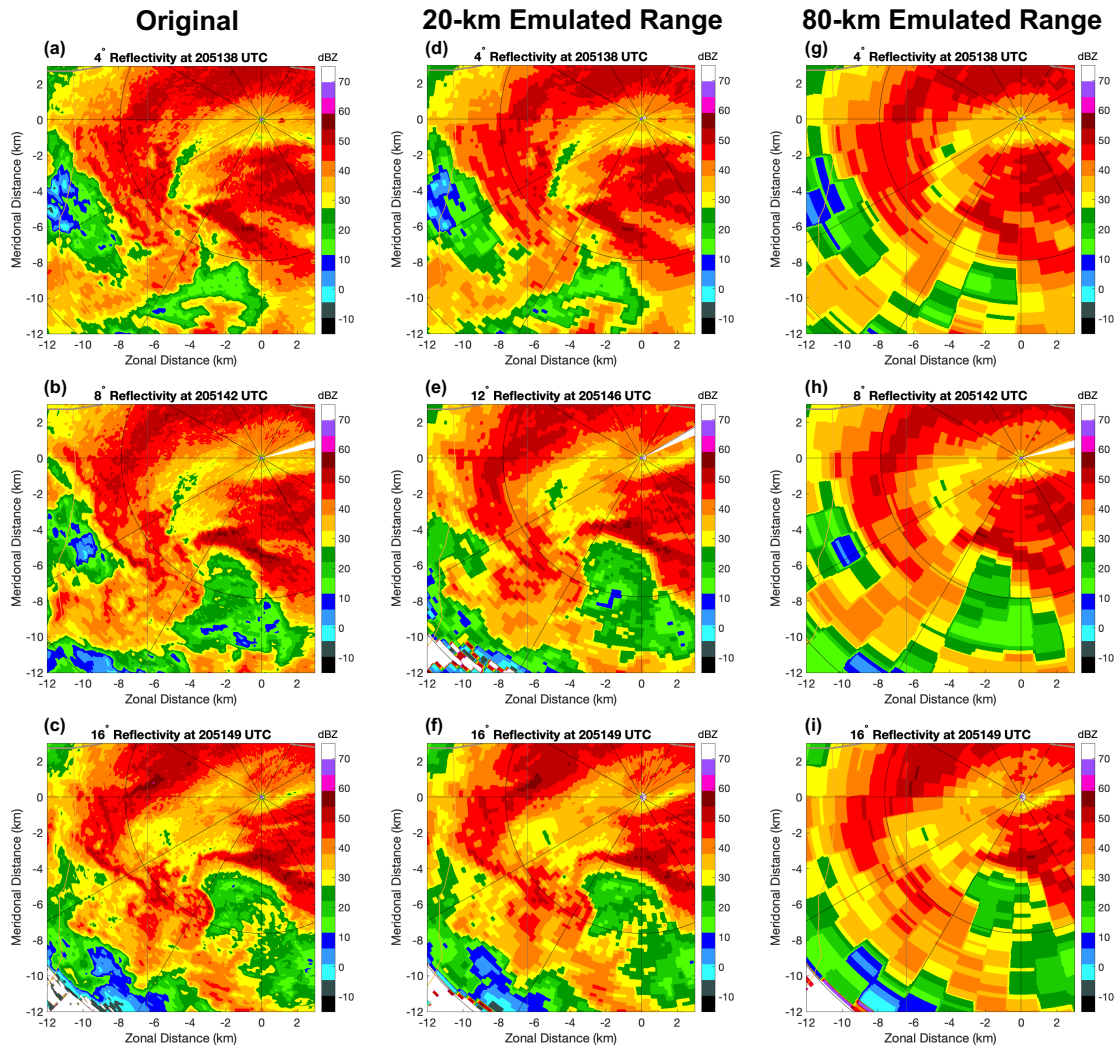
Figure 4.4: PPIs of Z at the 4°, 8°, and 16° elevation angles on 24 May 2011 at 2051:38 UTC, 2051:42 UTC, and 2051:49 UTC in each row, respectively. Three labeled columns separate the original RaXPol data (left), data at a 20-km emulated standoff range (middle), and data at an 80-km emulated standoff range (right) for each of the elevation angles.
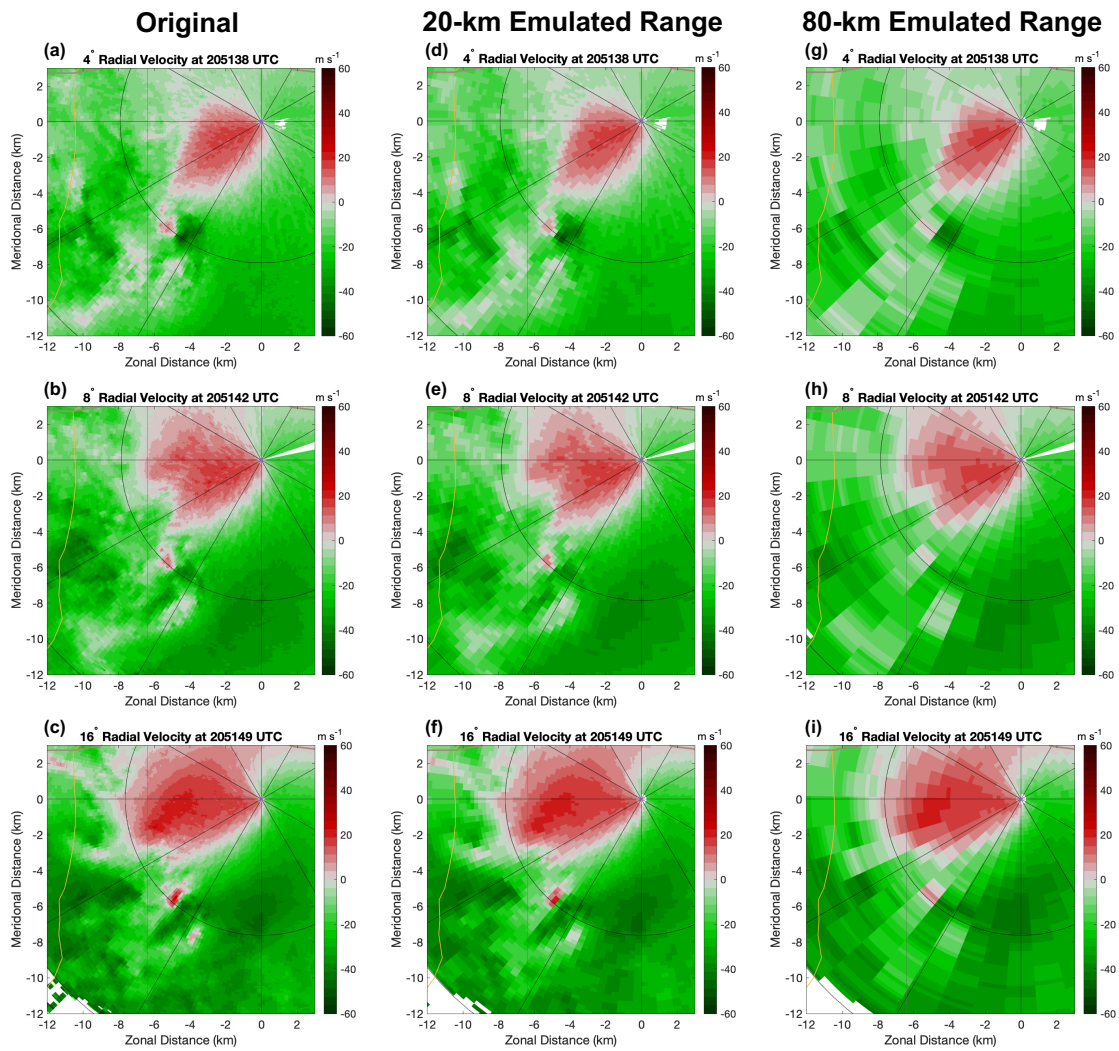
Figure 4.5: As in Figure 4.4, but here PPIs of V_r.
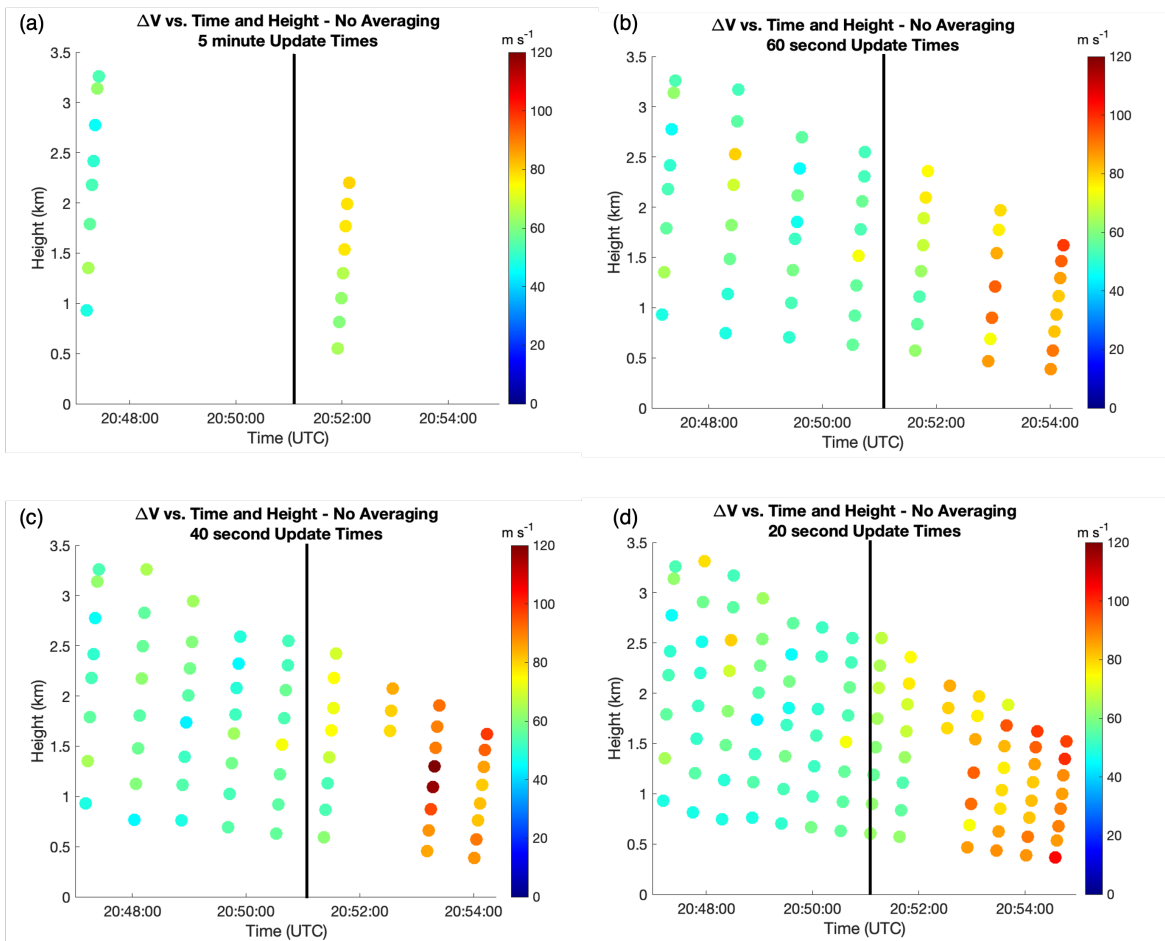
Figure 4.6: ΔV as a function of time and height on the original 24 May 2011 El Reno, OK data set. The vertical black line represents the time at which all velocities are >55 m s^{-1} indicating tornadogenesis has occurred. Data are temporally downsampled to provide volumetric updates on temporal scales of every (a) 5 min, (b) 60 s, (c) 40 s, and (d) 20 s.

The impacts of temporal downsampling are first applied to the original data set (Fig 4.6). Four different volumetric update times whereas the base RaXPol dataset has an update time of ∼17 s in the data set. Panels (a)-(d) of Figure 4.6 show 5-min, 60-s, 40-s, and 20-s updates, respectively. Specifics on quantitative ΔV values and noted areas of tornadogenesis success and failure are discussed in detail within Section 4.1 and will not be covered here. The analysis discussed here will instead be from a more qualitative perspective. To examine the benefit of rapid-scan observations,

49

a comparison to 5-min updates is first presented to explore how the TVS would be sampled, in time at least, by a WSR-88D (Fig. 4.6). The first observation is that there are many fewer data points to analyze. Two volumes of data are available using such a slow update time. The radar observations miss critical moments of the mesocyclone development and successful tornadogenesis. If a slight adjustment to the starting time of the 5-min update period was made to instead begin around the already discussed 2048–2049 UTC upper-level intensification period, our next volumetric update would suggest a tornado was on the ground already. Tornadogenesis would thus appear to be occurring via descending TVS intensification rather than the ascending or nearly simultaneous TVS intensification pattern seen in the full RaXPol data examined by this study. Consistent with previous work from French et al. (2013), this appears to be an artifact of temporal aliasing (or at least a result of severe undersampling in time).

To analyze the minimum system requirement of a future operational PAR, a comparison to 60-s updates is presented (Fig. 4.6(b)). While the data here are more sparse in comparison to that found in Figure 4.6(c) and 4.6(d), it is a vast improvement over the data available with 5-min volumetric update times. In direct contrast to those slower update times, it remains possible to identify a strengthening low-level mesocyclone leading up to tornadogenesis (2049:41 & 2050:49 UTC). Observing the brief upper-level intensification early on in the time series is a bit more difficult, however, given there is only one volumetric update within the 2048–2049 UTC window it occurred in. While the exact time of tornadogenesis is not captured here, it is evident that the intensification of ΔV, and thus the ensuing TVS, is occurring in a nearly simultaneous manner with successful tornadogenesis occurring. The 60-s updates also provides better insight than the 5-min updates on how quickly the tornado is intensifying across all heights after tornadogenesis. Despite being slower than the two faster update times (discussed in the following paragraphs), the processes leading towards

tornadogenesis and the rapid intensification which followed are generally observable here. However, there are still some instances (e.g., the volume scans preceding and following 2052 UTC) where there are large changes in ΔV hinting at rapidly occurring evolution that is not captured. In this case, the data here struggle to capture the actual formation of a TVS until a tornado is on the ground and intensifying.

A faster temporal resolution possible with an operational PAR is 40-s (Fig 4.6(c)). While fewer volumes of data are available to analyze than with 20-s updates (Fig. 4.6(d)), the most important features our analysis is focused on are still evident. The tornadogenesis failure that is observed around 2048-2049 UTC is evident with the enhanced upper level ΔV over a low-level area of weaker ΔV values. Leading up to tornadogenesis, the intensification of a low-level mesocyclone is seen with this 40-s update time. With this crucial step captured within the data, tornadogenesis is still evidenced to be occurring via an ascending or simultaneous TVS intensification method. The trend in rapid intensification following tornadogenesis is also quite clear with the volumes updated at this temporal resolution. As with the 20-s updates, there are still a large number of volume updates that provide information about the atmospheric processes occurring when sampled at 40-s.

The final temporal resolution of 20-s (Fig. 4.6(d)) is the fastest operational PAR possibility that is analyzed in this study. Here, there is an abundance of data available to analyze. All of the areas of interest in this analysis are presented and can be seen across the time series from tornadogenesis failure to tornadogenesis success and subsequent intensification. Analysis performed here would still support the finding from above that TVS intensification is occurring in an ascending or nearly simultaneous manner. The intensification process is also well sampled. The high number of complete volumes (13) available across the time series provides a more clear depiction of the

processes leading to the formation and subsequent intensification of the tornado on an appropriate time scale.
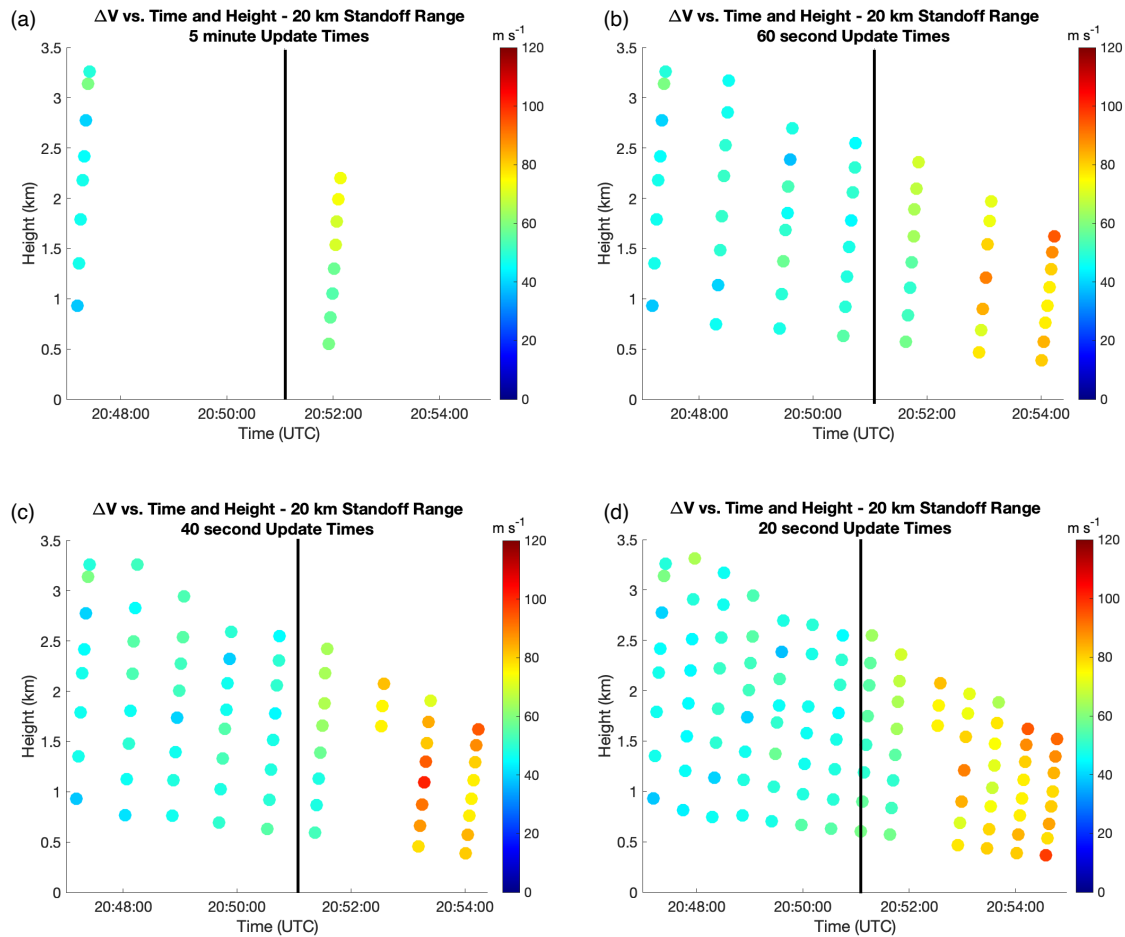
Figure 4.7: As in Figure 4.6, but here for ΔV for an emulated 20-km standoff range.

With analysis of the original data set complete, the 20-km standoff range ΔV is examined next (Fig. 4.7). Examining how the TVS would be sampled by a WSR-88D 4.7(a), there is again an obvious lack of volumetric data available at the current WSR-88D update time. In the first volume, there are ΔV around 40-45 m s^{-1} and greater across most of the column (1.5 km and above). The next volume shows ΔV continuing to increase, with the strongest ΔV still around 1.5 km and above. All points are still above a tornadic-velocity threshold of 55 m s^{-1} in this volume. In both volumes, the

52

highest ΔV are found around 1.5 km and above. However, the vertical extent of our samples is now more shallow ($\sim$3.3 km to $\sim$2.2 km) and is slightly closer to the surface ($\sim$0.9 km to $\sim$0.5 km) as the TVS moved closer to RaXPol. Comparing the ΔV values by altitude, the greatest intensification is found around 1.5 km by $\sim$26 m s^{-1} in 5 min. Intensification is still found closer to the surface noted by a range of ΔV increases of $\sim$10–22 m s^{-1} in 5 min at similar altitudes. This trend seems to suggest the column is intensifying nearly simultaneously at most altitudes, but an additional volume may be helpful in identifying if the strongest rotation originates around 1.5 km and descends in this case. Thus, at this temporal resolution, it is difficult to definitively resolve the method of TVS intensification.

The minimum system requirement of 60-s provides the next stage of analysis again (Fig. 4.7(b)). The data are once again limited in comparison to the 20-s and 40-s update times. However, sufficient data still exist to identify important features that are missed at the WSR-88D update time (with the exception of the early tornadogenesis failure as mentioned already in this section). Looking at the volume scans leading up to and immediately after tornadogenesis occurs, there remains evidence of TVS intensification in an ascending or nearly simultaneous manner. The intensification process is sampled well here as well. Even without the volumes available at faster update times, there is little question that this tornado is undergoing rapid intensification shortly after it is formed. Thus, despite not being the fastest update time simulated here, the updates provided with 60-s volumetric updates are much more informative.

Simulating temporal resolutions faster than the system requirement begins again at 40-s (Fig. 4.7(c)). The data remain a marked improvement to those shown in Figure 4.7(a). Again, at the time of the earlier tornadogenesis failure, updates show enhanced winds aloft before weakening briefly and intensifying at the lowest levels and eventually through the entire depth of data leading up to tornadogenesis. The volume

scan leading up to and after tornadogenesis provide support for identification of TVS intensification in an ascending or nearly simultaneous manner at this standoff range and temporal update time. After the data gap at 2052 UTC, the rapid intensification of this tornado is evident. With some of the intermediary data now removed as a result of the slower update time, ΔV jumps from around 50–65 m s^{-1} to around 75–80+ m s^{-1} over $\sim$40 s. This rapid intensification is exactly why faster temporal updates are necessary for severe hazards.

The fastest temporal resolution examined is once again 20-s (Fig. 4.7(d)). Data at this temporal resolution do introduce some doubt as to the TVS intensification found with tornadogenesis in this case. This is largely driven by the inherent gap in data sampling during the scanning strategy change. However, there does appear to be support that the TVS might be classified as downward intensification as higher ΔV (65–70 m s^{-1}) are located at or above 2 km AGL with lower ΔV found below. By the next complete volume scan at 2053:28 UTC, the data have all reached a more similar ΔV across the column. The rapid nature of the tornadogenesis process is well captured and lends support to the faster radar update time simulated. Intensification is also still clear from the data at this standoff range when sampled at a 20-s update time. The small amount of data removed from collecting volumes at this update rate do not have a significant impact on identifying the ongoing tornadic intensification by the end of this time series.

A final temporal resolution analysis is conducted using ΔV from the 80-km standoff range (Fig. 4.8). The lack of data are once again easy to identify amongst the remaining panels which offer greater insight into what is happening across the plotted time series. Using the lower threshold and delay mentioned in Section 4.1 for the 80-km standoff range, the second volume of data shown represents an area of nearly simultaneous
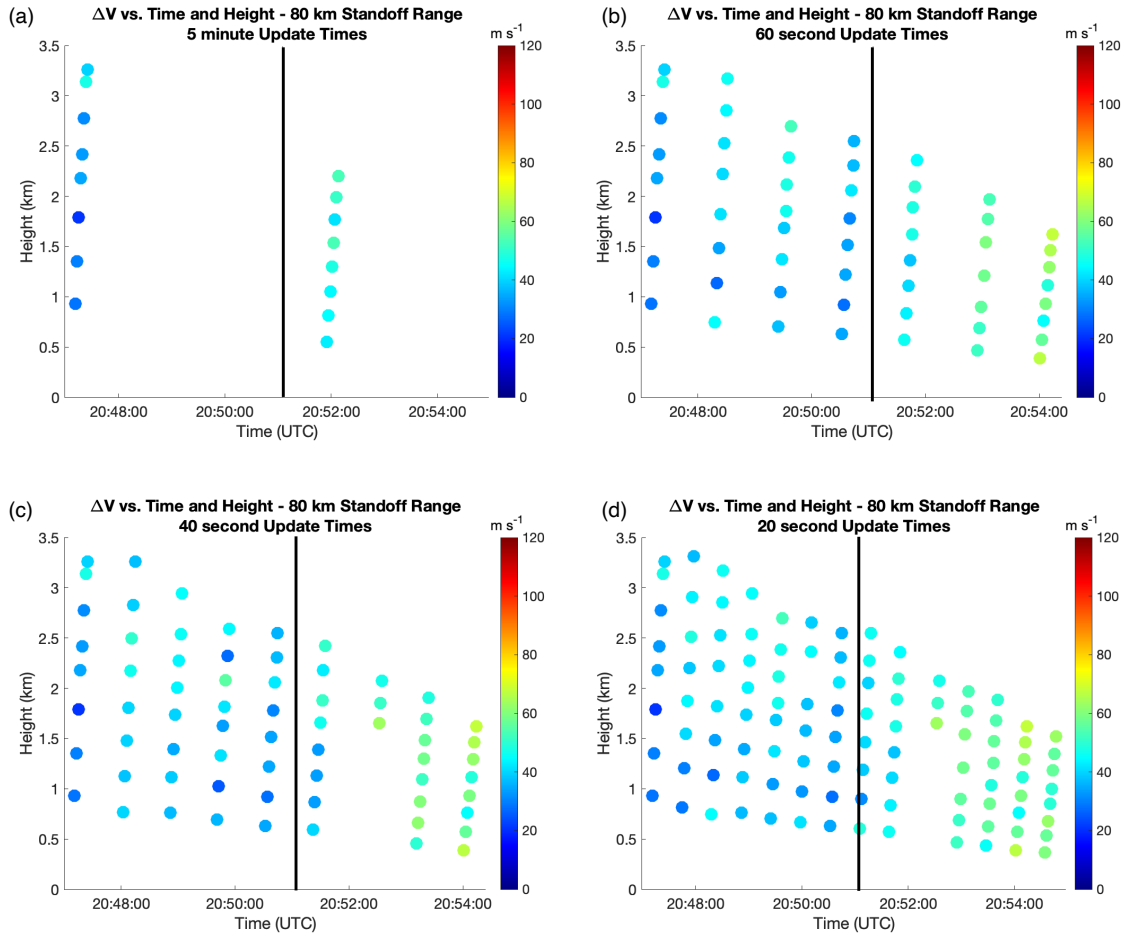
Figure 4.8: As in Figure 4.6, but here for ΔV for an emulated 80-km standoff range.

intensification. However, paired with the stronger upper-level ΔV at the beginning of the time series, this case would likely be miscategorized as tornadogenesis via a descending TVS intensification method. Higher ΔV around 50 m s^{-1} are present aloft with lower ΔV ($\leq$ 30 m s^{-1}) in the first volume scan. Subsequently, similar ΔV are present across all elevation angles by the second volume, which could lead to interpretation that the mid-level intensifying mesocyclone might have intensified in a downward manner. This, again, serves as more evidence for the need to have faster radar updates to better capture and understand the evolution of these rapidly evolving severe hazards.

The simulation of the 60-s temporal resolution system requirement is examined next (Fig. 4.8(b)). Here, the "slower" update time still provides a lot of value to a meteorological discussion. Again, limitations exist in how much can be noted about the initial brief upper-level intensification, but here TVS intensification is found again to occur in an ascending or simultaneous manner. Continued intensification is well sampled as well following the formation of this tornadic rotation. Directly compared to the 5-min update time, the data presented here are a more clear and complete depiction of the event than the WSR-88D system's 5-min update times.

The faster temporal resolution of 40-s is analyzed next (Fig. 4.8(c)). While this case does a decent job at displaying the tornadogenesis failure, there is a bit of a struggle to identify tornadogenesis as occurring close to when it did. There is a clear area of reduced ΔV around 1–1.5 km in the first volume scan shown past the vertical black line. As the only low-level ΔV close to the ΔV at the upper-levels is the 4° elevation angle, there is less clear support here for the ascending or nearly simultaneous TVS intensification method and the data are beginning to suggest the possibility of a descending TVS. However, given the coarse nature of these data and the overwhelming majority of analyses showing otherwise, it seems fair to say this is likely a temporal artifact likely from the initial selection of the first radar volume. Nonetheless, intensification is well captured near the end of the plotted time series. Though, with this and our spatial averaging methodology in mind, it seems probable that the rotation may be found to intensify simultaneously or upward on the tornado-scale but intensify downward with mesocyclone-scale rotation.

The fastest update time of 20-s is once again examined last (Fig. 4.8(d)). As with previously analyzed panel (d)s, the features of interest are well sampled here despite the significant reduction in ΔV across the time series. The slight delay in tornadogenesis occurring at such a far standoff range is evident here as all of the ΔV

crossing the tornadic-velocity threshold discussed in Section 4.1 is captured here with the first complete volume update immediately following the vertical black line. But, this still supports the ascending or nearly simultaneous TVS intensification method. Similarly, intensification still appears well at this standoff range when sampled with 20-s update times.

It is evident by looking at any of the expected PAR revisit times (20–60-s) that there is a clear need for faster radar update times if one wants to capture the evolution of rapidly changing phenomena such as tornadoes. As suggested by mobile radar studies and the data from this synthetic PAR data tool, the time scale on which tornadogenesis (via ascending or simultaneous TVS intensification) occurs is too rapid to be captured and/or confirmed with WSR-88D update times until a tornado is likely already ongoing.

4.3   PAR Scanning Mode: Focusing

This study analyzes one PAR scanning strategy: focusing. The analysis in this section will examine not only the impact of these modes on the TVS and data quality but also on the possible use to meet the next-generation system temporal resolution requirements. The results of two volumes of data at the 4° elevation angle, with each column representing one volume of the data are provided for analysis (Figs. 4.9 and 4.10).

The analysis of PPIs of Z (Fig. 4.9) shows no degradation or change that appears in the structure of the supercell. Similar results are seen in V_r (Fig. 4.10) with the evolution of the mesocyclone and TVS as smooth as if data were collected across the entire 360° azimuthal circle. Contrary to initial expectations, the rapidly updated sector is only slightly off-put from the rest of the static PPI which remains the same. Therefore, this does not change the interpretation with respect to TVS identification

or storm structure analysis. However, another possibility in plotting the results of focusing is plotting only the updated sector. The best form of visualization for this technique remains an area for further analysis.

The improved focus and temporal resolution that is capable of being provided as a result of focusing is helpful in watching the evolution of these features alongside the evolution of the mesocyclone and TVS features as well. When used in sync with each other, the reflectivity and radial velocity plots generated here complement each other well for use in an operational setting.

The power that focusing may provide for a future operational PAR network remains an open question due to the limitations of this project discussed in Section 3.2.1. With sector focused updates around an area of interest (here the area with the mesocyclone/velocity couplet), focusing would at least be able to potentially provide more useful updates on a faster temporal scale. The question remains, however, how the implementation of focusing to sample the evolution of the TVS under such rapid, focused updates could aid or hinder the warning decision process for forecasters.

Focusing may provide a balanced trade-off between the benefit and burden problem raised for operational use in Section 4.2 of this chapter. As the faster time scale for updates here only brings in data from a small, specified sector, forecasters may be less likely to become overwhelmed by an influx of data. The scanning strategy, akin to its name, provides only the most important information at that time for analysis. While outside of the primary goals for this study, there are potential pitfalls to using this method unrelated to identification of a TVS, and they are addressed below as future considerations for a focusing scanning strategy in a PAR network.

Focusing could also pair well with meeting mission goals of radar volume update times of 60 s or less while providing flexibility greater flexibility in scanning strategies
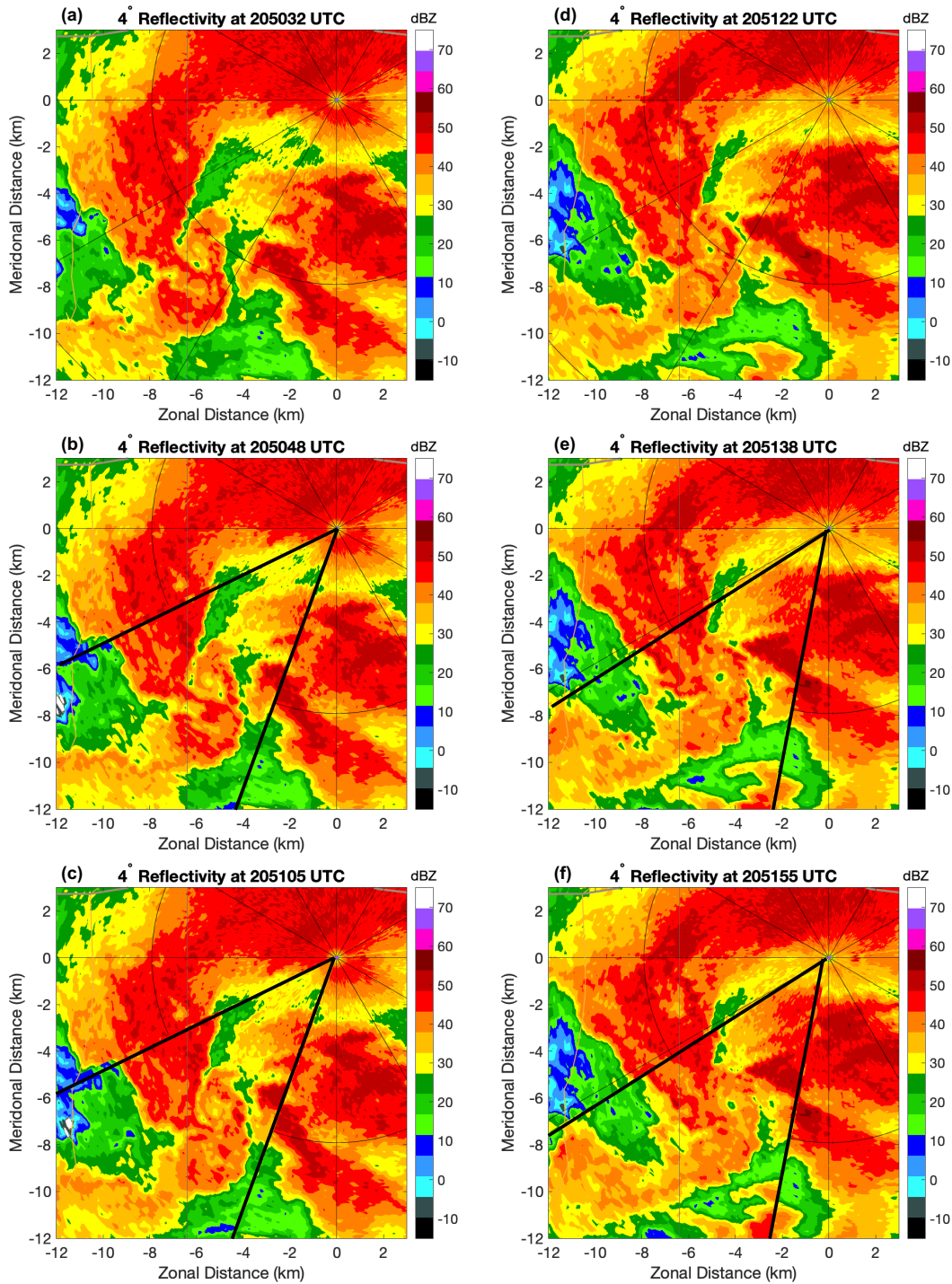
Figure 4.9: PPIs of Z at the 4° elevation angle on 24 May 2011 at (a) 2050:32 UTC, (b) 2050:48 UTC, (c) 2051:05 UTC, (d) 2051:22 UTC, (e) 2051:38 UTC, and (f) 2051:55 UTC. The figure is designed to be read by column top to bottom. Panel (a) shows a starting time with panels (b) and (c) showing the 20-s update of the 45° sector of interest outlined by black annotations. Panel (d) shows another 1-min update with panels (e) and (f) showing the same 20-s updates as (b) and (c).
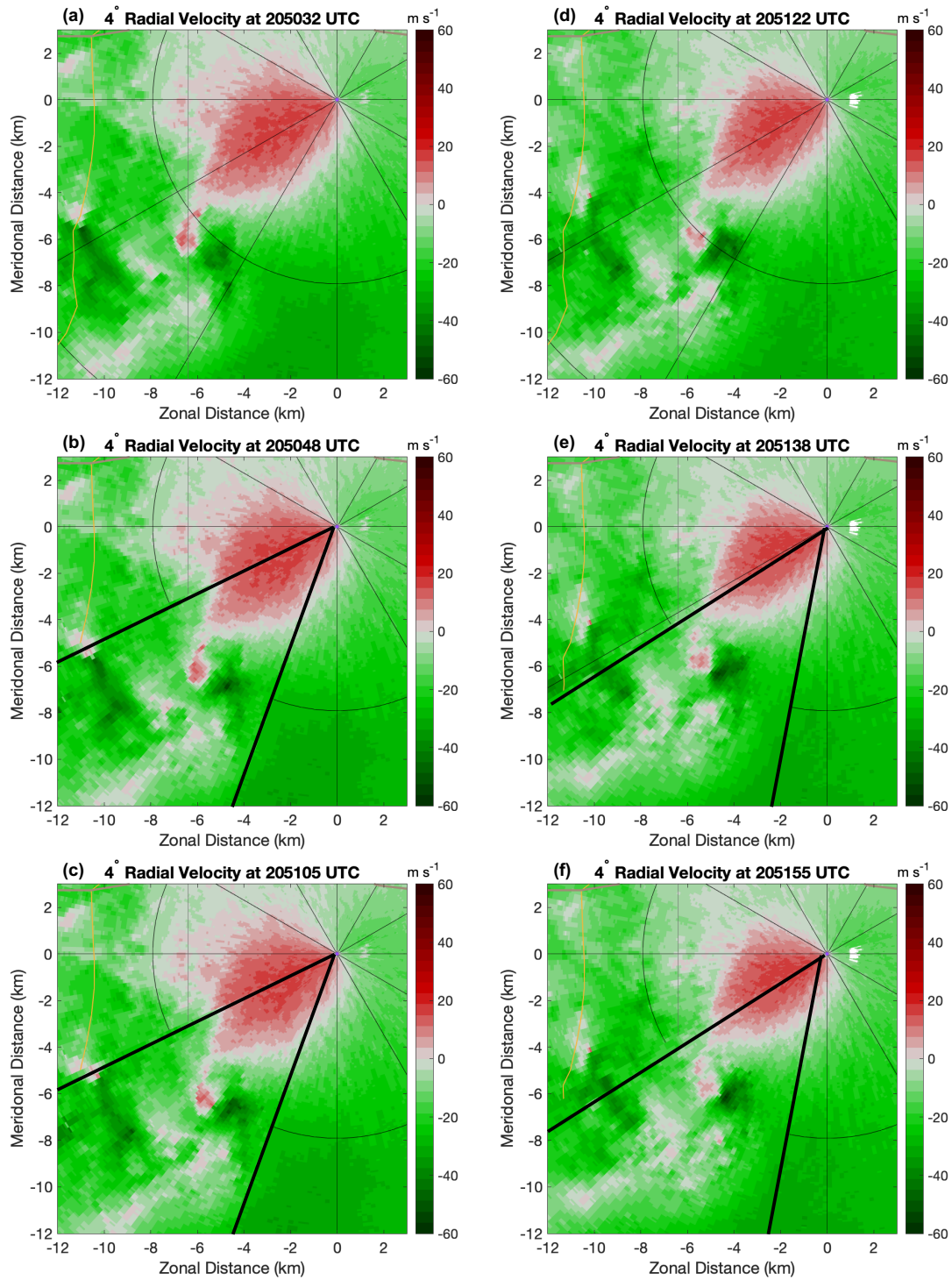
Figure 4.10: As in Figure 4.9, but here of V_r.

(similar to SAILS mode on current WSR-88D radars) to better capture the rapid evolution of severe hazards as discussed in Section 4.2. While 60-s update times were sufficient for most of the analysis, there was a clear benefit to the addition of more data from the 20-s and 40-s update times shown. With tornadogenesis occurring in such a rapid and short window (within approximately one volume scan, or about 17 s, in this case), these 20-s sector scan updates capture evolution of those tornado scale processes that are otherwise missed.

However, limitations do exist with these conclusions. While it is likely that the greatest benefit from focusing would come with targeted sampling of a particular region within a storm (e.g., mesocyclone), practical limitations must be considered. With a rotating PAR, focusing is much less likely to be used, at least in azimuth, since it would still require the radar to make a 360° azimuthal rotation to sample the smaller sector again. As the radar would still be spinning continuously across the entire azimuthal circle in this case, it begs asking what the utility would be for these scans unless you sped the radar up to recapture the sector. However, that would ultimately result in a greater amount of stress to the radar's motors and likely reduce the time needed between repairs and replacement. But, focusing could be used for data quality purposes to allocate pulses to areas of higher interest that are within the PAR's field of view. Additionally, focusing could be implemented in the vertical to avoid scanning high altitudes where no echoes are present in the absence of storms.

Chapter 5

Case II: 24 May 2016 Dodge City, KS Tornadoes

This chapter details the results and discussion related to the 24 May 2016 Dodge City, KS case. Each of the previously mentioned focus areas for this study have their own sections in this chapter. The format of analysis is similar to that of Chapter 4, but in this chapter there is separate analysis given on tornado 4 and 5, as identified in Figure 3.3 and in Wienhoff et al. (2020).

5.1   Spatial Resolution Impacts

This layout of this section once again provides primary analysis of ΔV followed by a discussion of PPIs of Z and V_r.

5.1.1   Tornado 4

Unlike the other tornadoes analyzed in this study, the entire life cycle of this tornado was captured by RaXPol. Although this was a weak tornado and dissipation is beyond the scope of this study, it does provide motivation to analyze more cases (across varied intensities) with observations of an entire tornadic life cycle to note potential benefits and signatures across its evolution.

Analysis of ΔV, from tornado 4's original data, highlights a few differences worth noting in comparison to case I (Fig. 5.1). There are three vertical lines indicating the time of tornadogenesis via a tornadic-velocity threshold of 60 m s^{-1} (2319:49 UTC),

observations (2320:26 UTC), and the time of dissipation (2321:21 UTC) from left to right. Another notable difference to the previous analysis performed with case I relates to the altitudes observed. Observations from this case were collected at much lower elevation angles than in case I, resulting in a much lower height AGL. Thus, in any discussion herein that uses the term upper-level will only be indicative of the atmospheric conditions up to 0.8 km AGL.
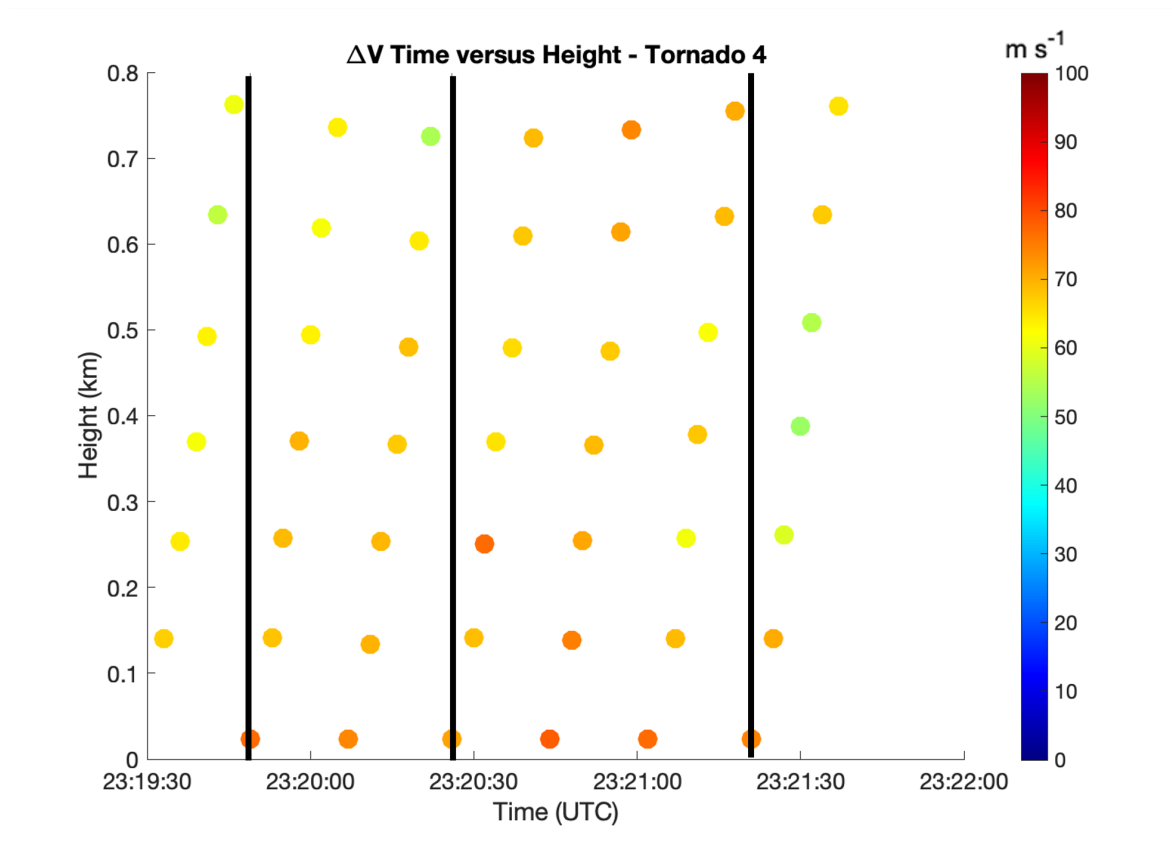
Figure 5.1: ΔV as a function of time and height on the original 24 May 2016 Dodge City, KS data set for tornado 4, as identified in Wienhoff et al. (2020). The first vertical black line represents the time at which all velocities are >60 m s^{-1} indicating tornadogenesis has occurred as in Wienhoff et al. (2020). The second vertical black line represents the time at which tornadogenesis occurred via observations. The third vertical black line indicates when the tornado dissipated.

Tornado 4 was preceded five minutes earlier by another short-lived, weak tornado. The TVS sampled remained fairly strong at the lowest elevations while remaining below the tornadic-velocity threshold of 60 m s^{-1} (not shown) at the highest elevations until 2319:49 UTC. At this time, all sampled ΔV were >60 m s^{-1}, indicating tornadogenesis had occurred utilizing the tornadic-velocity threshold. Notably, the same trend of stronger ΔV near the surface and weaker ΔV aloft (with the 6° elevation angle ($\sim$0.75 km AGL) at 2320:22 UTC sticking out as an outlier $\sim$10 m s^{-1} lower than surrounding values) continues to be observed until shortly after 2320:30 UTC, when visual observations identified tornadogenesis. Wienhoff et al. (2020) discusses that this weakness that is observed lacked support from higher aloft to generate a longer-lived vortex. Nonetheless, it is easy to identify in this case where the TVS intensification appears to occur simultaneously within the first four elevation angles sampled by 2319:49 UTC and slowly ascends as you move closer to the tornadogenesis time identified by observations.

The entire duration of tornado 4 varies slightly depending upon the method chosen for identifying tornadogenesis. It is $\sim$45–60 s based on ΔV only and $\sim$30 s from only the observational record. This serves to underscore a challenge recently discussed by Houser et al. (2022), which highlights the lack of a formal definition for a "tornadic" vortex and the variance of such a definition from study to study within the field. In addition, the rapid evolution of this tornado underscores the need for faster temporal updates to properly observe weak tornadoes, with these impacts further discussed in the following section. This would be completely unobservable with a WSR-88D radar. Considering a notional PAR with 1-min updates, this would only be sampled once. So while it could be detected at that temporal resolution, this is a case where 20-s updates are likely be useful.

Synthetic PAR data for a representative 13-km standoff range serves as the basis for the next ΔV analysis (Fig. 5.2). To create these data, spatial averaging is performed across $2°$ in azimuth and eight range gates. Using an approximate 6.5 km distance between the TVS and RaXPol provides an emulation of how a $1°$ beamwidth radar would see this tornado at a 13-km standoff range. The complete interval of standoff ranges, 13–14 km, is much smaller than with case I given the short distance between RaXPol and the TVS during this deployment.

Figure 5.2: As in Figure 5.1, but here for a 13-km emulated standoff range. Also, the vertical black lines remain in the same locations as those in the original figure for direct comparisons, even as ΔV decreases below the original thresholds listed.

Similar to the closer standoff range analyzed in case I, there was a more uniform decrease in ΔV across the observed time series by $\sim$9 m s^{-1}. Thus, an obvious degradation in ΔV is observed due to the spatial degradation needed to generate the synthetic PAR data. But, it is slightly more than the $\sim$7 m s^{-1} decrease observed in case I, with the exception of the point at 2320:22 UTC. This point seems to have had influence from some nearby higher V_r values, which provided enough influence in the averaging to result in a slightly higher ΔV in comparison to the surrounding reductions. Thus, this value likely results in a slightly lower average reduction than otherwise would be found across the time series. The 60 m s^{-1} tornadic-velocity threshold still holds fairly well for the data in the lowest elevation angles, but begins to fail at higher elevations. A reduction in this threshold by the observed average decrease fits the remaining upper-elevation data well (not shown) in still identifying tornadogenesis via ΔV at the first vertical black line.

Nonetheless, despite this decrease in ΔV, a similar qualitative trend in the formation and dissipation of this tornado remains. The ΔV prior to 2319:49 UTC (not shown) are reduced such that TVS intensification appears to occur in only an ascending manner at this standoff range beginning at that time and continuing until 2320:26 UTC. After that time, all ΔV remain >60 m s^{-1} across the depth of the column for two volume scans.

Around 2321:09–2321:16 UTC at $\sim$0.3–0.7 km AGL (or the 2–5° elevation angles), a weakening in ΔV is found. Values here begin to approach a reduced 50 m s^{-1} threshold and are below the original tornadic-velocity threshold. Thus, signs of weakening and dissipation become evident a volume scan earlier in the synthetic data than in the original data. This same area of ΔV continues to weaken after 2021:21 UTC representing the continued decay of this tornado.

The synthetic PAR data emulating a 52-km standoff range serves as the final ΔV analysis for tornado 4. This represents a 6.5 km distance between the TVS and RaXPol with spatial averaging across 8° in azimuth and eight range gates. The complete interval of standoff ranges remains small again, only 52–56 km.

Unlike the longer standoff range (i.e., 80-km) observed in case I where there is a difference in the observed reduction in ΔV prior to and after tornadogenesis, that is not found here. Instead, there is an average reduction by ~13 m s^{-1}, only about 4 m s^{-1} more than the closer standoff range. As a result of this observation, it seems that the impact of spatial averaging lessens for weaker tornadoes across all standoff ranges (also seen at 26-km, not shown) in comparison to stronger tornadoes. A reduction in the overall range of values is also seen, making it more difficult to see trends in tornado intensity. Recalling the case context described in Section 4.1, and considering it in comparison to that of a weaker tornado, this makes sense. The overall V_r field for this tornado was weaker, alongside the weaker velocities that are found in a couplet, which reduces the chance for significantly decreasing more extreme values as found in case I.

These results (Fig. 5.3) do highlight an area of challenge for longer-range observations with respect to weak tornadoes. In this case, the ΔV across all sampled elevations are within an ~18 m s^{-1} range. But from a purely visual look at the given figure, it is easy to see how visually analyzing the output from the simple ΔV calculation may lead to difficulties in properly analyzing the rotational intensity present. All ΔV shown from 2319:49 UTC onward are still >50 m s^{-1}, except for the 6° elevation angle. An increase in the ΔV in the next volume occurs at all levels by ~2–10 m s^{-1}, with an average of 4 m s^{-1}. Similar slight weakening (~2–5 m s^{-1}) occurs in the following volume coincident with the second vertical black line at 2320:22. This lost strength is regained in the following volume and sustained across the remainder of the time series.
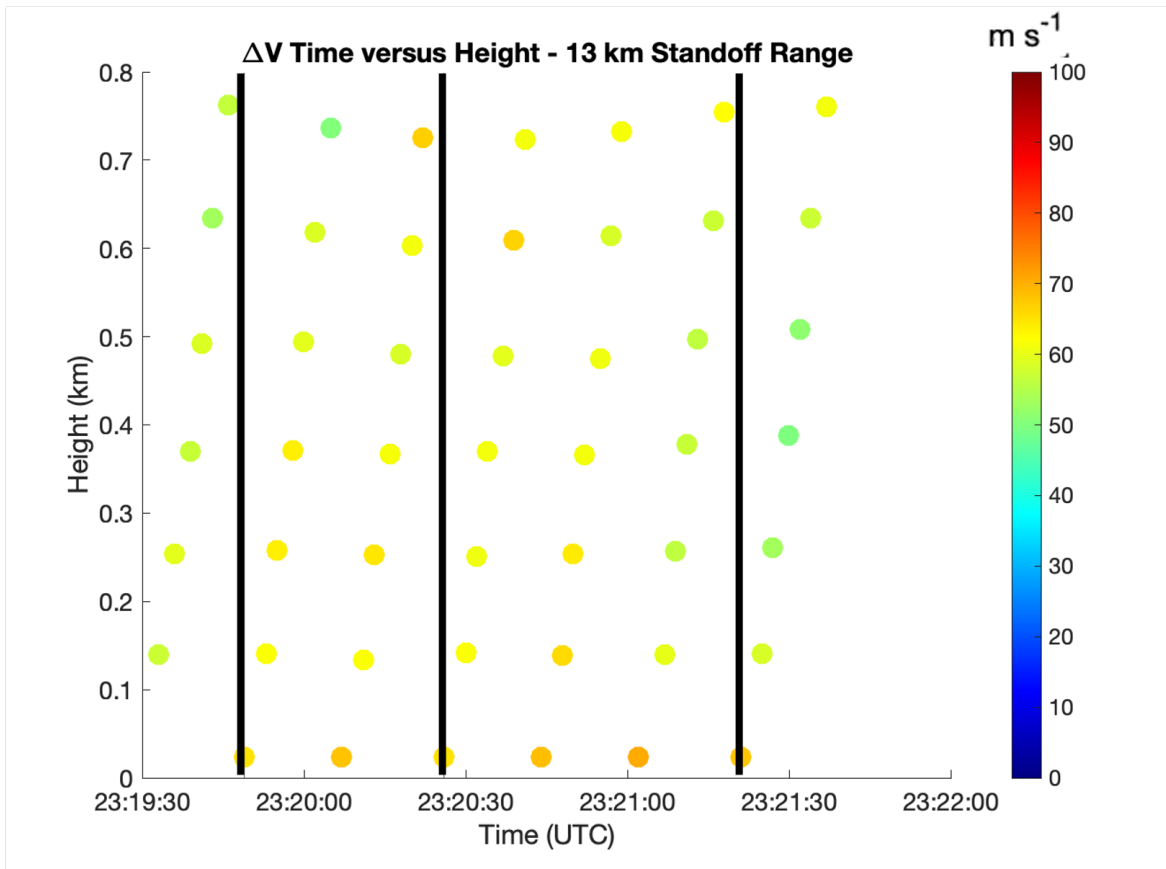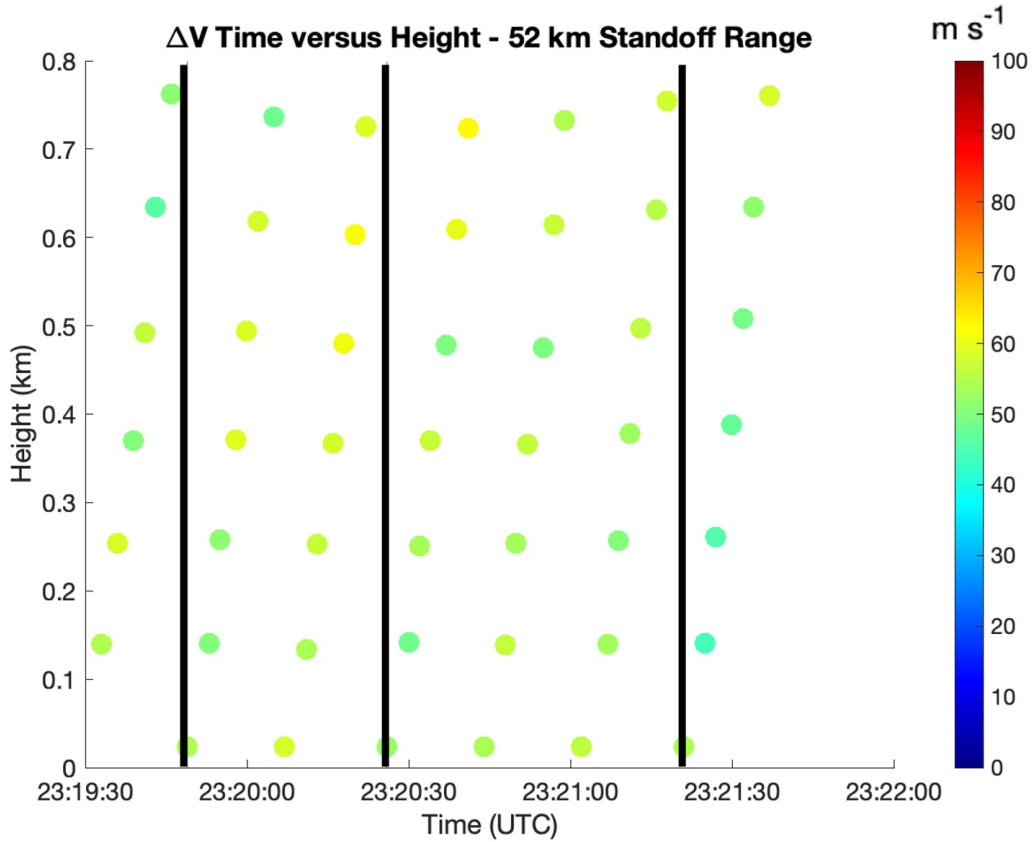
Figure 5.3: As in Figure 5.1, but here for a 52-km emulated standoff range. The vertical black lines remain in their original locations as detailed in the caption for Figure 5.2.

The same weakening found at the 13-km standoff range remains (by about 10 m s^{-1}) is exhibited in the final volume shown from ∼0.1–0.7 km AGL, with some weakening evident in this same layer a volume earlier but only by 2–5 m s^{-1}.

To provide a better idea of the output from the synthetic PAR data tool as well as the radar images a forecaster would actually see, several PPIs at different elevation angles are provided for both Z and V$_r$ (Figs. 5.4 and 5.5). Within each column, there are three elevation angles providing the PPIs for the original data alongside the synthetic data for the two standoff ranges used in this case, 13-km and 52-km.
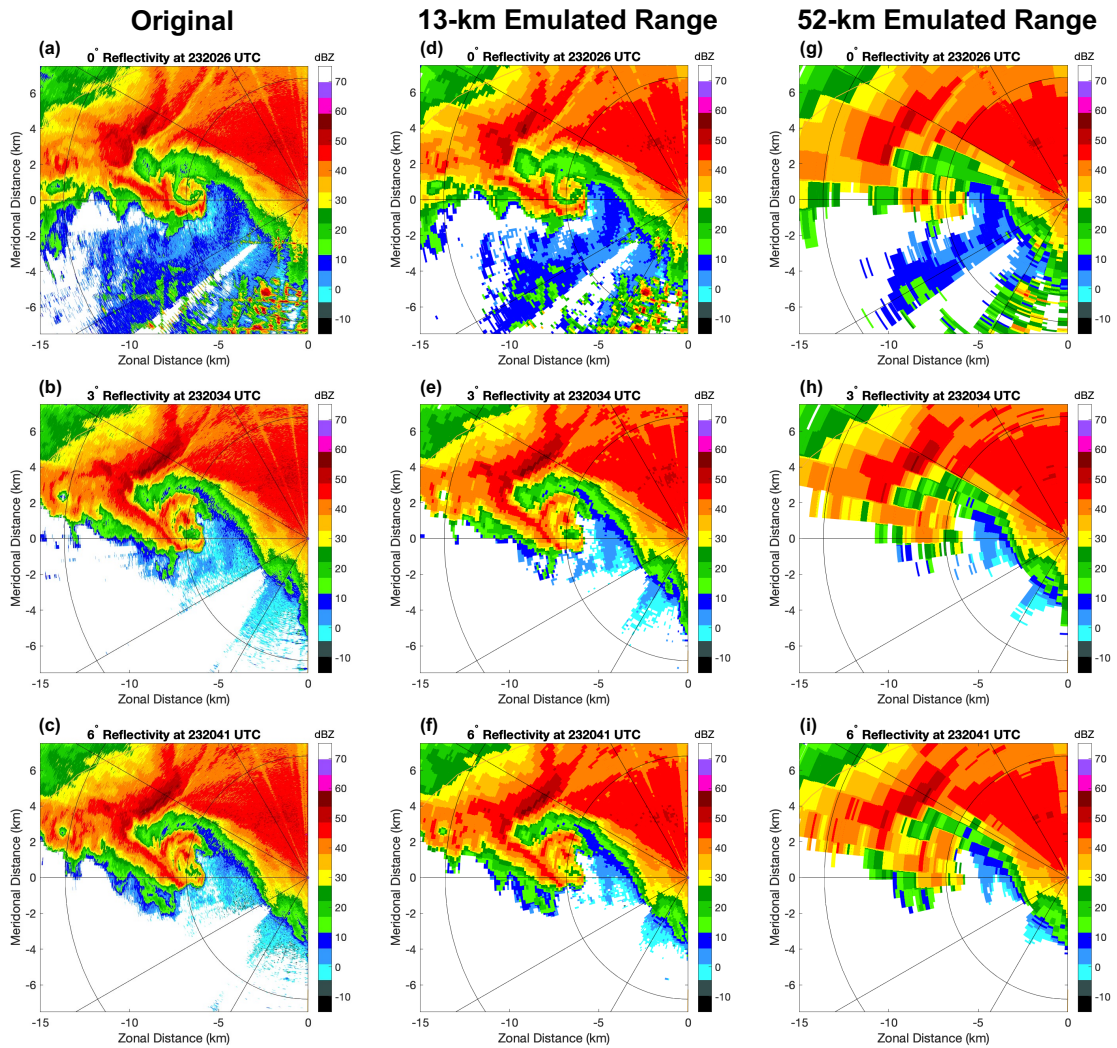
Figure 5.4: PPIs of Z at the 0°, 3°, and 6° elevation angles on 24 May 2016 at 2320:26 UTC, 2320:34 UTC, and 2320:41 UTC in each row, respectively. Three labeled columns separate the original RaXPol data (left), data at a 13-km emulated standoff range (middle), and data at an 52-km emulated standoff range (right) for each of the elevation angles.
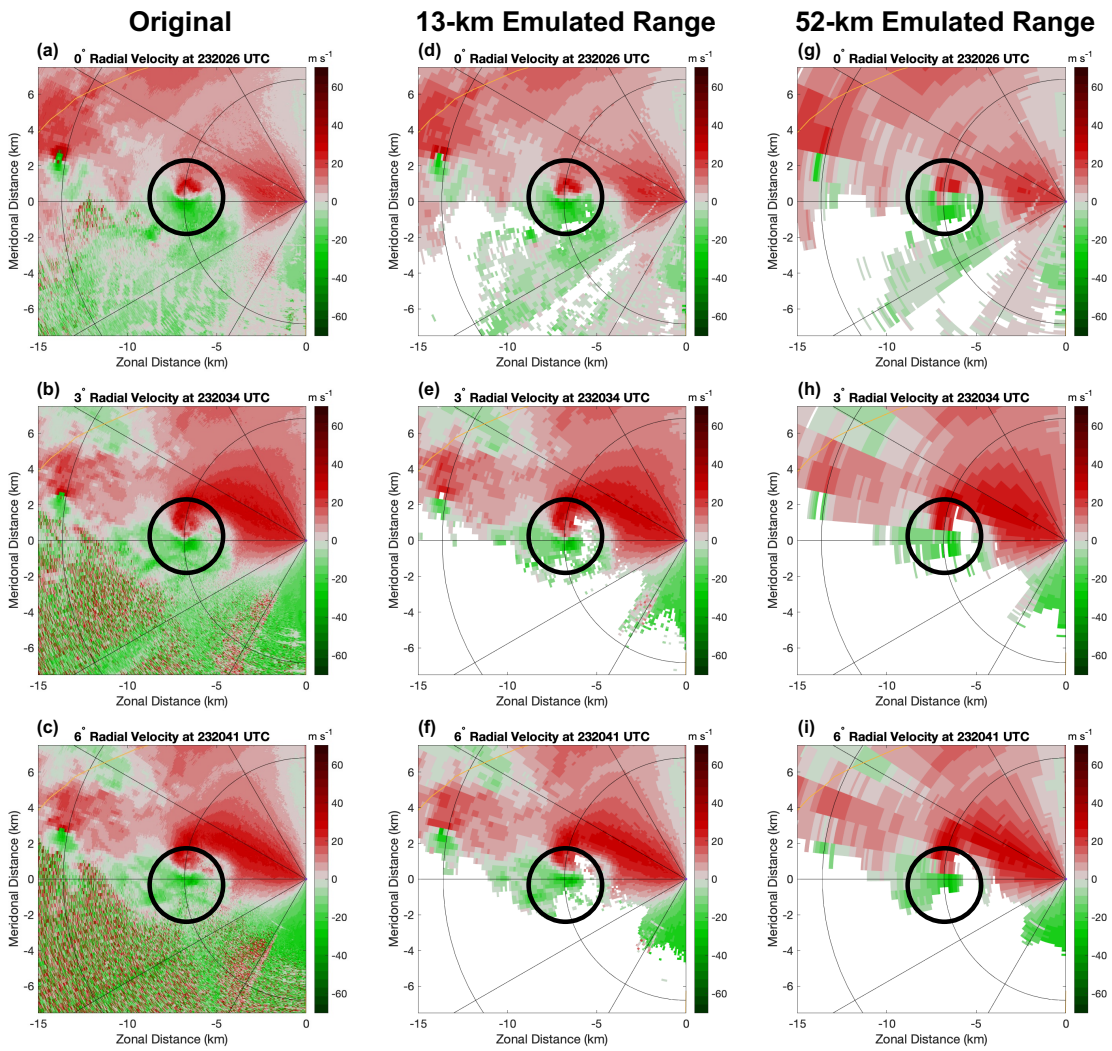
Figure 5.5: As in Figure 5.4, but here PPIs of V$_r$. The black circle denotes the TVS of interest.

The PPIs of Z (Fig. 5.4) again show the impacts of spatial averaging become more obvious at longer standoff ranges. In comparison to the original data, the 13-km standoff range data look relatively similar to smoothed radar data. All of the important features, notably the hook echo containing the tornado, remain prominent and visible for analysis. There are minimal impacts to the remainder of the data shown there. However, in the 52-km data, the structure of the storm and its features (i.e., hook echo) are not as easily discernible. The general structure of the supercell remains intact, and while not as clear as the 13-km data, one may be able to still identify where a hook echo feature would be on the data.

The PPIs of V_r (Fig. 5.5) display similar patterns for recognition. To familiarize the reader, tornado 4 was located within the TVS nearest the center of the figure (i.e., closest to RaXPol). The TVS farther away from the radar is the ongoing tornado 1, and does have some velocity aliasing. Once again, the closet standoff range of 13-km still reflects data that merely looks to smoothed with a well identifiable TVS still present. Notably, however, in contrast to the more difficult to discern hook echo found in Z in the 52-km standoff range data, the TVS nearest the radar is still clear to identify.

5.1.2 Tornado 5

In comparison to the previous tornadoes already introduced and discussed in this study, tornado 5 represents a tornado in more of the middle of the EF scale. As a stronger tornado in this supercell, it was preceded by two previously weak tornadoes, both of which were from the same mesocyclone.

Analysis of the original data holds a similar pattern as previous cases (Fig. 5.6). Similar to tornado 4, there are two vertical black lines indicating the time of tornado-genesis via a tornadic-velocity threshold of 60 m s^{-1} (2321:57 UTC) and observations
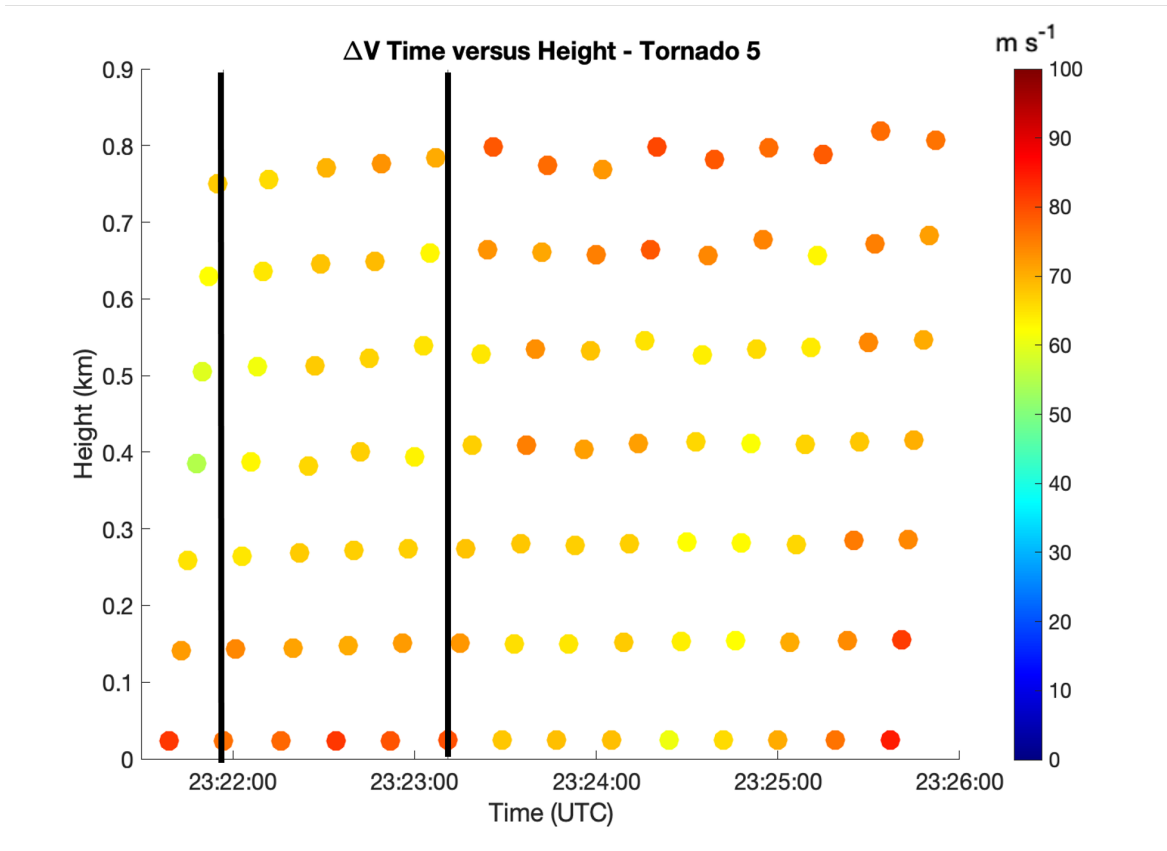
71

Figure 5.6: ΔV as a function of time and height on the original 24 May 2016 Dodge City, KS data set for tornado 5, as identified in Wienhoff et al. (2020). The first vertical black line represents the time at which all velocities are >60 m s^{-1} indicating tornadogenesis has occurred as in Wienhoff et al. (2020). The second vertical black line represents the time at which tornadogenesis occurred via observations.

(2323:11 UTC). The same range of lower elevation angles and heights AGL are found here as with tornado 4.

Tornado 5 was preceded by tornado 4, and the associated ΔV had already intensified rapidly at the lowest elevation angles (0–2° or ∼0-0.2 km AGL) following the dissipation of tornado 4. Compared to the ΔV seen with tornado 4's original data, these ΔV are indicative of a stronger and more intense rotation ongoing.

At the first vertical black line (2321:57 UTC), all of the plotted ΔV passed a tornadic-velocity threshold of 60 m s^{-1} as defined by Wienhoff et al. (2020). Notably,

this study stated that despite the presence of these relatively strong ΔV values, the tornado was not ongoing at this time. Once again, this further exemplifies the subjective problems discussed in Houser et al. (2022) related to the challenge in identifying tornadogenesis via a tornadic-velocity threshold, pseudo-vorticity, or similar metric.

Nonetheless, this area of relatively intense rotation is confined near the ground at first and slowly builds upwards to 0.8 km AGL until there are similar ΔV found across the column of data by 2322:16 UTC. These ΔV remain steady as with in time moving towards the second vertical black line (2323:11 UTC). After this point, there is some weakening found in the lower elevations (below 2° or 2 km AGL), but elevations above that point have continued to maintain their intensity. This trend persists and slowly builds upwards into the 3–5° elevation angles between 2324:24 and 2325 UTC volumetric updates. However, as this weakening moves upwards, the lower levels begin to rapidly reintensify. By 2325:19 UTC volume update, the entire column has rapidly reintensified and finally returns to $\Delta V > 70$ m s^{-1}. The time period after this continued to see rapid intensification of the tornado.

Synthetic PAR data emulating a 15-km standoff range serves as the basis for the next ΔV analysis (Fig. 5.7). The data were created by performing spatial averaging across 2° in azimuth and eight range gates. Here, using an approximate 7.5 km distance between RaXPol and the TVS (as the distance between RaXPol and the TVS was closer to this distance longer in the selected time range), emulating how a 1° beamwidth radar would see this tornado at a 15-km standoff range. The full interval of standoff ranges represented remains small at 13–15 km.

The decrease in ΔV is relatively uniform across the time series. Some exceptions exist where with weakening period found after 2324 UTC with decreases closer to 12 m s^{-1}, but there is not a large disparity between before and after tornadogenesis as found
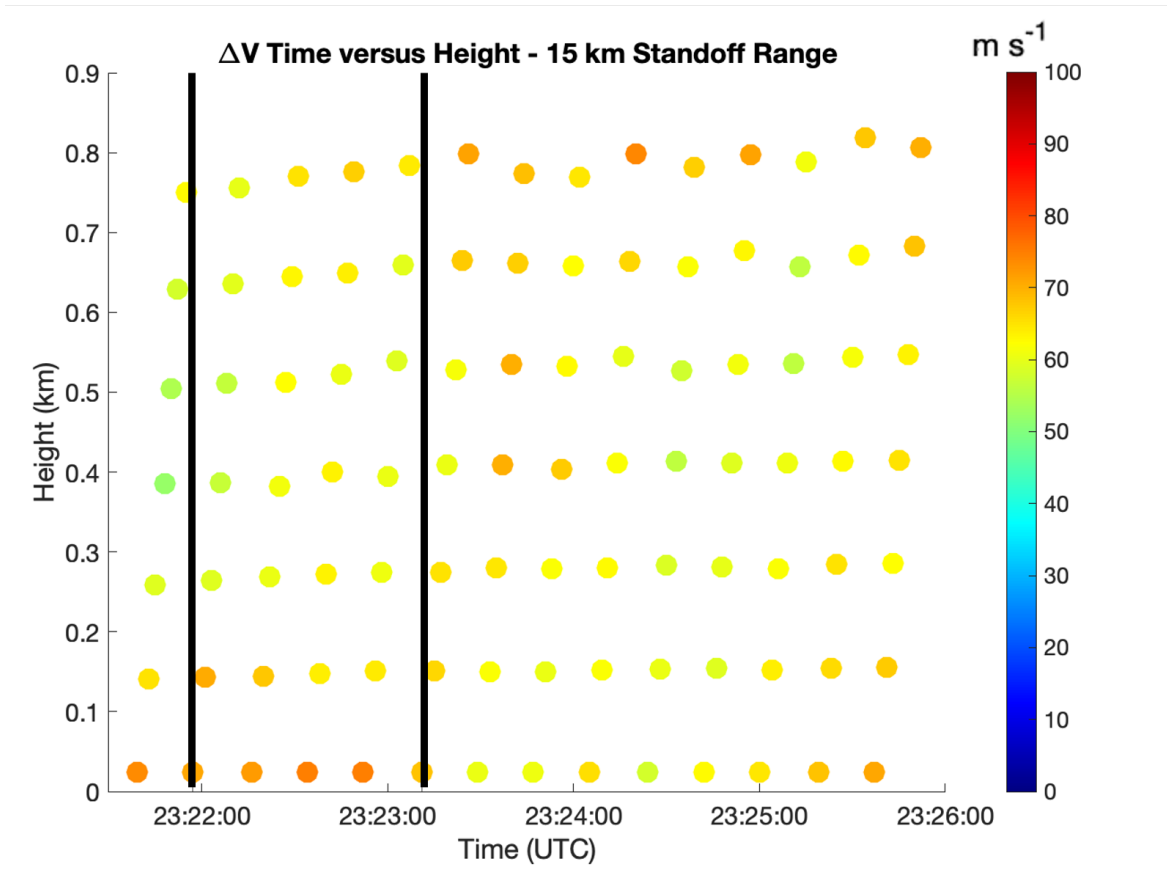
Figure 5.7: As in Figure 5.6, but here for a 15-km emulated standoff range. Also, the vertical black lines remain in the same locations as those in the original figure for direct comparisons, even as ΔV decrease below the original thresholds listed.

in case I. Nonetheless, the effects of spatial degradation are evident with these reduced values. However, evidence remains in support of a TVS ascending with time after 2321:57 UTC, once again consistent with previous mobile radar studies and findings in this study.

The weakening of the lowest elevation angle's ΔV is also well captured in the synthetic data. Pockets of weaker ΔV building upward from the surface to $\sim$0.7 km AGL are also still captured in these data. The rapid re-intensification that occurs at the end of the time series in Figure 5.6 is still seen in these synthetic data. While there is evidence of intensification (by $\sim$20–30 m s^{-1}), it is slightly weaker than before and

there are more areas around 0.3–0.6 km AGL which are still noticeably weaker than those ΔV above and below.

The synthetic PAR data emulating a 60-km standoff range serves as the basis for the final ΔV analysis (Fig. 5.8). These data use the 7.5 km distance between RaXPol and the TVS as well as averaging across 8° in azimuth and eight range gates.
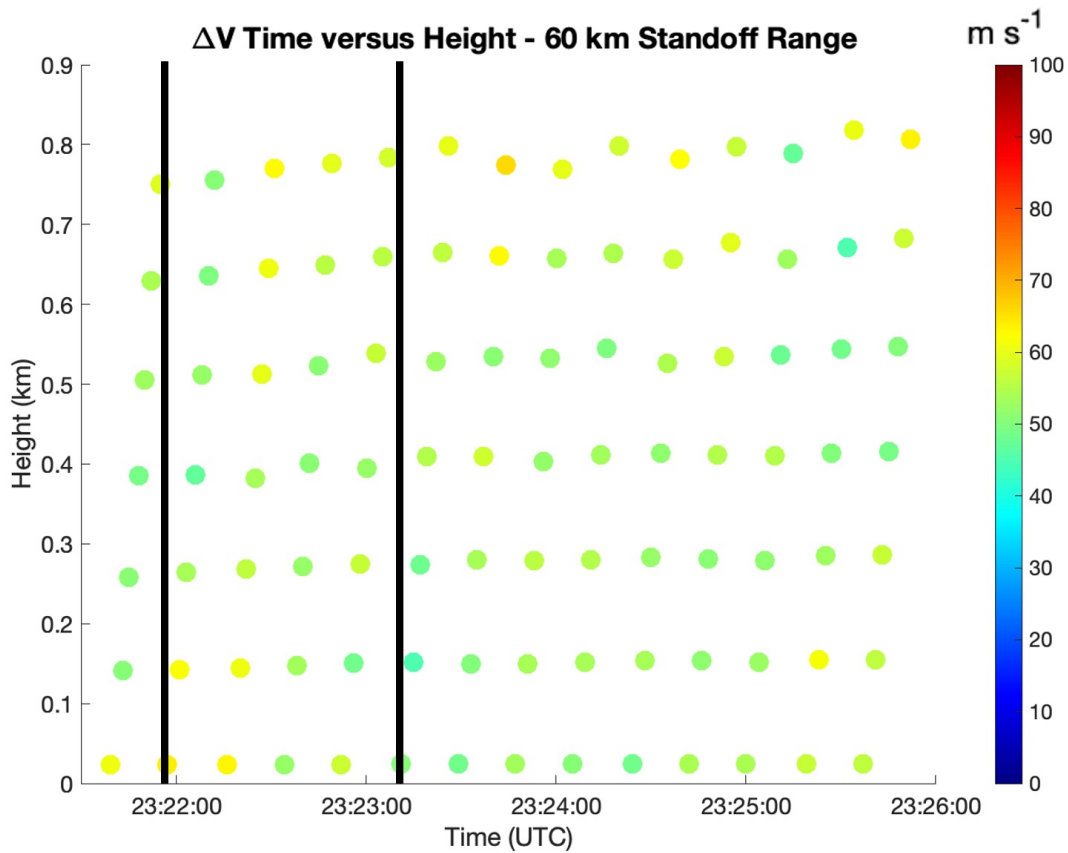
Figure 5.8: As in Figure 5.6, but here for a 60-km emulated standoff range. The vertical black lines remain in their original locations as detailed in the caption for Figure 5.7.

Similar to tornado 4, there is not a discrepancy at this longer range between times before and after tornadogenesis. It is recognized that this may be a result of the limitation in collecting much data to use in the "before" tornadogenesis time frame.

Instead, visually, there is a much more significant decrease in the ΔV, which is an average $\sim$18 m s^{-1} decrease across the time series.

Despite this significant degradation in ΔV, however, a generally similar qualitative trend of intensification remains visible shortly after the first vertical black line. As with earlier longer standoff ranges, a slight delay (again by one volume scan) in detecting this TVS intensification through ΔV is found, in comparison to the original data. At this longer standoff range, however, the rate of this intensification is even shorter and weaker with ΔV stabilizing around 2322:24 UTC through the remainder of the time series. This means that these data are unable to resolve the weakening moving from near surface up through 0.6 km AGL (2324–2325 UTC) as found in the previous two figures for this case. There is, however, some intensification, albeit with the same pockets of weaker ΔV mentioned with the 15-km standoff range, evident on the final two volumes of data plotted. The intensification is most evident at the 0–2° and 5–6° elevation angles.

As with tornado 4, another set of PPIs at different elevation angles for Z and V_r are provided (Figs. 5.9 and 5.10). The same format holds, except now the standoff ranges shown are 15-km and 60-km.

The PPIs of Z (Fig. 5.9) reveal the same relationship as previously shown between the closer and farther away standoff ranges. The 15-km standoff range data still primarily has a smoothed appearance, and the area of interest (hook echo) remains visible across all elevation angles. While the hook echo is certainly less distinct in shape at the 0° elevation angle when looking at the 60-km standoff range data, it does become more difficult to observe at the 3° and 6° elevation angles, but a trained eye may still detect some of the structure and identify the hook echo. A practical consideration, and among the future work for this project, is what the lowest elevation angle would
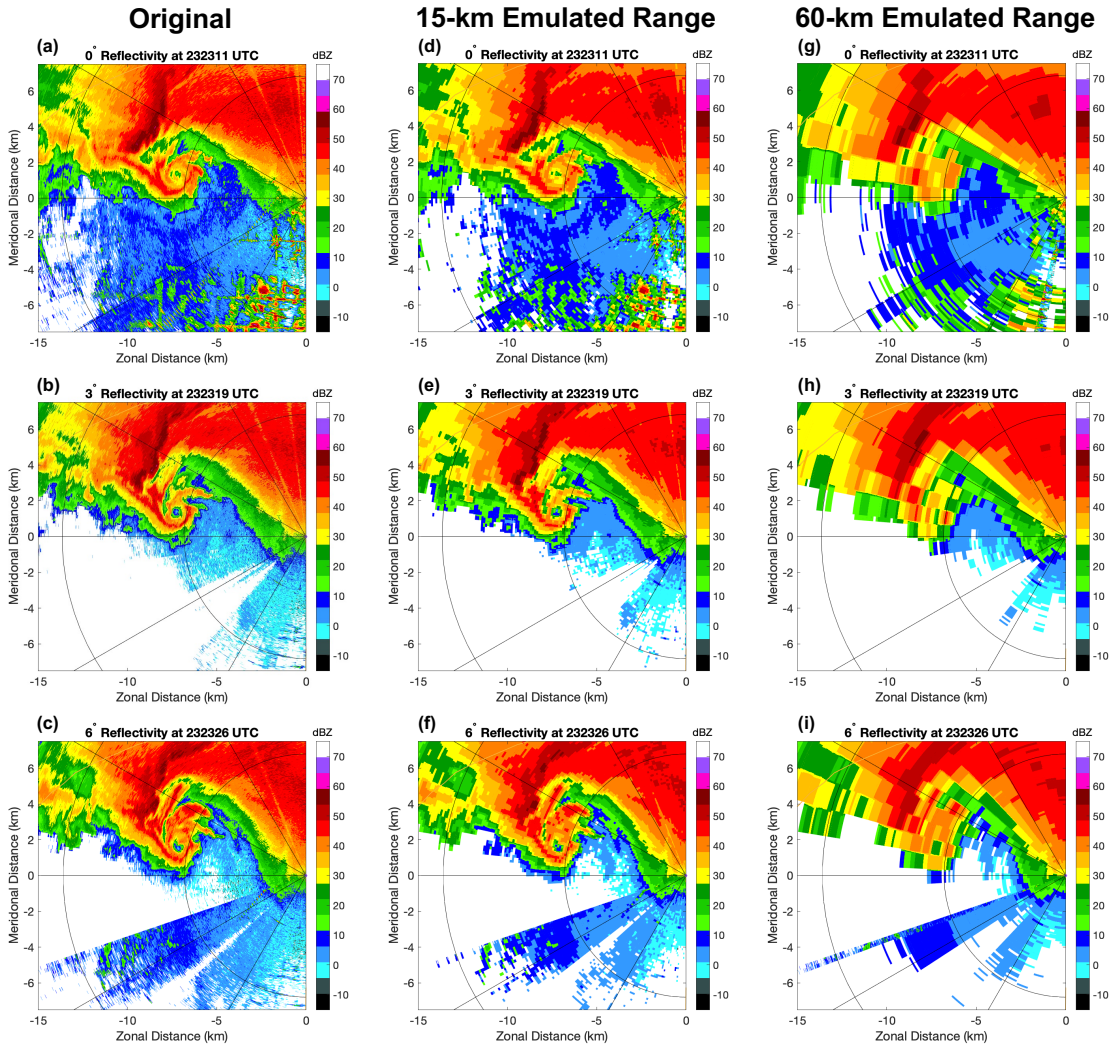
Figure 5.9: PPIs of Z at the 0°, 3°, and 6° elevation angles on 24 May 2016 at 2323:11 UTC, 2323:19 UTC, and 2323:26 UTC in each row, respectively. Three labeled columns separate the original RaXPol data (left), data at a 15-km emulated standoff range (middle), and data at an 60-km emulated standoff range (right) for each of the elevation angles.
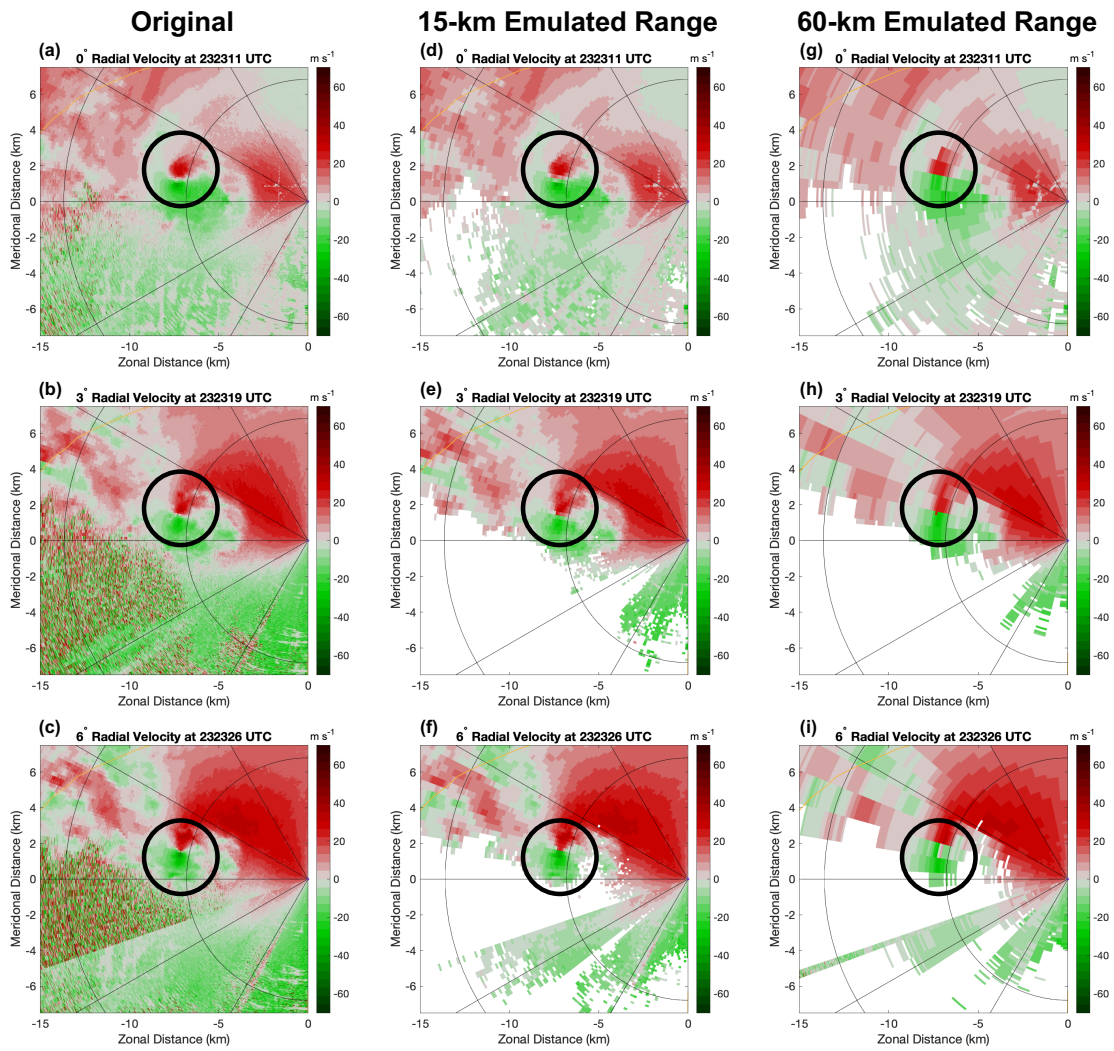
Figure 5.10: As in Figure 5.9, but here PPIs of V_r. The black circle denotes the TVS of interest.

actually be at that point in range. Therefore, it is important to consider that it is more likely that a PPI which looks like the 3° or 6° elevation angle would be the lowest elevation for analysis.

The PPIs of V_r (Fig. 5.10) show the same basic patterns as found in tornado 4's PPIs (Fig. 5.5). The velocity couplet remains the closer one, and across both the 15-km and 60-km synthetic data, a clear couplet can still be identified, providing further support for the utility of long range observations with a future operational PAR. Given the promising results here for the identification of a possible TVS via these PPIs, a similar study looking at the polarimetric variables could provide insight on the utility of long range observations with polarimetric variables associated with a TDS, such as ρ_{hv} and Z_{DR}.

5.2 Temporal Resolution Impacts

Challenges inherent to the evolution of this cyclic supercell limit the extent of some discussion provided in this section. However, this aspect remains important to the study, and a complete analysis is provided on the data available for analysis with respect to these inherent limitations.

5.2.1 Tornado 4

For this specific tornado, only 2 min of data were able to be collected. This was a common trend across the weaker tornadoes found in the data set as (1) their duration was inherently shorter and (2) the cyclic behavior of the parent supercell producing these weaker tornadoes in rather quick succession ahead of the stronger tornadoes found in the data. As this tornado was both preceded and succeeded by other tornadoes, the data available to sample specifically related to tornado 4 for the purposes of this study

was reduced. The trend existed across all of the short-lived tornadoes present in the data as an inherent limitation present from the actual storm dynamics. As a result, analysis of a 5-min update time is impossible in this case. While analysis was completed at 20-s, 40-s, and 60-s volumetric updates, the results were increasingly limited as the update time increased. The results to be gained from these plots are minimal, so they are not included in this thesis. However, a brief discussion of overall results from them is provided below.

Even at its longest possible duration of 1 min, this tornado would likely have been missed by a WSR-88D radar. If a future radar operated with 60-s volumetric updates, its utility would be greater in comparison to current radars, but it would still remain limited for short-lived tornadoes. While one volume of data might indicate a tornado is on the ground at these update times, it would fail to capture the evolution in either intensification and/or dissipation without update times of 20–40-s.

The need for faster volumetric updates remains equally important whenever considering the temporal updates on the spatially degraded data. In this case, as one might expect, the increase in volumetric updates available at higher temporal resolutions would be most helpful in attempting to detect these weaker tornadoes at long ranges.

Nonetheless, this case further supports the need for rapid temporal updates to be a priority to identify tornadogenesis across the range of intensities found with tornadoes. Without a rapid-scan system like RaXPol, this tornado would likely have only been verifiable via observations and not through Doppler radar analysis. These same results, although not presented here, are found across the remaining weak tornadoes in the data set.

5.2.2   Tornado 5

Similar to tornado 4, ∼4 min of data are available for analysis, so there is a lack of data in this particular set to emulate a 5-min volumetric update time. Therefore, analysis will instead be performed on the possible capabilities for a future PAR: 20-s, 40-s, and 60-s.

The impacts of temporal downsampling are first applied to the original data set (Fig. 5.11). As in Section 4.2, the analysis presented here will be qualitative with quantitative analysis provided in Section 5.1.2 of this chapter.

To analyze the minimum system requirement of a future operational PAR, a comparison to 60-s updates is presented (Fig. 5.11(a)). There is an evident lack of data in comparison to the other two panels. However, there are more volumes of data available than otherwise could be seen with 5-min update times (i.e., two volumes). In this case, the 60-s update actually well at capturing the TVS intensification across all sampled volumes. Additionally, the growth of the TVS is consistent with mobile radar studies by beginning near the surface and appearing across the entire column in the next update. Notably, the 60-s updates do miss the period of weakening otherwise seen near the end of the plotted time series.

To examine the PAR capabilities of updates faster than the system requirements, a 40-s temporal resolution is emulated (Fig. 5.11(b)). Only one more volume of data are available than with the 60-s updates in panel (a), which is not a vast improvement. More important to consider here is the impact this temporal resolution has on the data that are sampled by the radar. In this case, the radar once again captures intensification beginning near the surface and moving upward across the entire column in one volume update. However, in the next two volume updates, weakening is found near the surface and further weakening from near the surface to ∼0.55 km AGL, respectively. The final
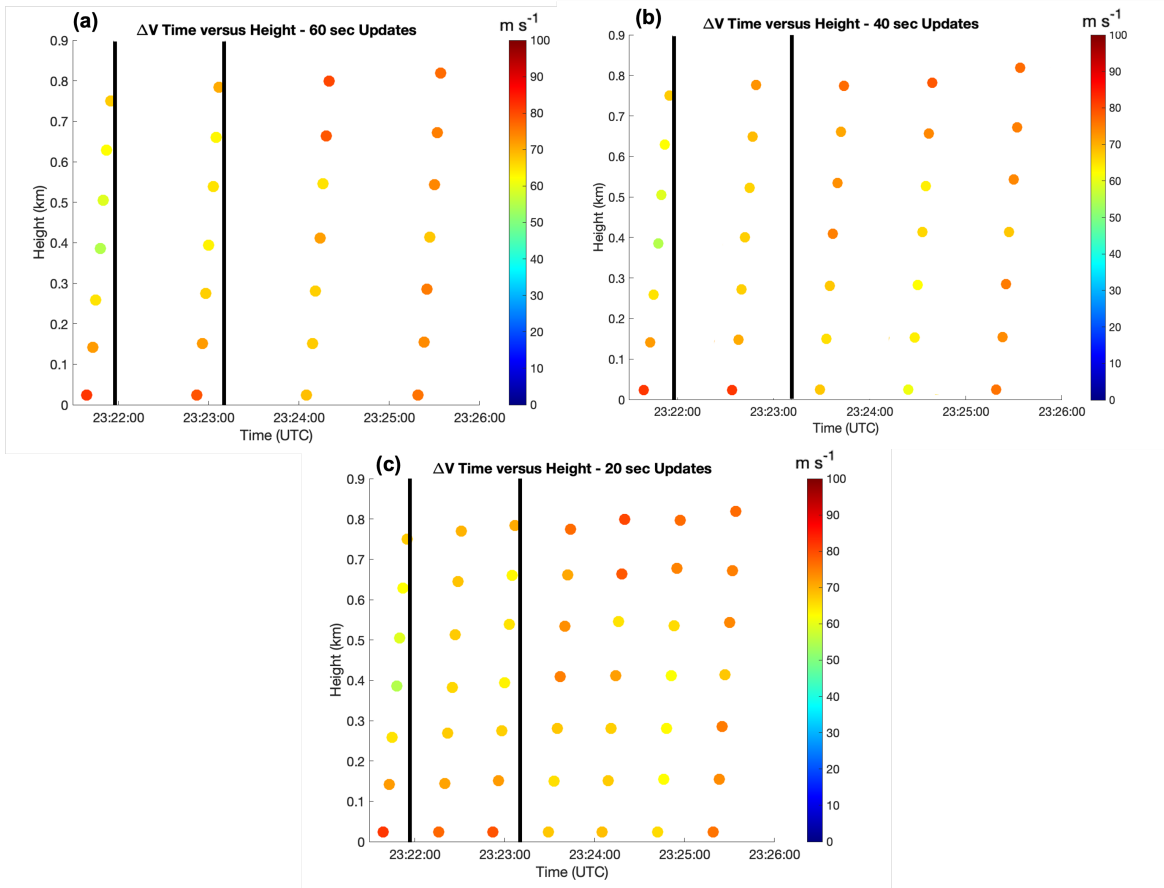
Figure 5.11: ΔV as a function of time and height on the original 24 May 2016 Dodge City, KS data set, using tornado 5 as identified in Wienhoff et al. (2020). The first vertical black line represents the time at which all velocities are >60 m s^{-1} indicating tornadogenesis has occurred. The second vertical black line represents the time at which tornadogenesis occurred via observations. Data are temporally downsampled to provide volumetric updates on temporal scales of every (a) 60-s, (b) 40-s, and (c) 20-s.

volume update once again shows the intensification of ΔV across the entire column. Though, this time, it becomes more likely to appear (though difficult to completely conclude) that the intensification of the TVS built downwards from 0.7 km AGL. This would be in contrast to previous mobile radar studies and results seen in the other results in this study with respect to the original data.

The capabilities of an even faster temporal resolution is provided through an emulated 20-s temporal resolution (Fig. 5.11(c)). The most data (i.e., full volumetric

updates) are available at this temporal resolution. Once again, the beginning of the time series reflects TVS intensification occurring in an ascending manner. The weakening present between 2324–2325 UTC is observed at this resolution. Once again, as with panel (b), there is some difficulty in identifying the TVS intensification method noted between the final two volumes shown. However, it would seem to imply that the TVS likely descended just as seen with the 40-s resolution.

Data from the 52-km standoff range are are also examined at the 60-s, and 40-s, and 20-s temporal resolutions (Fig. 5.12). As the number of volumes and their location across the time series remain the same as the analysis on the original data, focus is on similarities and differences found between the two.

The minimum system requirement temporal resolution of 60-s is simulated first (Fig. 5.12(a)). In this case, weakening across the first three volume at the 0° elevation angle is evident, with restrengthening occurring in the final volume. Otherwise, across much of the first three volumes shown, visually, there is little change and the entire field has a homogeneous appearance. There is not any indication of a weakening period between 2324–2325 UTC as seen in the original data. At this resolution, it is difficult to ascertain the TVS intensification method with these volumes, though it is acknowledged that this may be an artifact resulting from the selection of the initial volume time.

A 40-s temporal resolution again provides updates faster than the system requirements (Fig. 5.12(b)). Much of this panel carries similar visual characteristics to panel (a). There is a decrease of the ΔV at the 0° elevation angle across the first four volumes while there is an increase at the 5° and 6° elevation angles across the first three volumes before eventual weakening in the final two. The remainder of the elevation angles carry similar values, and there is once again a lack of indication there is any
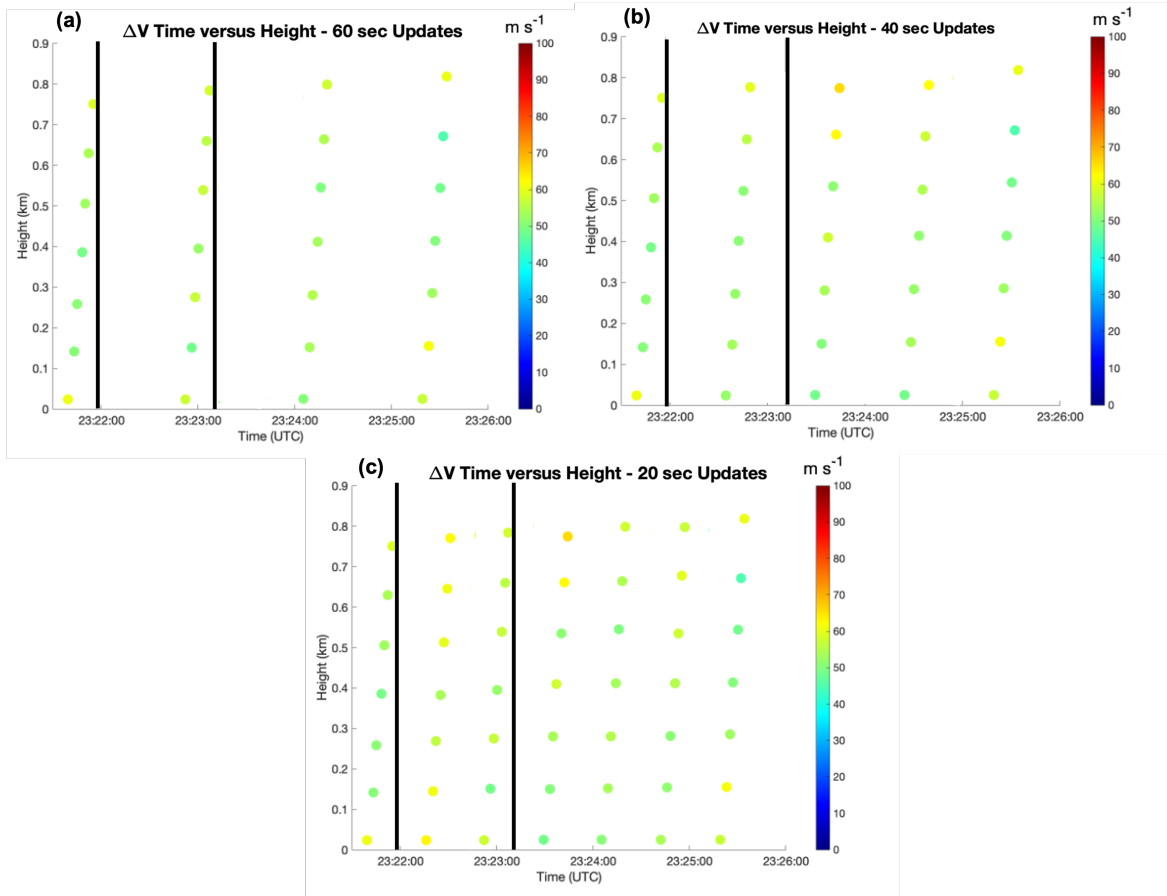
Figure 5.12: As in Figure 5.11, but here for ΔV for an emulated 60-km standoff range.

weakening process occurring between 2324–2325 UTC. Within the last volume, there appears to be support for intensification beginning to take on an ascending manner, though this is limited by the lack of an additional volume in the time series to confirm this.

A 20-s temporal resolution provides an emulated PAR scan at the highest resolution tested (Fig. 5.12(c)). In contrast to the other two resolutions used at this standoff range, the 0° elevation angle appears to intensify across the first two volume scans before weakening and stabilizing until the final two volumes. Interestingly, the intensification across the entire column does not appear until 2322:16 UTC, after the first

84

vertical black line. This would indicate a slight delay in the identification of tornadogenesis occurring via the tornadic-velocity threshold, but would still support an ascending TVS intensification method. Beyond this time, there is once again little visual support of any weakening period beyond that seen at the 0° elevation angle. At the final volume, again with a slight delay in comparison to the original data, re-intensification begins to occur from the surface building upward. This slight delay in observing tornadogenesis was also found at long standoff ranges with the data presented in Chapter 4.

Results from the 15-km standoff range are consistent with mobile radar observations of ascending/simultaneous TVS intensification. One exception to this is with the 40-s temporal resolution, where similar to previous discussion on this tornado, there appears to be support for descending TVS intensification near the end of the time series while ascending TVS intensification is present prior to 2324 UTC. However, as these results are largely similar to expectations and previous figures shown here, they are not shown here.

5.3   PAR Scanning Mode: Focusing

This section once again provides an analysis on the tested PAR scanning mode of focusing and its potential use to aid in the desired temporal resolution of a future operational PAR network. As Sections 3.2.1 and 4.3 have highlighted the limitations of this analysis as well as discussed some of the potential operational uses, this section will be kept brief.

5.3.1 Tornado 4

Results from this study are limited in understanding and analyzing the utility of focusing in scenarios like tornado 4. The reasoning for this is two-fold: (1) the previously discussed limitations on assessing focusing utility with RaXPol data and (2) the short duration of this tornado.

In order to fully understand any utility focusing updates may have on the warning decision process, it would be desirable to know forecaster preferences on the persistence of a TVS before issuing a warning. In this case, the tornado could potentially be sampled up to four times with focusing implemented: once as a full PPI, two times with 20-s sector scan updates, and once again as a full PPI scan. This is because it quickly dissipated and gave way to tornado 5. Therefore, the persistence directly associated with tornado 4 is limited, and it seems doubtful this signature would have been sampled long enough to prompt a warning by itself. Perhaps these scans would be useful in cyclic supercells like this one to potentially identify when a stronger tornado may take place amongst preceding weak tornadoes, but without a more complete understanding of forecaster perspective, this remains subjective to the author. Additionally, this tornado was ongoing with another further to the west. Thus, while these two would have been in the same sector, would a weak tornado such as this one take priority over a stronger one? If they had not been in the same sector, doubt is cast on if a weaker velocity couplet would be chosen over sampling an ongoing, stronger tornado.

For these reasons, although the focusing results promote an increased temporal resolution that better resolves tornado 4 (especially in comparison to WSR-88D updates), these images are not shown.

5.3.2 Tornado 5

The analysis of PPIs of Z (Fig. 5.13) show once again the capability to completely observe the structure of the supercell well across all PPIs. The continued development of a weak echo hole is captured and displayed well in this set of PPIs. By the final PPI provided in Figure 5.13(f), this feature has become increasingly well defined in comparison to the beginning formation $\sim$90 s earlier in Figure 5.13(a). The rapid evolution of this feature would not have been sampled by a WSR-88D system, but would more likely be sampled at any of the remaining temporal resolutions discussed in this study.

The analysis of PPIs of V_r (Fig. 5.14) shows the TVS remains identifiable. As focusing is only providing rapid sector updates, the data remain the same. Across the volume updates here, you can slowly begin to see the rotation begin to reintensify at this low elevation angle. By the time shown in Figure 5.13(f), the inbound and outbound V_r begin to contract and tighten into a better velocity couplet.

As focusing is only providing rapid sector updates, the data remain the same. With this case, a good example of how focusing could be used to capture signatures associated with an intensifying tornado (e.g., weak echo hole) is found. Paired with the intensification detectable in V_r, this set of PPIs highlights the intensification which took place at the end of the time series of ΔV shown throughout Section 5.1.2. Scenarios like this would be good candidates for times when focusing would be worthwhile in an operational setting. The difficulty, however, relies on how well forecasters can handle the amount of data available while also analyzing it for any indication that tornadogenesis and/or intensification is ongoing or likely to occur.
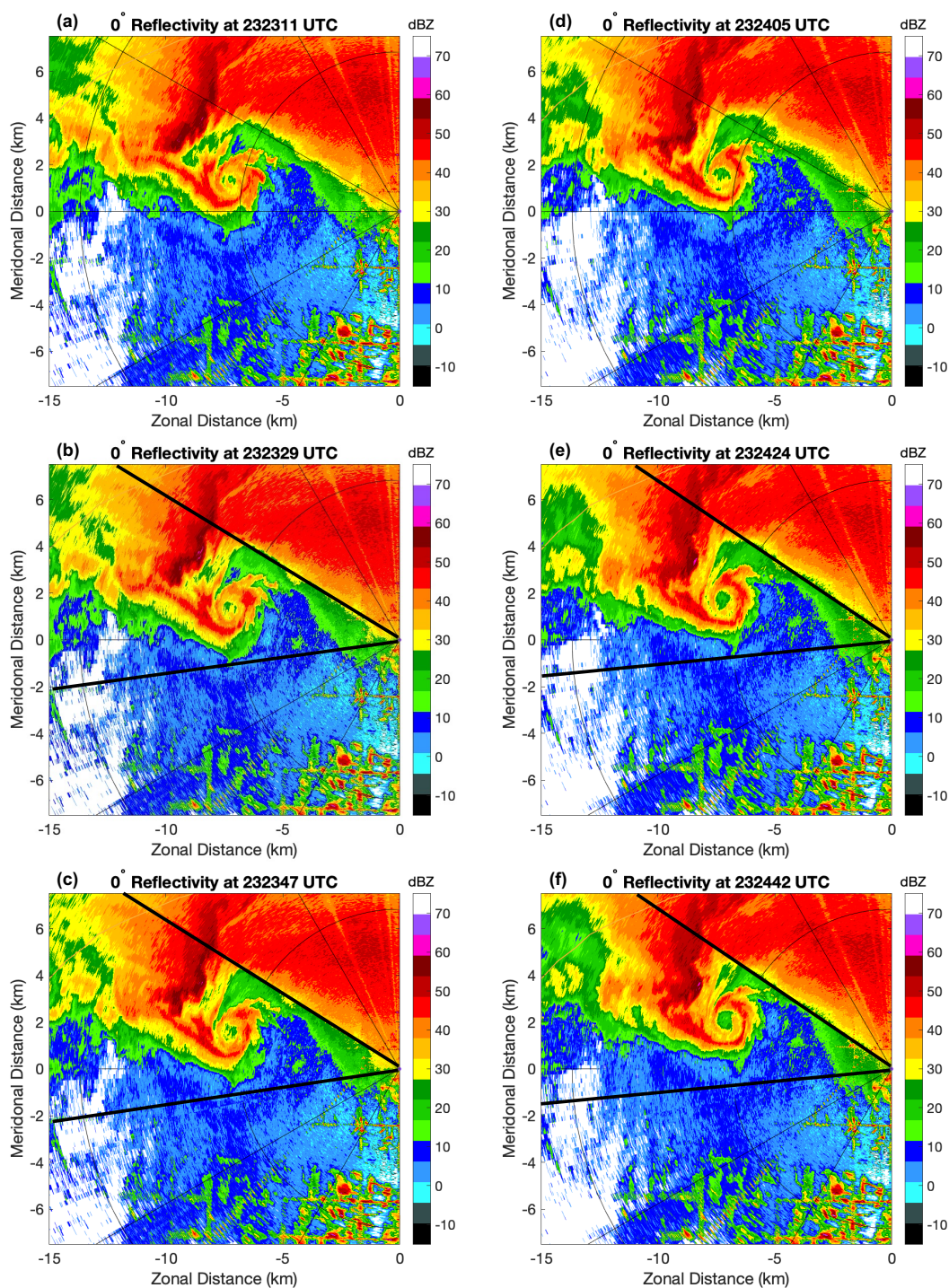
Figure 5.13: PPIs of Z at the 0° elevation angle on 24 May 2016 at (a) 2323:11 UTC, (b) 2323:29 UTC, (c) 2323:47 UTC, (d) 2323:05 UTC, (e) 2323:24 UTC, and (f) 2323:42 UTC. The figure is designed to be read by column top to bottom. Panel (a) shows a starting time with panels (b) and (c) showing the 20-s update of the 45° sector of interest outlined by black annotations. Panel (d) shows another 1-min update with panels (e) and (f) showing the same 20-s updates as (b) and (c).
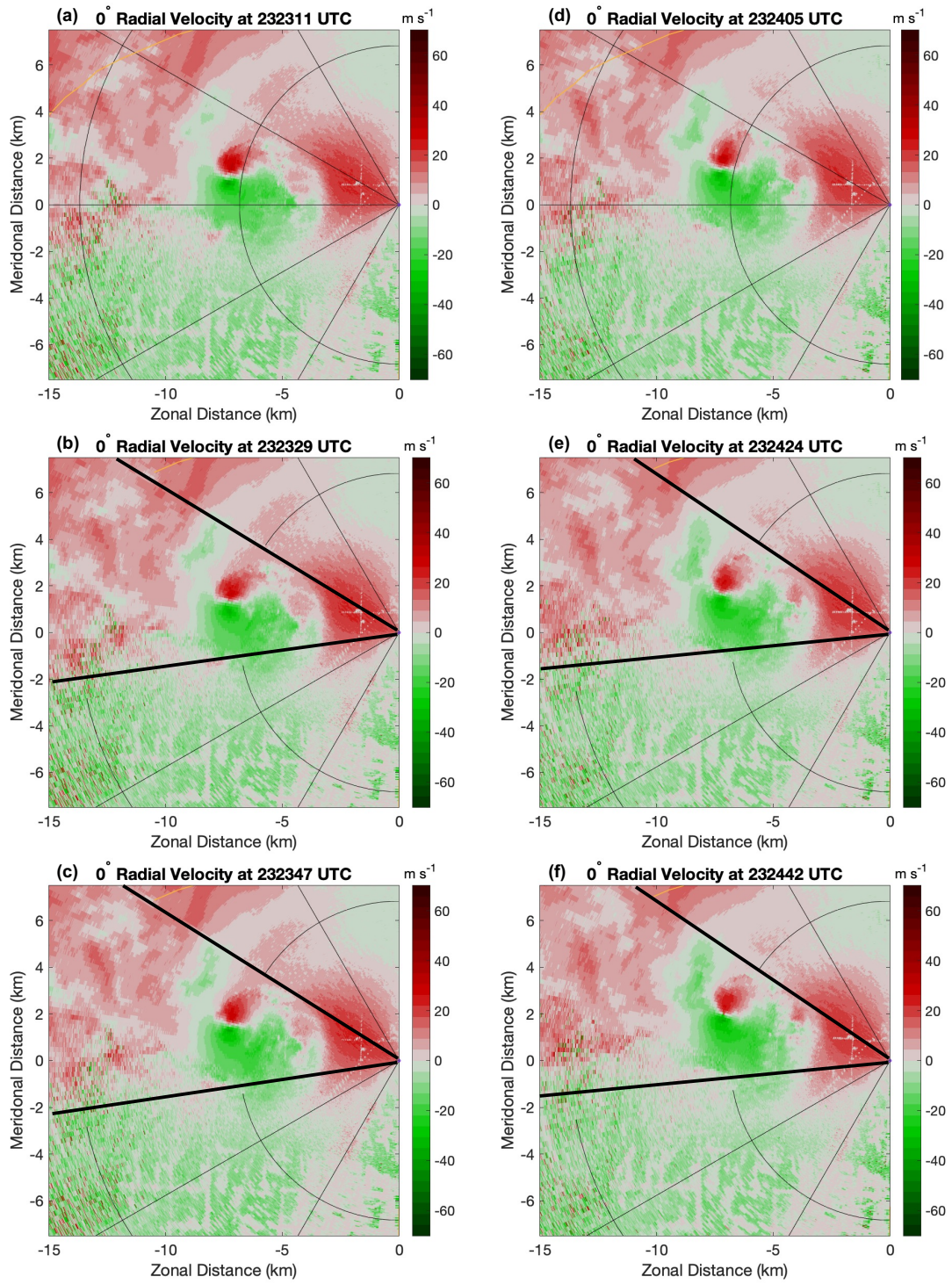
Figure 5.14: As in Figure 5.13, but here of V_r.

Chapter 6

Conclusions & Future Work

6.1   Summary of Conclusions

This study analyzed the meteorological benefits of a future operational PAR across three mesocyclone-produced tornadoes in supercells from two different cases in the central United States. Both cases were observed by RaXPol, which allowed for rapid-scan observations of the TVSs analyzed at close range of no more than 12.5 km. Spatial averaging, temporal downsampling, and simulations of a focusing PAR scanning technique were all applied to the data sets to provide the synthetic PAR data necessary for analysis. These methods generated a data set focused on analysis of the spatial and temporal effects on long range data as well as the general impacts of focusing. This analysis was used to consider some key science questions, including: (1) since tornadoes are observed at coarser resolution with long-range data, can rapid-scan signatures still provide substantial benefits? and (2) are the primary trends in tornadogenesis and intensification still seen with different PAR scanning strategies, and which are the most and least effective at this?

In the spatial analysis, despite increasingly coarse resolution, similar qualitative trends in intensity are seen even with the decreasing magnitude of ΔV as standoff ranges are increased. Though these qualitative trends are less detectable with weak tornadoes, a quantitative ΔV analysis may prove more useful in these cases. The TVS intensification is found to occur in an ascending or nearly simultaneous manner through

at least 2.5 km AGL for case I and 0.8 km AGL for case II, even for the longer emulated standoff ranges. This is consistent with previous work done which used mobile radar data for analysis. Rapid TVS intensification is also seen aloft, even if surface observations are absent. This rapid intensification signature, evident at long ranges, could help forecasters better detect tornadogenesis. Thus, it seems that a future operational PAR network may be able to detect tornadogenesis via TVS intensification mechanisms more akin to mobile radar studies versus those completed with WSR-88D data showing descending TVS intensification. Additionally, as a number of rapid-scan radar studies have found TVS intensification to occur in this manner over a few kilometers in depth, this could allow for TVS detection at longer ranges, as found in this study. A slight delay in identifying the TVS intensification, in comparison to the original data's genesis times, is found at the longer-standoff ranges. This delay was generally found to be only one volume scan, so it seems that the tornado-scale and mesocyclone-scale rotations are intensifying at roughly the same rate (i.e., intensification appears to be somewhat scale independent).

Several temporal resolutions were examined in this study. For all cases, tornadogenesis occurred in ~1 min or less. This rapidly evolving process underscores the need for faster temporal updates to better capture their structure and evolution. Several weaker tornadoes in case II were observed that exhibited entire lifecycles in ~90 s or less. With current WSR-88D update times, these tornadoes are likely to be missed or poorly observed. Results in this study show the utility of data at 60-s temporal resolution (and faster) in better observing some of the genesis and intensification processes as well as shorter-lived tornadoes. The faster temporal resolutions of 40 s and 20 s can provide additional data for analysis, but generally were not necessary to resolve the critical steps in tornadogenesis and intensification in two of three cases (longer lived tornadoes: El Reno and Dodge City tornado 5). In the Dodge City tornado 4

case, while 60-s data may capture one volume of the tornado, 20–40-s temporal resolution data would be helpful with the identification and analysis of weak tornadoes. Additionally, utilization of these faster (20–40 s) temporal resolutions could be useful with convective focused VCPs similar to WSR-88D VCPs 12/212. There are potential implications to how much data are more of a burden for a forecaster to analyze that could be brought about by these faster updates, which are discussed more in Section 6.2.

It was found, however, that at longer standoff ranges, the 40-s and 5-min temporal resolutions did sometimes show conflicting TVS intensification trends. It is hypothesized that this is partially related to the methodology of this study. As the data are essentially averaged to different spatial scales by looking at the varied standoff ranges, it appears that this analysis may identify tornado-scale rotation intensifies in a manner consistent with mobile radar studies, but the mesocyclone-scale rotation may intensify in a downward sense. Identifying what is seen at additional temporal resolutions between these two (besides only 60-s) would be helpful in determining if this is exists beyond those update times.

Despite the limitations of this data set in well identifying the potential benefits as well as practical implications for its use in operations, focusing may provide a potential middle-ground in providing faster temporal resolution data. The greatest difference from current WSR-88D capabilities focusing appears to provide is a targeted look at a mesocyclone or other area of interest. This scanning strategy could be used across multiple elevation angles in contrast to the SAILs mode used by WSR-88Ds.

6.2   Considerations for Future Operational PARs

This study not only highlights some of the benefits of a future operational PAR, but it also brings up some further considerations worthy of discussion.

While visual analysis may lead to challenges in determining the intensity and direction of TVS intensification for weak tornadoes (Section 5.1.1), providing an additional look at the actual ΔV helped to confirm intensification occurring nearly simultaneously across the depth of the column scanned. Even though the scanning strategy used limited the analysis to a discussion focused more on near-surface and the lower atmosphere, it at least confirmed the presence of low-level rotation that was still detectable at such a far range, albeit with some quick calculations required. This does raise the question of operational impact. Would a forecaster have the time in a warning decision scenario to perform this gate-to-gate calculation? Would they actually take the time to for something that appears visually unimpressive, if tools similar to this ΔV time versus height chart were available in real-time? It seems more likely, from the research perspective, that a weak tornado located this far from the radar could possibly go by undetected.

If a future operational PAR is able to detect tornadogenesis via TVS intensification mechanisms in a non-descending manner, this will require some shift in forecaster conceptual models. As they currently anticipate upper-level intensification first and a downward intensification after (as discussed, this is owed to WSR-88D update times and compounded by poor spatial resolution and near-ground data coverage at farther ranges), this may require further training when the new network is implemented beyond just processing additional data.

In the temporal resolution analysis of this study, it was shown that the amount of data presented at the higher temporal resolutions (especially 20-s) is significantly more

than currently available to operational forecasters. As a result, it becomes important to consider, similar to Wilson et al. (2017a): How much data are too much for forecasters to consider? Put another way, what would a forecaster do with so much data, and is there some point where the additional data are more of a burden than a benefit to the warning process? While some possible answers to these questions may come from Kurdzo et al. (2017), additional future work can include the opportunity to provide these data sets updated at varied temporal resolutions to forecasters at the NWS and receive their feedback on the operational impact of these results. Additional work on the exact specifications of a future operational PAR will also need to be discussed to understand what physical limitations there will be on how quickly the system can complete one revolution (for a rotating PAR), as this may further limit the temporal resolution capabilities. From trade-offs with faster revolutions introducing more beam smearing (i.e., creating a slightly larger effective beamwidth) to the general wear-and-tear on motors, these are just some of the physical limitations possible in resulting in a slower temporal resolution.

With respect to focusing, there are a few additional considerations for development of such a scanning strategy into an operational PAR network. These include: priority for various severe and non-severe hazards (e.g., do tornadoes have higher importance over hail cores?), forecaster controlled areas of focusing versus automated methods to select sector for focusing, and, for extreme cases where tornado outbreaks may be on-going, how to shift between multiple foci of the same hazard. These considerations will allow for a more well-rounded suite of scanning strategies and capabilities whenever it comes to implementation of a nationwide PAR ready to operate in unique, challenging, and rapidly-evolving weather environments alongside severe hazards. On a broader scale, all of these considerations might add additional burden to a forecaster compared

to the current process which just requires selecting a pre-defined VCP, especially without some degree of automation built into the system. Overall, it does appear that there could be benefit to implementation of a focusing scanning strategy for a future operational PAR. However, the extent of this benefit appears highly dependent upon specific observational goals and the final system's architecture.

Considering the PAR scanning techniques discussed in this study alongside others such as beam multiplexing, one further consideration remains. Is there the possibility of using a VCP (possibly longer than the 60 s operational goal) that could implement multiple PAR enabled scanning techniques in that VCP time? Would there be a list of desirable scenarios (e.g., tornado or large hail approaching a large city) that would call for the use of a specific PAR technique? How might these data be ingested into algorithms to aid forecaster decision making? Even if forecasters do not want to see PPIs every 20–40 s, the assimilation of these data into algorithms at this resolution may result in better products that give these faster scans more value.

While these questions are beyond the scope of this study, they are important considerations for continued development of the capabilities for any future operational PAR.

6.3 Future Work

The sample size of this study is small, and it does not provide a complete view of the range of intensity, duration, or environments associated with tornadic or non-tornadic supercells. Expanding the storms analyzed would aid in the further generalization of results to more tornadic and non-tornadic supercells. The addition of analysis from supercells near Medicine Park/Lawton, OK on 17 April 2013 will be used to provide a first look at non-tornadic supercells with this methodology. A unique aspect of this

case is that it is observed by both the AIR and RaXPol, enabling pencil beam versus imaging comparisons.

The synthetic PAR data tool also remains an actively updated tool. The planned implementation of 2D imaging by adding in the capability to conduct vertical and horizontal imaging to the synthetic PAR data tool will provide further insight into the utility of imaging. It would also be helpful to emulate minimum beam altitude changes associated with long-range (i.e., detection of mesocyclone altitudes rather than the tornado due to Earth's curvature effects) for the denial of low-level observations. This would allow for determining if significant benefits is still obtained when low-level observations are unavailable. Additional expansion to include polarimetric variables such as Z_{DR} and ρ_{hv} would allow this methodology to be applied to the TDS as well.

Conducting quantitative analysis with TVS algorithm threshold criteria may be helpful to further understand the significance of our results, especially at the longer emulated standoff ranges. Further, acknowledging the conclusions of Houser et al. (2022), it is likely that the results of this work are dependent on the ΔV thresholds used that deemed rotation to be tornadic or not. The application of their methodology may further discussion related to the development of a more standard set of TVS identification criterion, and could better allow for further analyzing some of the conflicting TVS intensification methods found at the 40-s and 5-min temporal resolutions.

When the all-digital Horus radar is fully completed and brought online to collect weather observations, it will serve as a demonstrator providing the unique opportunity to examine the operational benefits of PAR technology for a wide spectrum of meteorological cases. The system will be used to answer this question: "In different modes of PAR scanning operations, how do data from the all-digital Horus radar compare to data from nearby S-band polarimetric radars, and what is the operational utility of data from an all-digital PAR?" over the course of the author's PhD studies.

Alongside his current advisors and the larger senior research team, this work will use dual-polarization measurements from Horus to perform fundamental inter-comparisons of different PAR scanning techniques to evaluate their benefits and limitations for different meteorological conditions and evaluate the benefits of rapid-scan observations for operational applications.

A collaborative opportunity with the PAR and Meteorological Studies team at the Cooperative Institute for Severe and High-Impact Weather Research and Operations (CIWRO) is also in its beginning stages. Our teams will work together to further develop scanning strategies and attempt to collect early input from NWS forecasters. This input will allow for modifications of our scanning strategies and recommendations for a future operational PAR network.

Reference List

Adlerman, E. J., K. K. Droegemeier, and R. Davies-Jones, 1999: A numerical simulation of cyclic mesocyclogenesis. *Journal of the Atmospheric Sciences*, **56 (13)**, 2045–2069, https://doi.org/10.1175/1520-0469(1999)056⟨2045:ANSOCM⟩2.0.CO;2, URL https://linkinghub.elsevier.com/retrieve/pii/S0263876299718083http://journals.ametsoc.org/doi/10.1175/1520-0469(1999)056%3C2045:ANSOCM%3E2.0.CO;2.

Alexander, C. R., 2010: A mobile radar based climatology of supercell tornado structures and dynamics. Ph.D. dissertation, University of Oklahoma, Norman, OK, 229 pp.

Alexander, C. R., and J. Wurman, 2005: The 30 May 1998 Spencer, South Dakota, storm. Part I: The structural evolution and environment of the tornadoes. *Monthly Weather Review*, **133 (1)**, 72–96, https://doi.org/10.1175/MWR-2855.1.

Alexander, C. R., and J. M. Wurman, 2008: Updated mobile radar climatology of supercell tornado structures and dynamics. *24th Conference on Severe Local Storms*, American Meteorological Society, Savannah, GA, 19.4, URL https://ams.confex.com/ams/pdfpapers/141821.pdf.

Biggerstaff, M. I., and Coauthors, 2005: The shared mobile atmospheric research and teaching radar: A collaboration to enhance research and learning. *Bulletin of the American Meteorological Society*, **86 (9)**, 1263–1274, https://doi.org/10.1175/BAMS-86-9-1263.

Bluestein, H. B., M. M. French, I. Popstefanija, R. T. Bluth, and J. B. Knorr, 2010: A mobile, phased-array Doppler radar for the study of severe convective storms: The MWR-05XP. *Bulletin of the American Meteorological Society*, **91 (5)**, 579–600, https://doi.org/10.1175/2009BAMS2914.1.

Bluestein, H. B., J. G. Ladue, H. Stein, D. Speheger, and W. F. Unruh, 1993: Doppler radar wind spectra of supercell tornadoes. *Monthly Weather Review*, **121 (8)**, 2200–2222, https://doi.org/10.1175/1520-0493(1993)121⟨2200:DRWSOS⟩2.0.CO;2, arXiv:1011.1669v3.

Bluestein, H. B., A. L. Pazmany, J. C. Galloway, and R. E. McIntosh, 1995: Studies of the substructure of severe convective storms using a mobile 3-mm-wavelength Doppler radar. *Bullein - American Meteorological Society*, **76 (11)**, 2155–2170, https://doi.org/10.1175/1520-0477(1995)076⟨2155:sotsos⟩2.0.co;2.

Bluestein, H. B., K. J. Thiem, J. C. Snyder, and J. B. Houser, 2019: Tornadogenesis and early tornado evolution in the El Reno, Oklahoma, supercell on 31 May 2013. *Monthly Weather Review*, **147 (6)**, 2045–2066, https://doi.org/10.1175/MWR-D-18-0338.1.

Bluestein, H. B., and W. P. Unruh, 1989: Observations of the wind field in tornadoes, funnel clouds, and wall clouds with a portable Doppler radar. *Bulletin - American Meteorological Society*, **70 (12)**, 1514–1525, https://doi.org/10.1175/1520-0477(1989)070⟨1514:OOTWFI⟩2.0.CO;2.

Bluestein, H. B., and R. M. Wakimoto, 2003: Mobile Radar Observations of Severe Convective Storms. *Meteorological Monographs*, **30 (52)**, 105–105, https://doi.org/10.1175/0065-9401(2003)030⟨0105:mroosc⟩2.0.co;2.

Bluestein, H. B., C. C. Weiss, and A. L. Pazmany, 2003: Mobile Doppler radar observations of a tornado in a supercell near Bassett, Nebraska, on 5 June 1999. Part I: Tornadogenesis. *Monthly Weather Review*, **131 (12)**, 2954–2967, https://doi.org/10.1175/1520-0493(2003)131⟨2954:MDROOA⟩2.0.CO;2.

Bowden, K. A., and P. L. Heinselman, 2016: A qualitative analysis of NWS forecasters' use of phased-array radar data during severe hail and wind events. *Weather and Forecasting*, **31 (1)**, 43–55, https://doi.org/10.1175/WAF-D-15-0089.1.

Bowden, K. A., P. L. Heinselman, D. M. Kingfield, and R. P. Thomas, 2014: The phased array radar innovative sensing experiment 2013. *30th Conference On Environmental Information Processing Technologies*, American Meteorological Society, Ed., Atlanta, GA.

Bowden, K. A., P. L. Heinselman, D. M. Kingfield, and R. P. Thomas, 2015: Impacts of phased-array radar data on forecaster performance during severe hail and wind events. *Weather and Forecasting*, **30 (2)**, 389–404, https://doi.org/10.1175/WAF-D-14-00101.1.

Brotzge, J., K. Hondl, B. Philips, L. Lemon, E. J. Bass, D. Rude, and J. L. Andra, 2010: Evaluation of distributed collaborative adaptive sensing for detection of low-level circulations and implications for severe weather warning operations. *Weather and Forecasting*, **25 (1)**, 173–189, https://doi.org/10.1175/2009WAF2222233.1.

Brown, R. A., L. R. Lemon, and D. W. Burgess, 1978: Tornado Detection by Pulsed Doppler Radar. *Monthly Weather Review*, **106**, 29–38, https://doi.org/https://doi.org/10.1175/1520-0493(1978)106⟨0029:TDBPDR⟩2.0.CO;2.

Brown, R. A., and V. T. Wood, 2012: The tornadic vortex signature: An update. *Weather and Forecasting*, **27 (2)**, 525–530, https://doi.org/10.1175/WAF-D-11-00111.1.

Burgess, D. W., R. Donaldson Jr., and P. Desrochers, 1993: Tornado detection and warning by radar. *The Tornado: Its Structure, Dynamics, Prediction, and Hazards*, Geophysical Monograph Series, 79th ed., American Geophysical Union, 203–221.

Burgess, D. W., L. R. Lemon, and R. A. Brown, 1975: Tornado characteristics revealed by Doppler radar. *Geophysical Research Letters*, **2 (5)**, 183–184, https://doi.org/10.1029/GL002i005p00183, URL http://doi.wiley.com/10.1029/GL002i005p00183.

Burgess, D. W., M. A. Magsig, J. Wurman, D. C. Dowell, and Y. Richardson, 2002: Radar observations of the 3 May 1999 Oklahoma City tornado. *Weather and Forecasting*, **17 (3)**, 456–471, https://doi.org/10.1175/1520-0434(2002)017⟨0456:ROOTMO⟩2.0.CO;2.

Burgess, D. W., V. T. Wood, and R. A. Brown, 1992: Mesocyclone evolution statistics. Preprints, *12th Conf. on Severe Local Storms*, San Antonio, TX, American Meteorological Society, 422–424.

Cho, J. Y. N., J. M. Kurdzo, B. J. Bennett, M. E. Weber, J. W. Dellicarpini, A. Loconto, and H. Frank, 2022: Impact of WSR-88D intra-volume low-level scans on severe weather warning performance. *Weather and Forecasting*, 1–50, https://doi.org/10.1175/WAF-D-21-0152.1, URL https://journals.ametsoc.org/view/journals/wefo/aop/WAF-D-21-0152.1/WAF-D-21-0152.1.xml.

Cook, R. D., T. L. Allmon, G. Secrest., A. D. Free, D. L. Rose, and J. M. Williams, 2014: A service life extension program for the WSR-88D radars. *30th Conference on Environmental Information Processing Technologies*, American Meteorological Society, Atlanta, GA.

Crum, T. D., and R. L. Alberty, 1993b: The WSR-88D and the WSR-88D operational support facility. *Bulletin of the American Meteorological Society*, **74 (9)**, 1669–1687, https://doi.org/10.1175/1520-0477(1993)074⟨1669:TWATWO⟩2.0.CO;2.

Curtis, C. D., and S. M. Torres, 2011: Adaptive range oversampling to achieve faster scanning on the National Weather Radar Testbed phased-array radar. *Journal of Atmospheric and Oceanic Technology*, **28 (12)**, 1581–1597, https://doi.org/10.1175/JTECH-D-10-05042.1.

Doviak, R. J., and D. S. Zrnić, 2006: *Doppler Radar and Weather Observations.* 2nd ed., Dover Publications, 562 pp.

Dowell, D. C., and H. B. Bluestein, 2002: The 8 June 1995 McLean, Texas, storm. Part I: Observations of cyclic tornadogenesis. *Monthly Weather Review*, **130 (11)**, 2626–2648, https://doi.org/10.1175/1520-0493(2002)130⟨2626:TJMTSP⟩2.0.CO;2.

Dunn, L. B., 1990: Two examples of operational tornado warnings using Doppler radar data. *Bulletin of the American Meteorological Society*, **71 (2)**, 145–153, https://doi.org/10.1175/1520-0477(1990)071⟨0145:TEOOTW⟩2.0.CO;2.

Dunn, L. B., and S. V. Vasiloff, 2001: Tornadogenesis and operational considerations of the 11 August 1999 Salt Lake City Tornado as seen from two different Doppler radars.

Weather and Forecasting, **16 (4)**, 377–398, https://doi.org/10.1175/1520-0434(2001) 016⟨0377:TAOCOT⟩2.0.CO;2.

Emersic, C., P. L. Heinselman, D. R. MacGorman, and E. C. Bruning, 2011: Lightning activity in a hail-producing storm observed with phased-array radar. *Monthly Weather Review*, **139 (6)**, 1809–1825, https://doi.org/10.1175/2010MWR3574.1.

French, M. M., H. B. Bluestein, I. Popstefanija, C. A. Baldi, and R. T. Bluth, 2013: Reexamining the vertical development of tornadic vortex signatures in supercells. *Monthly Weather Review*, **141 (12)**, 4576–4601, https://doi.org/10.1175/ MWR-D-12-00315.1.

French, M. M., H. B. Bluestein, I. Popstefanija, C. A. Baldi, and R. T. Bluth, 2014: Mobile, phased-array, Doppler radar observations of tornadoes at X band. *Monthly Weather Review*, **142 (3)**, 1010–1036, https://doi.org/10.1175/MWR-D-13-00101.1.

Fulton, C., M. Yeary, D. Thompson, J. Lake, and A. Mitchell, 2016: Digital Phased Arrays: Challenges and Opportunities. *Proceedings of the IEEE*, **104 (3)**, 487–503, https://doi.org/10.1109/JPROC.2015.2501804.

Griffin, C. B., D. J. Bodine, J. M. Kurdzo, A. Mahre, and R. D. Palmer, 2019: High-temporal resolution observations of the 27 May 2015 Canadian, Texas, Tornado using the atmospheric imaging radar. *Monthly Weather Review*, **147 (3)**, 873–891, https://doi.org/10.1175/MWR-D-18-0297.1.

Heinselman, P., D. Ladue, D. M. Kingfield, and R. Hoffman, 2015: Tornado warning decisions using phased-array radar data. *Weather and Forecasting*, **30 (1)**, 57–78, https://doi.org/10.1175/WAF-D-14-00042.1.

Heinselman, P. L., D. S. Ladue, and H. Lazrus, 2012: Exploring impacts of rapid-scan radar data on NWS warning decisions. *Weather and Forecasting*, **27 (4)**, 1031–1044, https://doi.org/10.1175/WAF-D-11-00145.1.

Heinselman, P. L., D. L. Priegnitz, K. L. Manross, T. M. Smith, and R. W. Adams, 2008: Rapid sampling of severe storms by the National Weather Radar Testbed Phased Array Radar. *Weather and Forecasting*, **23 (5)**, 808–824, https://doi.org/ 10.1175/2008WAF2007071.1.

Heinselman, P. L., and S. M. Torres, 2011: High-temporal-resolution capabilities of the National Weather Radar Testbed Phased-Array Radar. *Journal of Applied Meteorology and Climatology*, **50 (3)**, 579–593, https://doi.org/10.1175/2010JAMC2588.1.

Hondl, K., and M. Weber, 2019: NOAA's Meteorological Phased Array Radar Research Program. *IEEE International Symposium on Phased Array Systems and Technology*, **2019-October**, https://doi.org/10.1109/PAST43306.2019.9020994.

Houser, J. L., H. B. Bluestein, and J. C. Snyder, 2015: Rapid-scan, polarimetric, Doppler radar observations of tornadogenesis and tornado dissipation in a tornadic supercell: The "El Reno, Oklahoma" storm of 24 May 2011. *Monthly Weather Review*, **143 (7)**, 2685–2710, https://doi.org/10.1175/MWR-D-14-00253.1.

Houser, J. L., H. B. Bluestein, and J. C. Snyder, 2016: A finescale radar examination of the tornadic debris signature and weak-echo reflectivity band associated with a large, violent Tornado. *Monthly Weather Review*, **144 (11)**, 4101–4130, https://doi.org/10.1175/MWR-D-15-0408.1.

Houser, J. L., H. B. Bluestein, K. Thiem, J. Snyder, D. Reif, and Z. Wienhoff, 2022: Additional Evaluation of the Spatiotemporal Evolution of Rotation during Tornadogenesis Using Rapid-Scan Mobile Radar Observations. *Monthly Weather Review*, **150 (7)**, 1639–1666, https://doi.org/10.1175/MWR-D-21-0227.1.

Isom, B., and Coauthors, 2013: The atmospheric imaging radar: Simultaneous volumetric observations using a phased array weather radar. *Journal of Atmospheric and Oceanic Technology*, **30 (4)**, 655–675, https://doi.org/10.1175/jtech-d-12-00063.1.

Ivic, I., C. Curtis, E. Forren, R. Mendoza, D. Schvartzman, S. Torres, D. J. Wasielewski, and F. A. Zahrai, 2019: An Overview of Weather Calibration for the Advanced Technology Demonstrator. *IEEE International Symposium on Phased Array Systems and Technology*, https://doi.org/10.1109/PAST43306.2019.9021053.

Joint Action Group for Phased Array Radar Project, 2006: Federal Research and Development Needs and Priorities for Phased Array Radar, FCM-R25-2006. Tech. rep., 119 pp.

Kingfield, D. M., and M. M. French, 2022: The influence of WSR-88D intra-volume scanning strategies on thunderstorm observations and warnings in the Dual-Polarization radar era: 2011–20. *Weather and Forecasting*, **37 (2)**, 283–301, https://doi.org/10.1175/WAF-D-21-0127.1, URL https://journals.ametsoc.org/view/journals/wefo/37/2/WAF-D-21-0127.1.xml.

Kollias, P., E. P. Luke, K. Tuftedal, M. Dubois, and E. J. Knapp, 2022: Agile Weather Observations using a Dual-Polarization X-band Phased Array Radar. *2022 IEEE Radar Conference*, IEEE, 1–6, https://doi.org/10.1109/RadarConf2248738.2022.9764308.

Kurdzo, J. M., D. J. Bodine, B. L. Cheong, and R. D. Palmer, 2015: High-temporal resolution polarimetric X-band Doppler radar observations of the 20 May 2013 Moore, Oklahoma, Tornado. *Monthly Weather Review*, **143 (7)**, 2711–2735, https://doi.org/10.1175/MWR-D-14-00357.1.

Kurdzo, J. M., B. L. Cheong, R. D. Palmer, G. Zhang, and J. B. Meier, 2014: A pulse compression waveform for improved-sensitivity weather radar observations. *Journal*

of Atmospheric and Oceanic Technology, **31 (12)**, 2713–2731, https://doi.org/10.1175/JTECH-D-13-00021.1.

Kurdzo, J. M., and Coauthors, 2017: Observations of severe local storms and tornadoes with the atmospheric imaging radar. *Bulletin of the American Meteorological Society*, **98 (5)**, 915–935, https://doi.org/10.1175/BAMS-D-15-00266.1.

Kuster, C. M., P. L. Heinselman, and M. Austin, 2015: 31 May 2013 El Reno Tornadoes: Advantages of rapid-scan phased-array radar data from a warning forecaster's perspective. *Weather and Forecasting*, **30 (4)**, 933–956, https://doi.org/10.1175/WAF-D-14-00142.1.

Kuster, C. M., P. L. Heinselman, and T. J. Schuur, 2016: Rapid-update radar observations of downbursts occurring within an intense multicell thunderstorm on 14 June 2011. *Weather and Forecasting*, **31 (3)**, 827–851, https://doi.org/10.1175/WAF-D-15-0081.1.

Leslie, L. M., 1971: The development of concentrated vortices: A numerical study. *Journal of Fluid Mechanics*, **48 (1)**, 1–21, https://doi.org/https://doi.org/10.1017/S0022112071001435.

Lhermitte, R. M., and E. Kessler, 1964: An experimental pulse Doppler radar for severe storm investigations. *Proc. 1964 World Conf. on Radio Meteorology and 11th Weather Radar Conf.*, American Meteorological Society, 304–309.

McLaughlin, D., and Coauthors, 2009: Short-wavelength technology and the potential for distributed networks of small radar systems. *Bulletin of the American Meteorological Society*, **90 (12)**, 1797–1818, https://doi.org/10.1175/2009BAMS2507.1, URL https://journals.ametsoc.org/doi/10.1175/2009BAMS2507.1.

Mead, J., A. Pazmany, S. Sekelsky, and R. McIntosh, 1994: Millimeter-wave radars for remotely sensing clouds and precipitation. *Proceedings of the IEEE*, **82 (12)**, 1891–1906, https://doi.org/10.1109/5.338077.

National Research Council, 2002: *Weather Radar Technology Beyond NEXRAD*. The National Academies Press, Washington, DC, 1–98 pp., https://doi.org/10.17226/10394.

National Research Council, 2008: *Evaluation of the Multifunction Phased Array Radar Planning Process*. The National Academies Press, Washington, DC, 1–79 pp., https://doi.org/10.17226/12438.

National Severe Storms Laboratory, 2020: Spectrum Efficient National Surveillance Radar (SENSR): OAR Feasibility Study Final Report. 1–142.

National Weather Service, 2015: NOAA/National Weather Service Radar Functional Requirements. Tech. rep., National Oceanic and Atmospheric Administration, 57 pp. URL https://www.roc.noaa.gov/WSR88D/PublicDocs/NOAA_Radar_Functional_Requirements_Final_Sept2015.pdf.

Newman, J. F., and P. L. Heinselman, 2012: Evolution of a quasi-linear convective system sampled by phased array radar. *Monthly Weather Review*, **140 (11)**, 3467–3486, https://doi.org/10.1175/MWR-D-12-00003.1.

Office of the Federal Coordinator for Meteorological Services and Supporting Research, 2007: WSR-88D unit description and operational applications. Doppler Radar Meteorological Observations. Federal Meteorological Handbook 11, Part D, FCM-H11D-2006. 218 pp., URL https://www.icams-portal.gov/resources/ofcm/fmh/FMH11/FMH11D-2006.pdf.

Palmer, R. D., C. J. Fulton, J. Salazar, H. Sigmarsson, and M. Yeary, 2019: The "Horus" radar: An all-digital polarimetric phased array radar for multi-mission surveillanceitle. *35th Conference on Environmental Information Processing Technologies*, American Meteorological Society, Phoenix, AZ, URL https://ams.confex.com/ams/2019Annual/webprogram/Paper349962.html.

Pazmany, A. L., J. B. Mead, H. B. Bluestein, J. C. Snyder, and J. B. Houser, 2013: A mobile rapid-scanning X-band polarimetric (RaXPol) Doppler radar system. *Journal of Atmospheric and Oceanic Technology*, **30 (7)**, 1398–1413, https://doi.org/10.1175/JTECH-D-12-00166.1.

Radar Operations Center, 2015: WSR-88D Volume Coverage Pattern (VCP) Improvement Initiatives. URL https://www.roc.noaa.gov/WSR88D/PublicDocs/NewTechnology/New_VCP_Paradigm_Public_Oct_2015.pdf.

Rotunno, R., 1986: Tornadoes and tornadogenesis. *Mesoscale Meteorology and Forecasting*, P. Ray, Ed., American Meteorological Society, 414–436.

Rotunno, R., 1993: Supercell thunderstorm modeling and theory. *The Tornado: Its Structure, Dynamics, Prediction, and Hazards*, Geophysical Monograph Series, 79th ed., American Geophysical Union, 57–74.

Ryzhkov, A. V., M. R. Kumjian, S. M. Ganson, and P. Zhang, 2013: Polarimetric radar characteristics of melting hail part II: Practical implications. *Journal of Applied Meteorology and Climatology*, **52 (12)**, 2871–2886, https://doi.org/10.1175/JAMC-D-13-074.1.

Salazar, J. L., and Coauthors, 2019: An Ultra-Fast Scan C-band Polarimetric Atmospheric Imaging Radar (PAIR). *IEEE International Symposium on Phased Array Systems and Technology*, **2019-October**, 1–5, https://doi.org/10.1109/PAST43306.2019.9021042.

Smith, R. L., and D. W. Holmes, 1961: Use of Doppler radar in meteorological observations. *Monthly Weather Review*, **89 (1)**, 1–7, https://doi.org/10.1175/1520-0493(1961)089⟨0001:UODRIM⟩2.0.CO;2, URL http://journals.ametsoc.org/doi/10.1175/1520-0493(1961)089%3C0001:UODRIM%3E2.0.CO;2.

Snyder, J. C., and H. B. Bluestein, 2014: Some considerations for the use of high-resolution mobile radar data in tornado intensity determination. *Weather and Forecasting*, **29 (4)**, 799–827, https://doi.org/10.1175/WAF-D-14-00026.1.

Tanamachi, R. L., H. B. Bluestein, W. C. Lee, M. Bell, and A. Pazmany, 2007: Ground-based velocity track display (GBVTD) analysis of W-band Doppler radar data in a tornado near Stockton, Kansas, on 15 May 1999. *Monthly Weather Review*, **135 (3)**, 783–800, https://doi.org/10.1175/MWR3325.1.

Tanamachi, R. L., and P. L. Heinselman, 2016: Rapid-scan, polarimetric observations of central Oklahoma severe storms on 31 May 2013. *Weather and Forecasting*, **31 (1)**, 19–42, https://doi.org/10.1175/WAF-D-15-0111.1.

Torres, S. M., and D. Schvartzman, 2020: A simulation framework to support the design and evaluation of adaptive scanning for phased-array weather radars. *Journal of Atmospheric and Oceanic Technology*, **37 (12)**, 2321–2339, https://doi.org/10.1175/JTECH-D-20-0087.1.

Trapp, R. J., and R. Davies-Jones, 1997: Tornadogenesis with and without a dynamic pipe effect. *Journal of the Atmospheric Sciences*, **54 (1)**, 113–133, https://doi.org/10.1175/1520-0469(1997)054⟨0113:TWAWAD⟩2.0.CO;2.

Trapp, R. J., and B. H. Fiedler, 1995: Tornado-like Vortexgenesis in a Simplified Numerical Model. *Journal of the Atmospheric Sciences*, **52 (21)**, 3757–3778, https://doi.org/10.1175/1520-0469(1995)052⟨3757:TLVIAS⟩2.0.CO;2, URL http://journals.ametsoc.org/doi/10.1175/1520-0469(1995)052%3C3757:TLVIAS%3E2.0.CO;2.

Trapp, R. J., and E. D. Mitchell, 1995: Characteristics of tornadic vortex signatures detected by wsr-88d radars. 211–212, proceedings of the 1995 27th Conference on Radar Meteorology ; Conference date: 09-10-1995 Through 13-10-1995.

Trapp, R. J., E. D. Mitchell, G. A. Tipton, D. W. Effertz, A. I. Watson, D. L. Andra, and M. A. Magsig, 1999: Descending and nondescending tornadic vortex signatures detected by WSR-88Ds. *Weather and Forecasting*, **14 (5)**, 625–639, https://doi.org/10.1175/1520-0434(1999)014⟨0625:DANTVS⟩2.0.CO;2.

Vasiloff, S., 1993: Single-Doppler radar study of a variety of tornado types. *The Tornado: Its Structure, Dynamics, Prediction, and Hazards*, Geophysical Monograph Series, 79th ed., American Geophysical Union, 203–221.

Warning Decision Training Division, 2022: Base and derived products - tornado vortex signature (TVS). URL https://training.weather.gov/wdtd/courses/rac/products/tvs/presentation_html5.html.

Weber, M., and Coauthors, 2021: Towards the next generation operational meteorological radar. *Bulletin of the American Meteorological Society*, **102 (7)**, E1357–E1382, https://doi.org/10.1175/BAMS-D-20-0067.1.

Wienhoff, Z. B., H. B. Bluestein, D. W. Reif, R. M. Wakimoto, L. J. Wicker, and J. M. Kurdzo, 2020: Analysis of debris signature characteristics and evolution in the 24 May 2016 Dodge City, Kansas, Tornadoes. *Monthly Weather Review*, **148 (12)**, 5063–5086, https://doi.org/10.1175/MWR-D-20-0162.1.

Wilson, J., R. Carbone, H. Baynton, and R. Serafin, 1980: Operational application of meteorological Doppler radar. *Bulletin of the American Meteorological Society*, **61 (10 , Oct. 1980)**, 1154–1168, https://doi.org/10.1175/1520-0477(1980)061⟨1154:oaomdr⟩2.0.co;2.

Wilson, K. A., P. L. Heinselman, and Z. Kang, 2016: Exploring applications of eye tracking in operational meteorology research. *Bulletin of the American Meteorological Society*, **97 (11)**, 2019–2025, https://doi.org/10.1175/BAMS-D-15-00148.1.

Wilson, K. A., P. L. Heinselman, and Z. Kang, 2018: Comparing forecaster eye movements during the warning decision process. *Weather and Forecasting*, **33 (2)**, 501–521, https://doi.org/10.1175/WAF-D-17-0119.1.

Wilson, K. A., P. L. Heinselman, and C. M. Kuster, 2017b: Considerations for phased-array radar data use within the National weather service. *Weather and Forecasting*, **32 (5)**, 1959–1965, https://doi.org/10.1175/WAF-D-17-0084.1.

Wilson, K. A., P. L. Heinselman, C. M. Kuster, D. M. Kingfield, and Z. Kang, 2017a: Forecaster performance and workload: Does radar update time matter? *Weather and Forecasting*, **32 (1)**, 253–274, https://doi.org/10.1175/WAF-D-16-0157.1.

Wurman, J., and S. Gill, 2000: Finescale radar observations of the Dimmitt, Texas (2 June 1995), Tornado. *Monthly Weather Review*, **128 (7)**, 2135–2164, https://doi.org/10.1175/1520-0493(2000)128⟨2135:FROOTD⟩2.0.CO;2.

Wurman, J., J. Straka, E. Rasmussen, M. Randall, and A. Zahrai, 1997: Design and deployment of a portable, pencil-beam, pulsed, 3-cm Doppler radar. *Journal of Atmospheric and Oceanic Technology*, **14 (6)**, 1502–1512, https://doi.org/10.1175/1520-0426(1997)014⟨1502:DADOAP⟩2.0.CO;2.

Yu, T. Y., M. B. Orescanin, C. D. Curtis, D. S. Zrnić, and D. E. Forsyth, 2007: Beam multiplexing using the phased-array weather radar. *Journal of Atmospheric and Oceanic Technology*, **24 (4)**, 616–626, https://doi.org/10.1175/JTECH2052.1.

Zhang, G., R. Doviak, D. Zrnić, and J. Crain, 2008: Phased array radar polarimetry for weather sensing: Challenges and opportunities. *International Geoscience and Remote Sensing Symposium (IGARSS)*, **5 (1)**, 449–452, https://doi.org/10.1109/IGARSS.2008.4780125.

Zrnić, D. S., and Coauthors, 2007: Agile-beam phased array radar for weather observations. *Bulletin of the American Meteorological Society*, **88 (11)**, 1753–1766, https://doi.org/10.1175/BAMS-88-11-1753.